1-1-2013

Improving SN Ia Distance Measurements Through Better Understanding of SN Ia Systematic Uncertainties

Jennifer Lynn Mosher
University of Pennsylvania, jmosher@sas.upenn.edu

Improving SN Ia Distance Measurements Through Better Understanding of SN Ia Systematic Uncertainties

Abstract
Distance measurements using Type Ia Supernovae have enabled the startling discovery that the expansion of the universe is accelerating. To determine the nature and the source of this acceleration, systematic uncertainties on distance measurement must be reduced. Due to their importance to high-redshift optical SN Ia cosmology and their sensitivity to dust and progenitor metallicity effects, understanding rest-frame near-UV (NUV) measurements of Type Ia SNe is key to reducing these systematic uncertainties. Unfortunately, the calibration and acquisition of this data is challenging.

We use direct comparisons of low-redshift SDSS-II and Carnegie Supernova Project NUV SN Ia photometry to quantify uncertainties on our ability to calibrate observer frame observations, and find that photometry in this region is consistent at the level of 2% in flux with a 6% scatter about the mean. Monte Carlo simulated SN Ia samples are used to directly measure Hubble Diagram biases resulting from SN Ia model training. Four simulated SN Ia samples are used to train the SALT-II SN Ia model: two width-luminosity adjustments and two intrinsic scatter models are tested. Adding intrinsic scatter to the training sample yields biased color laws and wavelength-dependent scatter in the NUV region, and causes the color correction parameter β to be systematically underestimated. Assuming a flat ΛCDM cosmology and including BAO and CMB constraints, three of our tests correctly recover the Dark Energy equation of state parameter w. The fourth test gives a w offset of 0.02, with a 4-σ significance. The software developed to support this work may be adapted to measure Hubble Diagram biases for any combination of SN Ia model and surveys.

Degree Type
Dissertation

Degree Name
Doctor of Philosophy (PhD)

Graduate Group
Physics & Astronomy

First Advisor
Masao Sako

Keywords
Calibration, Cosmology, Distance Measurement, Simulations, Type Ia Supernovae

Subject Categories
Astrophysics and Astronomy | Physics

IMPROVING SN Ia DISTANCE MEASUREMENTS THROUGH BETTER UNDERSTANDING OF SN Ia SYSTEMATIC UNCERTAINTIES

Jennifer Lynn Mosher

A DISSERTATION

in

Physics and Astronomy

Presented to the Faculties of the University of Pennsylvania

in Partial Fulfillment of the Requirements for the Degree of Doctor of Philosophy

2013

Supervisor of Dissertation

_____

Masao Sako, Associate Professor of Physics and Astronomy

Graduate Group Chairperson

_____

A. T. Charlie Johnson, Professor of Physics and Astronomy

Dissertation Committee

Gary Bernstein, Professor of Physics and Astronomy

Mark Devlin, Professor of Physics and Astronomy

Ravi Sheth, Professor of Physics and Astronomy

Joe Kroll, Professor of Physics and Astronomy

Dedication

For the family, friends and neighbors who have supported me and mine through the past seven years with kind words, meals, kid-schlepping, babysitting, yardwork, and Friday evening drinks around the Woodcrest Ave picnic table. I am so lucky to have you. I couldn't have done this without you.

For my husband Michael and son James, who have believed in me and given me strength when confidence has been hard to come by.

Acknowledgments

I would like to thank my advisor, Masao Sako, for his patience, support, and guidance over these past years.

I thank the members of the Sloan Digital Sky Survey-II Supernova Survey and the Joint Lightcurve Analysis group for providing essential feedback on my research, editing of my papers, and data products used throughout this thesis. The names of those who have helped are many, but I would like to thank in particular John Marriner, Richard Kessler, and Julien Guy.

I have been very fortunate to have my fellow group members Chris D'Andrea, Ravi Gupta, John Fischer, and Rachel Cane with whom to discuss all sorts of supernova related topics, computer issues, and statistical techniques over the final years of my thesis.

I thank the graduate students and post-docs I've interacted with over the course of my physics career - Michelle Calder, Jessamyn Fairfield, Tsz Yan Lam, Marisa March, Heather Campbell, Ben Dilday, Anjana Shah, Rebecca Surman, Peter Bertone, Carrie Rowland, Vera Hansper, and Diane Markoff. Your friendship, leadership, advice, and support have been invaluable to my growth as a scientist.

I'd also like to thank the UNC-Chapel Hill, Emma Willard College, Longwood University, and University of Pennsylvania students I've taught. I've learned as much from you as you've learned from me.

I thank UNC faculty Christian Iliadis and Hugon Karwowski, Bryn Mawr faculty Peter Beckmann and Neil Abraham, Union College faculty Jonathan Marr and Rebecca

Koopman, and the NIST Neutron Physics Group for guiding my interests in physics and research.

Finally, I thank my committee members, Gary Bernstein, Mark Devlin, Ravi Sheth, and Joe Kroll for reading my dissertation and providing feedback.

ABSTRACT

IMPROVING COSMOLOGICAL DISTANCE MEASUREMENTS THROUGH BETTER UNDERSTANDING OF SN Ia SYSTEMATIC UNCERTAINTIES

Jennifer Lynn Mosher

Masao Sako

Distance measurements using Type Ia Supernovae have enabled the startling discovery that the expansion of the universe is accelerating. To determine the nature and the source of this acceleration, systematic uncertainties on distance measurement must be understood. Due to their importance to high-redshift optical SN Ia cosmology and their sensitivity to dust and progenitor metallicity effects, rest-frame near-UV (NUV) measurements of Type Ia SNe are key to constraining systematic uncertainties. Unfortunately, the calibration and acquisition of this data is challenging. We use direct comparisons of low-redshift SDSS-II and Carnegie Supernova Project NUV SN Ia photometry to quantify uncertainties on our ability to calibrate observer frame observations, and find that photometry in this region is consistent at the level of 2% in flux with a 6% scatter about the mean. Monte Carlo simulated SN Ia samples are used to directly measure Hubble Diagram biases resulting from SN Ia model training. Four simulated SN Ia samples are used to train the SALT-II SN Ia model: two width-luminosity adjustments and two intrinsic scatter models are tested. Adding intrinsic scatter to the training sample yields biased color laws and wavelength-dependent scatters in the NUV region, and causes the color correction parameter β to be systematically underestimated. Assuming a flat ΛCDM cosmology and including BAO and CMB constraints, three of our tests correctly recover the Dark Energy equation of state parameter w. The fourth test gives a w offset of 0.02, with a 4-σ significance. The software developed to support this work may be adapted to measure Hubble Diagram biases for any combination of SN Ia model and surveys.

Contents

List of Tables

List of Figures

Chapter 1

Introduction

Where did Earth come from? How long have we been here? How did the Universe begin? How will it end? Cosmology is as old as humanity; we have always sought to understand the universe and our place in it. It is only how we go about answering these questions that has changed. Beginning with the invention of the telescope, advances in technology have allowed cosmology to be informed by quantitative measurements. One such measurement – distance – has played a key role during the 20th century, and continues to provide an important constraint on cosmological models.

My thesis work has focused on improving our ability to use a particular class of astronomical object, Type Ia Supernovae, as a distance measurement tool. I will begin my thesis with an overview of the importance of distance measurements to cosmology, how Type Ia Supernovae are used to measure distance, and how we would like to use these objects to improve our understanding of key cosmological parameters in the immediate future. Next I will present the key challenges inherent to the use of these objects, summarize the work others have done to constrain and overcome these challenges, and motivate the questions I was interested in answering during my time at the University of Pennsylvania. Finally, I will present the work I have done and discuss its impact with respect to future cosmology projects.

1.1 Distance Measurements and Quantitative Cosmology

Distance measurement has played a key role in humans' attempts to understand the universe. Knowing the dimensions of our physical surroundings allows us to properly situate ourselves in the context of our universe. From a cosmological point of view, the first important distance measurements were for objects in our Solar System, starting with the size of the Earth and the distances from Earth to the Sun and the Moon.

1.1.1 Early Distance Measurements

Eratosthenes of Cyrene performed the first recorded measurement of the circumference of the Earth by comparing shadows thrown at noon on the summer solstice in two cities lying at the same longitude: Alexandria and Syene. Around the same time, Aristarchus of Samos used relative sizes of shadows to estimate the relative sizes of the Earth, Moon, and Sun and the relative distances to the Sun and the Moon. After concluding that the Sun was very far away and much larger than the Earth, Aristarchus proposed that the Earth must orbit the Sun.

Understanding the concept of parallax – that the apparent position of a distant object depends on the location from which it is observed – the Greeks realized that if the Earth did orbit the Sun, then the relative positions of the stars should change over the course of the year. However, no such parallax was observed, implying one of two possibilities: either the Earth does not orbit the Sun, or the stars are so far away from the Earth as to make the parallax invisible to the naked eye. Unable to comprehend distances so immense, the Greeks instead chose to believe that the Earth was stationary, pausing the development of Western cosmology for 1500 years.

During the 1600's the invention of the telescope and the micrometer enabled more precise parallax measurements. further advances in distance measurement. These technologies were used in 1672 by Paris Observatory director Jean-Dominique Cassini and his colleague Jean Richer to measure the distance to Mars, allowing the first determination of

the absolute scale of the solar system. In 1838, Friedrich Bessel used a Fraunhofer-built micrometer to measure the parallax of the star 61 Cygni. His result – 62 mas, or a distance of 16 parsecs – astounded his contemporaries with its immensity. From the Earth's surface, parallax enables the measurement of distances out to ~ 100 parsecs[1] and forms the base of the modern distance ladder. More details on these early distance measurements may be found in the books Webb (1999) and Van Helden (2010).

Cosmological distance measurements had to wait for the refinement of two more new technologies: photographic plates and spectroscopy. Silver bromide dry emulsion plates enabled the first large-scale sky surveys, such as the Henry Draper Memorial survey run by Edward Pickering at Harvard College Observatory (Pickering 1890). The acquisition of spectra as part of these surveys allowed the classification of many different types of objects by their spectral features. Once objects could be reliably classified, their apparent brightnesses could be used as a proxy for their distances. By combining many such observations statistical estimates of stellar cluster distances could be calculated.

Imaging surveys allowed astronomers to make detailed quantitative studies of the brightnesses of variable stars: stars whose luminosities vary with time. In 1908, Henrietta Swan Leavitt published the first paper describing Cepheid Variable stars (Leavitt 1908). She found that the brightnesses of these stars correlated with the periods of their luminosity fluctuations. By using a collection of variable stars within the Small Magellanic Cloud, presumably all the same distance away from Earth, Leavitt was able to use relative brightnesses to determine the brightness-period relationship. At least one Cepheid – Delta Cephei– is close enough to Earth for its distance to be measured via parallax, allowing the absolute brightness of a Cepheid to be determined. This new understanding of Cepheid Variable stars allowed the first quantitative tests of modern scientific cosmology.

[1]Space-based measurements have higher precision. The Hipparchos satellite could measure parallax to 1 mas, and therefore distances of ~ 1000 parsecs; the soon-to-be-launched Gaia mission will measure parallax to 1 μas for distances of $\sim 1,000,000$ parsecs (e.g. Turon et al. 2012).

1.1.2 Quantitative Astronomy

Implicit in the previous section is the idea that knowing the relative brightness of two identical objects allows the distance between the objects to be measured. In this section, the physical quantities measured by astronomers will be defined.

We assume that an object such as a star emits a certain amount of energy per second. This quantity is called luminosity L, and may be time-dependent (as with variable stars). The object's energy is emitted in the form of photons, with the energy of a single photon given by Planck's equation $E = \frac{hc}{\lambda}$. Here λ is the wavelength of the photon and h is Planck's constant. Since the energy is emitted at specific wavelengths, we can further specify the specific luminosity L_λ, which is defined as the energy emitted per unit time per unit wavelength. The quantity astronomers actually measure is the specific flux f_λ of an object, defined as the energy incident per unit second per unit wavelength per unit area. Assuming that the object's energy emission is isotropic, that the energy is not being absorbed during transit, and that time and wavelength units are constant, specific luminosity L_λ and specific flux f_λ can be related by an inverse square law:

$$f_\lambda = \frac{L_\lambda}{4\pi r^2}, \tag{1.1}$$

where r is the distance between the object and the detector.

For historical reasons, optical astronomers typically report measured brightnesses in terms of magnitude rather than flux. In the magnitude system, brightnesses are logarithmic in flux and are always defined with respect to a reference object. If two stars are observed to have fluxes f_1 and flux f_2 respectively, we define the magnitude[2] difference between the stars as

$$m_1 - m_2 = -2.5\ log_{10}\ (\frac{f_1}{f_2}). \tag{1.2}$$

Because flux decreases as a factor of $1/r^2$, optical astronomers can calculate distances via magnitude measurements: imagine that there exists an astronomical object that always

[2]This is the Pogson magnitude difference. Other definitions, such as the asinh magnitude, exist. Typically the different magnitudes differ mainly at very small fluxes where the logarithms are poorly behaved

has the same luminosity. This type of object is called a "standard candle". If we have one of those objects near us, and another of those objects farther away from us, the difference between their magnitudes is proportional to the ratio of their respective distances

$$m_{far} - m_{near} = -5.0\ log_{10}\ (\frac{d_{near}}{d_{far}}). \tag{1.3}$$

If the specific luminosities being measured are over the same wavelength range, then we can simplify this calculation by defining an "absolute magnitude" M , the magnitude that would be observed if the object were to be at a distance of 10 pc. Then

$$m - M = 5.0\ log_{10}(d_{far}) - 5.0, \tag{1.4}$$

where the units of d_{far} are in parsecs. This quantity $m - M$ is called the distance modulus μ.

If the specific luminosities being measured are not over the same wavelength range, an extra term – the K-correction – "K" must be included:

$$m - M = K + \mu. \tag{1.5}$$

The K-correction term brings one object (typically the observed object) into the same wavelength frame as the reference object.

1.1.3 A new theory advances cosmology

The flowering of observational astronomy was matched by a flowering of theory. In 1915, Albert Einstein proposed General Relativity (GR), a new theory of space, time, and gravitation (Einstein 1915) summarized by the Einstein equation:

$$R_{\mu\nu} - \frac{1}{2} g_{\mu\nu}\ R = -\kappa\ T_{\mu\nu}. \tag{1.6}$$

In GR the curvature of space-time itself is the mechanism by which massive[3] objects experience "gravitational force", and the distribution of mass-energy in turn determines

[3] mass including energy, as per $E = mc^2$

the curvature of space-time. The left hand side of Equation 1.6 contains the information about geometry, represented by the Ricci tensor $R_{\mu\nu}$ and the metric $g_{\mu\nu}$, while the right hand side contains the information about the mass-energy distribution, represented by the stress-energy tensor $T_{\mu\nu}$.

As Einstein, de Sitter, and others quickly realized, GR had profound implications for our understanding of cosmology. As originally published, the Einstein equation implied that the large-scale geometry of the universe was evolving with time. To allow for the possibility of a static universe, the standard cosmological model at that time, Einstein published a revised version in 1917 containing a "cosmological" constant Λ:

$$R_{\mu\nu} - \frac{1}{2} g_{\mu\nu} R + \Lambda g_{\mu\nu} = -\kappa T_{\mu\nu}. \tag{1.7}$$

The cosmological solutions considered through the 20th century were first published by Alexander Friedmann in 1922 and 1924 (Friedmann 1922, 1924). Assuming (as did Einstein and de Sitter) that mass moves slowly compared to the speed of light and that the universe is homogeneous and isotropic, but also allowing the possibility that the overall scale of the universe evolves with time, the Friedmann equation[4] relates the scale of the universe $a(t)$[5] to the energy density $\varepsilon(t)$ and curvature as:

$$(\frac{\dot{a}}{a})^2 = \frac{8\pi G}{3c^2}\varepsilon(t) - \frac{\kappa c^2}{R_0^2}\frac{1}{a(t)^2} + \frac{\Lambda}{3}, \tag{1.8}$$

where κ represents the curvature-dependence of the solution, R_0 is the present-day radius of curvature, Λ is the cosmological constant, G is the gravitational constant, and c is the speed of light.

GR and the Friedmann equations made cosmography (mapping out the distances to objects in the universe) even more interesting: measuring the scale of the universe tells us not only the size of the universe – a question fascinating in its own right – but also opened the possibility for humans to peer into the cosmic past and future. Using Cepheids as

[4] as per the 1922 paper, this equation comes from the $i = k = 4$ term of the Einstein Equation

[5] The assumptions of homogeneity, isotropy, and a time-dependent scale factor give a scale $a(t)$-dependent metric, later to be called the Friedmann-LeMaitre-Robertson-Walker metric

a distance measurement tool, Edwin Hubble was the first to take advantage of this new opportunity.

1.1.4 Hubble and the expanding universe

In 1929, the astronomical techniques of spectroscopy and magnitude measurement had been in use for at least 30 years. Astronomers had correctly attributed observed shifts in the wavelengths of spectral absorption features to the relative velocity of the observed object with respect to Earth. At the same time, the absolute magnitudes of Cepheids had been calibrated and used in turn to determine the absolute magnitudes of the brightest stars in nearby galaxies, enabling these galaxy distances to be measured. Edwin Hubble combined these two sets of information and made a startling discovery: the observed velocities of nearby galaxies were linearly correlated with their distances. Hubble's original plot of velocity as a function of distance is shown in Figure 1.1.

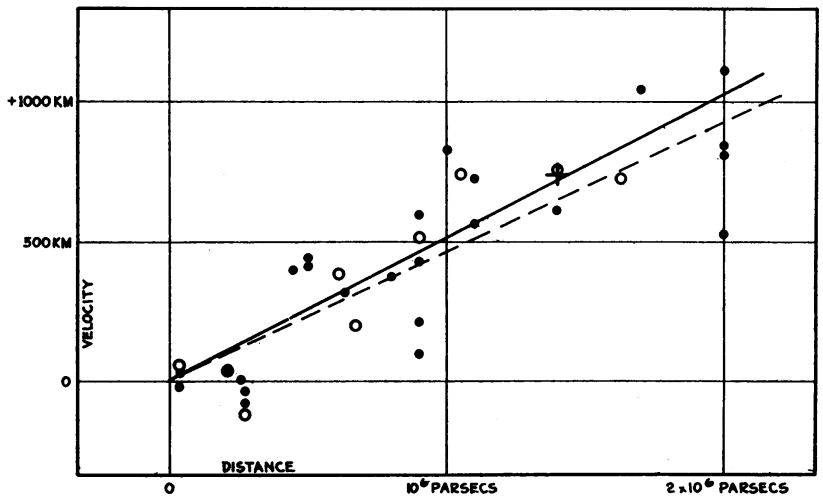

Figure 1.1 The original Hubble diagram shows radial velocities plotted as a function of distance for a collection of nearby galaxies. When the galaxies are considered individually, the best-fit velocity-distance relation is given by the solid line. The dashed line gives the best fit if the galaxies are grouped.

This plot – the original "Hubble diagram" – provided the first quantitative evidence that the scale of the universe is expanding and supported the Big Bang hypothesis formulated by Lemaître (1927). The consistent shift in the spectral feature wavelengths observed as a function of distance came to be associated with the stretching of space-time itself and labeled the "cosmological redshift". Measured redshifts provide a snapshot of the scale-factor $a(t)$ at the time the light was emitted. As postulated by Friedmann, the evolution of the scale factor with time depends on the energy density $\varepsilon(t)$ and the curvature. Perfect knowledge of both the scale factors and the energy densities as a function of time would allow us to predict distances to ancient objects. Conversely, knowing the distances of ancient objects and their scale factors allows us to measure the energy density as a function of time. For these reasons, Hubble diagrams continue to be a cornerstone of observational cosmology; extending the Hubble diagram as far back in redshift as possible is one key to understanding the composition, the past, and (perhaps) the future of our universe.

1.2 Type Ia Supernovae as Standardizeable Candles

Type Ia Supernovae are a class of Supernovae distinguished by the absence of spectral hydrogen features, and the presence of strong silicon absorption features (Wheeler & Harkness 1990). They are extremely bright and are found in both early and late-type galaxies. Although the exact progenitor system(s) and explosion mechanism remain unknown (e.g. Maoz & Mannucci 2012), there is consensus around two key issues: 1) the exploding star is most likely to be a Carbon-Oxygen white dwarf which ignites as its mass approaches the Chandrasekhar limit (Hoyle & Fowler 1960), and 2) the resulting light curve is powered by the radioactive decay of ^{56}Ni produced in abundance during the nuclear burning phase of the explosion (Axelrod 1980a,b).

The extreme luminosity ($M_B \sim -19.5$) and relative light curve homogeneity of Type Ia SNe (Kowal 1968; Pskovskii 1977) make these objects desirable as standard candles.

However, SNe Ia have been found to cover a range of absolute magnitudes (e.g. Leibundgut et al. 1993; Filippenko et al. 1992), and require standardization before they can be used as distance indicators. A relation between SN Ia light curve shapes and their absolute magnitudes was proposed by Pskovskii (1977) and established by Phillips (1993).

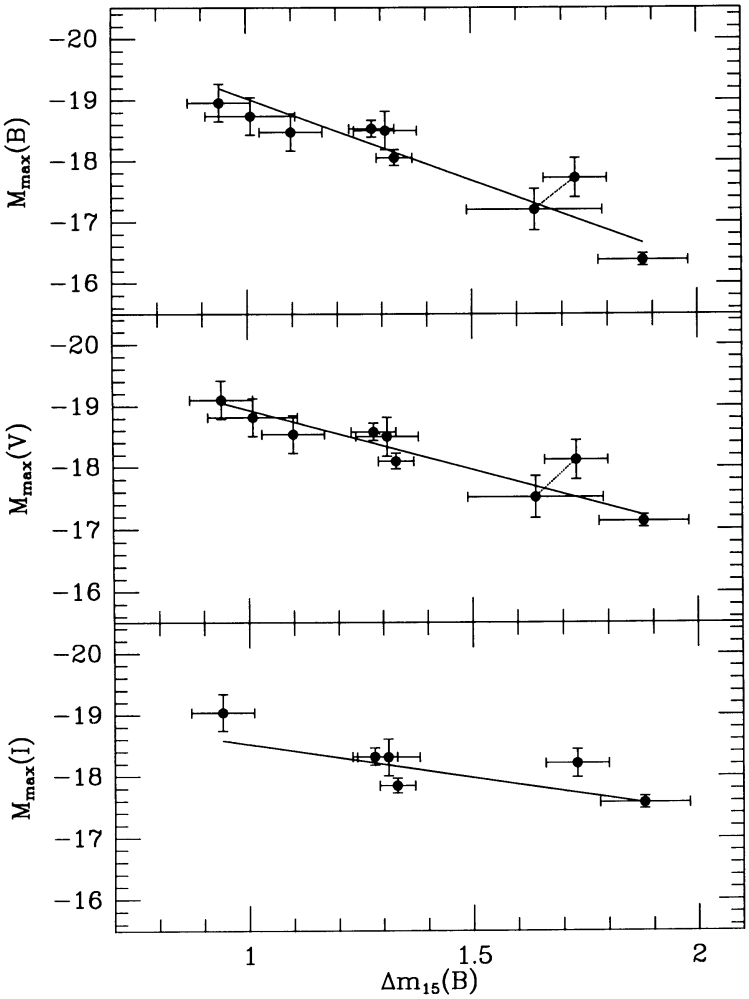

Figure 1.2 Absolute magnitude M as a function of light curve width $\Delta m_{15}(B)$, the magnitude drop in the B band light curve over the first fifteen days post-peak. Absolute magnitudes in three different broadband filters are shown: M_B(top), M_V(middle), and M_I(bottom).

Reproduced from Phillips' original paper, Figure 1.2 shows the linear relationship be-

tween SN Ia B-band absolute magnitude M_B and the light curve shape parameter $\Delta m(B)_{15}$, a light curve shape parameter defined as the decline in luminosity between SN peak and 15 days past peak. In general, broader light curves are associated with brighter luminosities, regardless of the particular variable used to parametrize the shape. A second relation between SN Ia color and absolute magnitude was found by Tripp (1998). In general, redder SNe are dimmer and bluer SNe are brighter. Although different SN Ia models differ about the extent to which this color-brightness correlation is due to dust extinction, corrections for the color-luminosity relation clearly improve the standardization of SNe Ia. Figure 1.3, adopted from Phillips et al. (1999), shows the progressive reduction in the scatter about SN Ia Hubble diagram as the width-luminosity and color-luminosity standardizations are applied to the observed SN m_B magnitudes.

Used together, light curve width and color relations produce Hubble Diagrams with residual scatter of 0.15-0.20 (Kessler et al. 2009a; Conley et al. 2011), or roughly 10% in distance.

In 1998, two separate groups (Riess et al. 1998; Perlmutter et al. 1999) independently discovered that high-redshift SN Ia distance measurements are most consistent with an accelerating universe composed mostly of "dark energy" ($\Omega_M = 0.3$, $\Omega_\Lambda = 0.7$). Observations of the Cosmic Microwave Background and large-scale galactic structure (e.g. Spergel et al. 2003; Planck Collaboration et al. 2013; Eisenstein et al. 2005; Parkinson et al. 2012) have since confirmed this result; the leaders of these groups were awarded the Nobel Prize in 2011. A Hubble diagram of their combined data set is shown in Figure 1.4, adopted from Astier (2012).

Current SN Ia cosmology efforts are focused on reducing the uncertainties in distance measurements in order to better constrain the nature of dark energy. In particular, we would like to know whether dark energy is consistent with a cosmological constant. The most recent SN Ia cosmology results (Conley et al. 2011) indicate that optical SN Ia cosmology is limited by systematics rather than statistics at all but the highest redshifts. For the increasing number of SN Ia observations to impact our understanding of dark

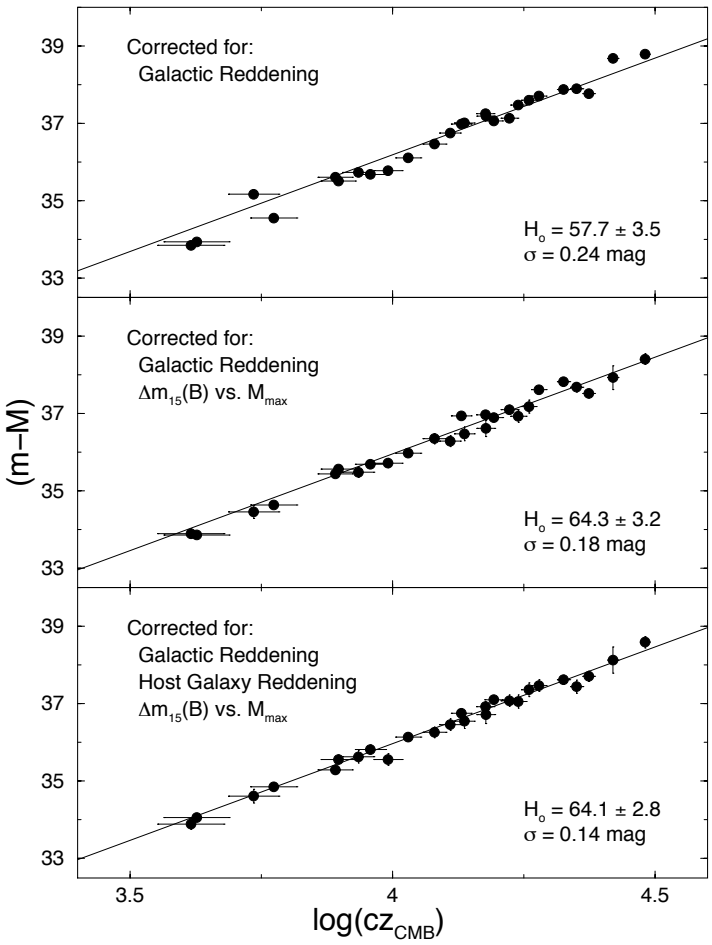

Figure 1.3 Hubble diagrams for the 26 SNe Ia in the Calan-Tololo "low-extinction" sample. The top panel has been corrected for Galactic reddening, the middle panel for Galactic reddening and light-curve width, and the bottom panel for reddening, width, and color.

energy, these systematic errors must be understood and reduced.

1.3 Key Sources of SN Ia systematic uncertainties

To accurately recover cosmology parameters from a SN Ia Hubble diagram, the Hubble diagram must not be biased as a function of redshift. The most general function for the

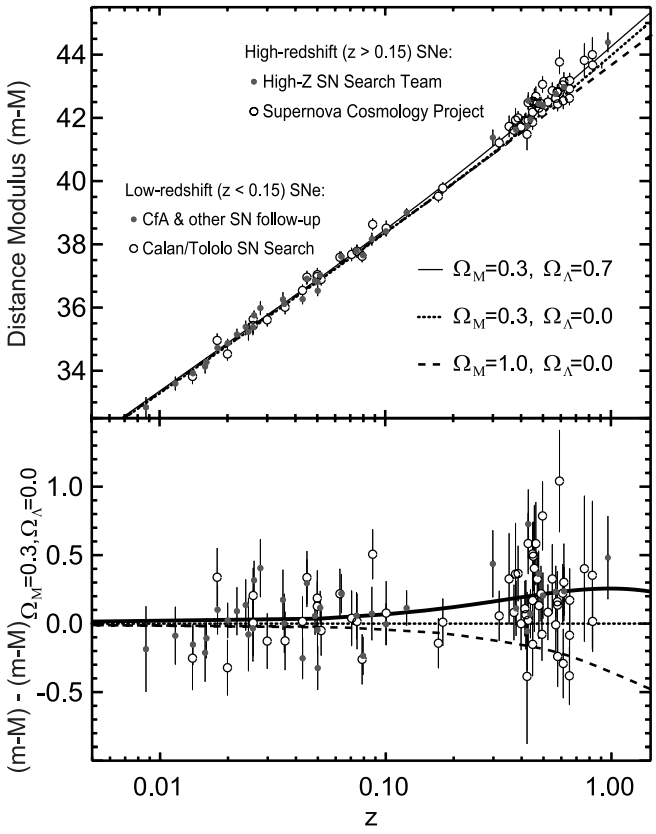

Figure 1.4 Hubble diagram of the combined High-Z and Supernova Cosmology Project data set. The top panel shows distance modulus as a function of redshift. The bottom panel shows the difference between the distance modulus and the default $\Omega_M = 0.3, \Omega_\Lambda = 0.0$ cosmology. The lines indicate the expected results for three different cosmologies: ΛCDM(solid), default(dotted), and matter-dominated(dashed). As the bottom panel clearly shows, the SN Ia data favor the ΛCDM cosmology.

SN Ia distances used to populate the Hubble diagram can be written as follows:

$$\mu = (m_x - K_{Bx}) - M_B^* - A_{x,host}(c) - \Delta M(c) - \Delta M(x1). \tag{1.9}$$

To find the distance modulus μ, we measure an observed magnitude m_x (here "x" is the filter in which m was observed), we apply a K-correction K_{Bx} to remove the effects

of cosmological redshift[6], we subtract the average B-magnitude M_B^* of SNe Ia, we use a color-dependent extinction correction $A_{x,host}$ to compensate for scattering and reemission by host galaxy dust, and finally we apply the standardization corrections $\Delta M(c)$ and $\Delta M(x1)$ related to light curve color c and shape $x1$. Examining Equation (1.9) with an eye to possible changes with redshift helps us understand the most likely sources of systematic uncertainties. In the following sections, the main sources of systematics will be discussed.

1.3.1 Calibration

The largest single current source of systematic uncertainty in SN Ia-based distance measurements is calibration (Conley et al. 2011; Sullivan et al. 2011). This can be seen in Equation (1.9): calibration uncertainties affect the observed magnitude m_x and the observed color c. If the same telescope were to observe another SN at a different redshift, such that the standardization band B corresponded to a different observer-frame band y, different calibration uncertainties would apply to the measured m_y and c. Therefore, calibration uncertainties across different filters at a single telescope have the ability to cause redshift-dependent biases. These biases are large because the corrections for extinction and color are large, typically on the order of $3 \times c$. More generally, biases in the calibration of the low-redshift sample will cause a bias in the average B-magnitude M_B^* of SNe Ia, and potentially also in the extinction law and color correction functions used to obtain extinction and color corrections $A_{x,host}(c)$ and $\Delta M(c)$.

In order to accurately combine data from different telescopes at different redshift ranges, it is important that the photometric systems of the observations be well understood. Prior to 2005, SN Ia observations were reported in the Landolt system rather than in the natural system of the telescope. The Landolt system is defined solely by its star catalog (Landolt 1992): to put photometry into the Landolt system, color transformations derived from stellar observations are applied to observed SN Ia magnitudes. The Landolt

[6]The combined term $(m_x - K_{Bx})$ is the observed magnitude m_B in the standardization band B.

standard stars are much redder than SNe Ia[7], with very different spectral features, so these transformations may not be accurate for SNe Ia (an extensive discussion of Landolt calibration of SNe photometry may be found in Regnault et al. 2009). All SN Ia surveys since 2005 have been aiming for SN Ia photometry with sub-1% calibration uncertainties. To meet these goals, photometry are being reported in the natural system of the instrument (Contreras et al. 2010; Hicken et al. 2009b; Holtzman et al. 2008; Guy et al. 2010; Tonry et al. 2012), and extensive cross-calibration efforts are being undertaken before data sets are combined Betoule et al. (e.g. 2012b).

1.3.2 Dust

Dust has always been a problem for distance measurement. Dust lying along the line of sight between the object and the detector scatters and absorbs light, decreasing the observed magnitude. To correct for dust extinction we can take advantage of the fact that dust acts preferentially on bluer light, changing observed colors as well as observed magnitudes. If the intrinsic color of an astronomical object is known, changes in observed color can be used to determine the dust extinction along a particular line of sight (e.g. Schlegel et al. (1998) use colors of elliptical galaxies to calibrate their Milky Way Galaxy dust maps), or to determine the overall absorption profile ("dust law") of the intervening dust (Cardelli et al. 1989).

Two main approaches to handling observed SN Ia color variations are used. The first method, developed by Tripp (1998) and used by light curve models SiFTo (Conley et al. 2008) and SALT (Guy et al. 2005, 2007), is to treat time-independent color variations empirically. In other words, the origin of observed time-independent SN Ia color variation is assumed to be some unknown combination of dust extinction and SN Ia physics, and no a priori assumptions are made about the intrinsic colors of any of the SNe used for model training. In this method, both the color correction as a function of wavelength

[7]Most star catalogs, Landolt or not, have colors quite different from those of SNe Ia. The Landolt requirement for color transformations just makes this worse.

and the color correction parameter[8] are determined from the supernova sample itself. With respect to Equation (1.9), this approach is like combining the dust and SN Ia color corrections $A_{x,host}(c)$ and $\Delta M(c)$ into a single term.

The second method is to assume that time-independent color variation is due solely to dust, i.e. to eliminate the SN Ia color correction term $\Delta M(c)$ altogether. This approach has been used by Phillips et al. (1999) and by the MLCS family of SN Ia models (Riess et al. 1996; Jha et al. 2007). The difficulty with this second approach as compared to the first, is that it requires the identification of a "dust-free" SN Ia sample from which intrinsic SN Ia colors may be determined. Typically, this sample is created by requiring that SNe come from dust-free regions (i.e. early-type galaxies or the outer arms of spiral galaxies) and that SN spectra show no signs of Na *I* or Ca *II* lines (Lira 1995; Riess et al. 1996).

Comparisons between SALT-II and MLCS2k2 have suggested that the MLCS2k2 approach leads to significant biases in the trained SN Ia model (Kessler et al. 2009a; Guy et al. 2010), due in part to its assumptions about the distribution of SN Ia excess color. On the other hand, studies of SN Ia spectra (Maguire et al. 2012) have found that the CCM dust law does a better job correcting for color differences than its SALT-II (Guy et al. 2010) color correction counterpart.

Regardless of the color correction law assumed, the color correction parameter obtained from SN samples is well below the one expected from studies of Milky Way Galaxy (MWG) dust: in the MWG, our dust law is $R_B \sim 4.1$, whereas dust laws determined from SNe typically have a R_B value of 3 (Kessler et al. 2009a; Conley et al. 2007; Freedman et al. 2009; Nobili & Goobar 2008).

1.3.3 Evolution

Using SNe Ia as standardizable candles to measure distances across a large range of redshifts requires assuming that the objects themselves remain the same across a large range

[8] analogous to the CCM color law "R_V" parameter in function if not physical significance

of redshifts. If this assumption is not true, a redshift-dependent distance bias will ensue, caused by shifts in average SN absolute magnitude, color, or shape.

Comparisons of SN Ia spectra at high and low redshifts have found changes in spectral feature strength and position as a function of redshift (Ellis et al. 2008; Foley et al. 2008, 2012a; Balland et al. 2009; Sullivan et al. 2009; Maguire et al. 2012), particularly in the NUV. Figure 1.5 shows such a result, adopted from Maguire et al. (2012), whose authors report a significant difference in near-UV (NUV) flux between mean low-z and high-z SNe Ia peak spectra. The dispersion as a function of wavelength, shown in the bottom panel, also confirms reports of higher dispersion in NUV SNe Ia photometry and spectra (Jha et al. 2006; Brown et al. 2010; Ellis et al. 2008).

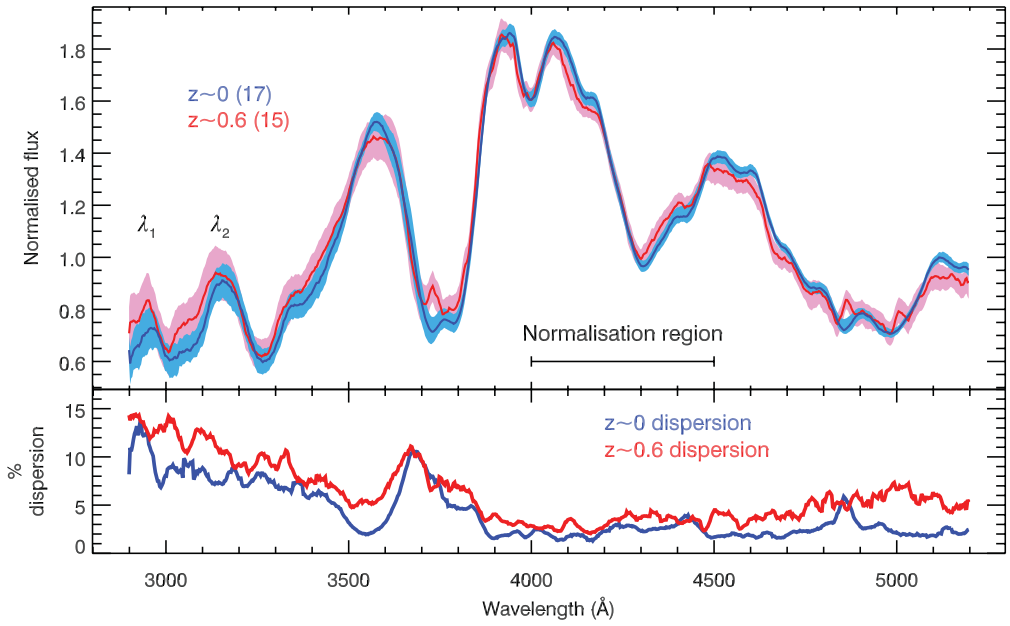

Figure 1.5 Comparisons of SN Ia flux(top panel) and dispersion(bottom panel) as a function of mean SN redshift. The mean high-z spectrum is shown in red, the mean low-z spectrum is shown in blue. Each mean spectra has been constructed from $\sim$ 16 SNe Ia spectra with stretch and redshift-corrected phases between -1.0 and 4.5 . This figure has been adopted from Maguire et al. (2012, Figure 9).

Correlations between SN Ia Hubble residuals and host galaxy mass $M_{stellar}$ have also been found, even after standardization has been taken into account (Kelly et al. 2010; Lampeitl et al. 2010; Gupta et al. 2011; Sullivan et al. 2010). Sullivan et al. (2011) have found that the color correction parameter β used by SALT-II models also varies as a function of host galaxy $M_{stellar}$, such that low-mass hosts have smaller β than high-mass hosts. Underlying SN Ia progenitor properties such as metallicity or age are thought to be responsible for these observations. Although no direct connection between SN progenitors and either of these properties has been observed, correlations between host galaxy metallicities and SN Ia Hubble residuals similar to the host mass - Hubble residual correlations have been observed (e.g. D'Andrea et al. 2011). These observed Hubble residual correlations are consistent with a shift in SN Ia progenitor metallicity as a function of redshift which one would naturally expect to occur through star formation history and galaxy evolution.

Explosion models have been used to test the effects of different progenitor metallicities on SN Ia luminosity[9]. The general conclusion is that higher metallicities favor the production of stable Fe isotopes such as ^{54}Fe and ^{58}Ni over the unstable Fe isotope ^{56}Ni which powers the light curve, thereby decreasing the absolute luminosity of the supernova (Hoeflich et al. 1998; Timmes et al. 2003; Mazzali & Podsiadlowski 2006). Radiative transfer studies which propagate these differences to light curves differ on the impact they expect this effect to have on distance measurements. Mazzali & Podsiadlowski (2006) attribute the observed ~ 0.15 magnitude intrinsic scatter in SN Hubble residuals to progenitor metallicity differences, as their models show M_B changing with metallicity while light curve shapes and optical colors remain the same. A similar study by Kasen et al. (2009) predicts only a 0.04 magnitude metallicity-induced scatter in distance measurement.

Recent theoretical studies have examined the influence of SN Ia progenitor metallicity on NUV flux. By scaling the metallicity in a set of synthetic SN Ia spectra, Walker et al.

[9] via the intermediary of ^{56}Ni production

(2012) find that for a given luminosity NUV flux (particularly in the 3000-3500 Å range) can vary by as much as a factor of two whereas optical fluxes show much less variability.

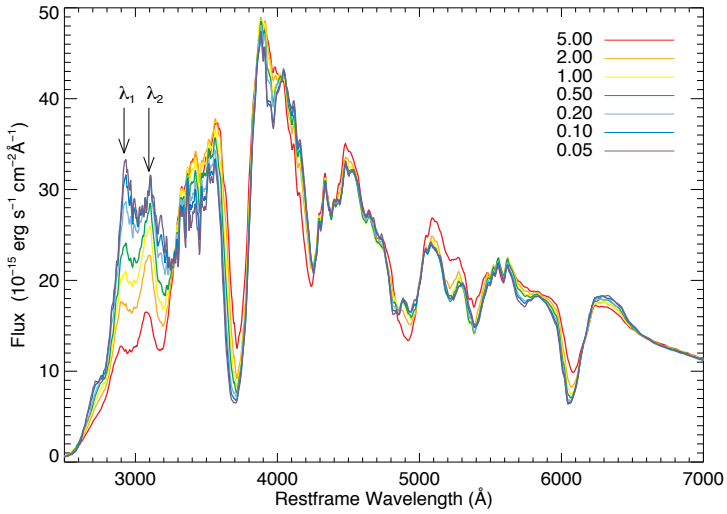

Figure 1.6 Variation in flux as a function of metallicity for a model SN Ia spectrum with bolometric luminosity $log(L_{bol}/L_{\odot}) = 9.6$. Each color corresponds to a different metallicity scaling factor η compared to a nominal value $\eta = 1$. This figure has been adopted from Figure 3 of Walker et al. (2012).

Figure 1.6, adopted from Walker et al. (2012), shows the variance in a model SN Ia spectrum[10] as the abundances of elements with $Z > 20$ are scaled by a factor η. Although some optical ($\lambda > 4000$Å) features exhibit variations in strength and position, metallicity-driven changes are much stronger in the NUV wavelength region.

This result has been used to explain the increase in dispersion observed in UV broadband and spectral flux measurements compared to the optical (Jha et al. 2006; Ellis et al. 2008; Milne et al. 2010; Maguire et al. 2012).

[10]the spectrum is based on the well-studied normal SN Ia 2005cf

1.3.4 *K*-corrections and *S*-corrections

The ability to correctly perform *K*-corrections also poses a challenge for SN distance measurements. *K*-corrections are applied to standardize photometry from different photometric systems or different cosmological redshifts. Hogg et al. (2002) provides a good general overview of the technique, Kim et al. (1996) describe the the technique for SNe Ia in particular, and Suntzeff (2000) discusses the need to use *K*-corrections to standardize photometry from different instruments ("*S*-corrections"). In order to perform *K*-corrections, a photometric system and a Spectral Energy Distribution (SED) must be assumed. Assuming an SED for SNe Ia is not obvious; their spectra vary with time, and the amount of spectral variation from object to object is not well determined, particularly in regions of SN phase space where spectra are difficult to obtain (pre-peak and UV). To compensate for SN-to-SN variation, *K*-corrections are performed with mean spectra empirically adjusted to match the observed photometric colors of the particular SN (Nugent et al. 2002; Hsiao et al. 2007).

1.4 SN Ia UV

The SN Ia UV region lies at the intersection of these four sources of systematic uncertainty.

Ground-based *U* [3000-4000 Å] observations are the most difficult to calibrate. First, the blue edge of the filter transmission is determined by atmospheric absorption, making it difficult to determine. Second, the number of calibration stars available in *U* is small compared to other broad-band filter regions, degrading the statistical determination of imaging zeropoints. Third, the colors of these calibration stars are not at all similar to the colors of SNe Ia, so a calibration that is consistent for stars may not be consistent for SNe. Taken together, the difficulty of *U* band calibration means that ground-based broadband measurements of the near UV are questionable.

The SALT-II model deweights these measurements for training, adding an extra 10%

uncertainty to their given statistical uncertainties (Guy et al. 2010); the SNLS collaboration chooses to omit all ground-based broadband measurements from their cosmology analysis (Conley et al. 2011). A comparison of cosmology parameters obtained from the same data set with the SN Ia models MLCS2k2 and SALT-II (Kessler et al. 2009a) found large differences, attributed primarily to systematic calibration offsets of the low-z UV photometry used to train MLCS2k2.

For similar reasons, ground-based UV spectra are hard to obtain, requiring spectrometers mounted on 8-10 m class telescopes. Added to the difficulty of getting low-z UV spectra, pre-peak UV spectra in any redshift range are harder to obtain.

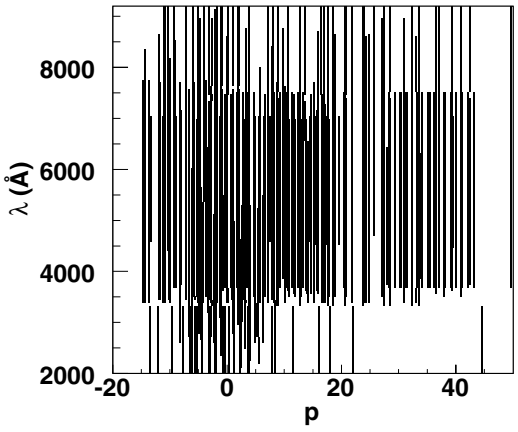

Figure 1.7 Rest frame phase and wavelength coverage of SN Ia spectra used to train the SALT-II model. This figure has been adopted from Guy et al. (2007, Figure 1).

Figure 1.7 shows the rest frame phase and wavelength coverage of the SN Ia spectra used to train the SALT-II model (adopted from Figure 1 of Guy et al. (2007)). The coverage density is largest in the 4000-6000 Å range (broadband *B* and *V* near SN peak). The wavelength limitations of ground-based photometry are obvious in the sharp cutoff in coverage below 3800 Å. Bluer wavelength coverage mostly comes from space-based telescopes, and is clustered within 5 rest-frame epochs of peak. Given the added dispersion in the UV (see Figure 1.5), the reliability of *K* and *S* corrections in this region is in

question (e.g. Foley et al. 2012b).

Lack of information about SN Ia UV spectra and colors makes the color correction law, regardless of origin, hard to determine since it is most sensitive in the UV region. Adopted from Guy et al. (2010), Figure 1.8 shows a representative range of color laws used to correct for SN Ia color variation. These color laws, regardless of the value of the color correction parameter (e.g. β or R_V), are all similar in the core wavelength region of 4000 to 6000 Å. After 6000 Å, the laws diverge slightly. However, the differences are extreme in the bluest wavelength regions: depending on which color law is used, magnitude differences for a SN Ia with color $c = 0.1$ could be as large as 0.2 at 3200 Å.

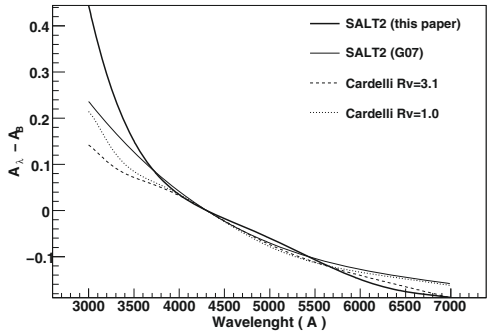

Figure 1.8 The range of color laws used to correct color variation in SN Ia observations. The SALT-II (G10) color law is shown by the thick solid curve, the SALT (G07) color law by the thin solid curve, and two variants of the CCM color law ($R_V = 1.0$ and $R_V = 3.1$) in the dotted and dashed lines, respectively. All laws are shown for $c \sim E(B-V) = 0.1$. This figure has been adopted from Guy et al. (2010), Figure 6.

Optical SN Ia Hubble diagrams depend on SN Ia rest-frame U and B to measure distances at high redshifts ($z \sim 1.0$). As shown in Figure 1.9 a SN survey such as the Dark Energy Survey (e.g. Bernstein et al. 2012) will be dependent on SN Ia rest frame U and B ($\lambda \sim 3000 - 5000$Å) for its distance measurements.

To put these high-z objects on the same footing as the lower redshift objects used for model training, it is essential that the relationship between $U-B$ and $B-V$ colors be

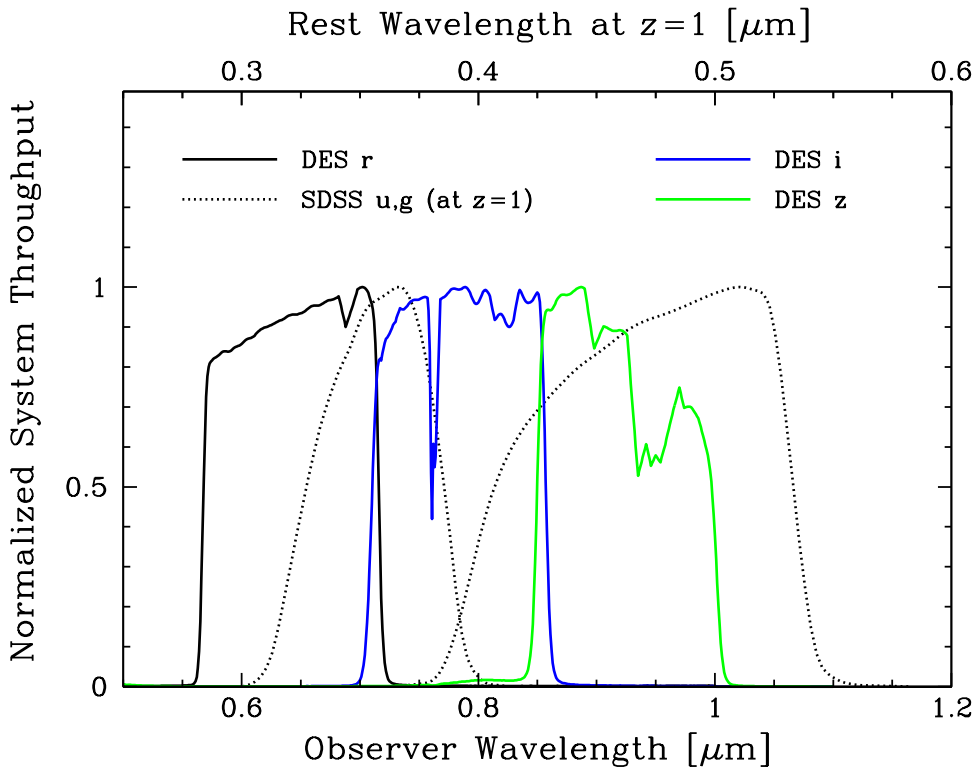

Figure 1.9 Rest frame wavelength range observed at $z \sim 1$. Observer frame DES *riz* filters are shown in solid lines. The equivalent redshifted SDSS u and g filters are overplotted in dotted lines. The bottom x-axis shows observer frame wavelengths; the top x-axis shows the equivalent rest-frame wavelengths for a SN Ia with $z = 1$.

understood. As discussed in Guy et al. (2010), underestimates of $U-B$ color dispersion lead to biased color law and color correction parameter estimates.

Furthermore, as previously mentioned, signs of metallicity-driven differences in SN Ia features are most likely to appear in the UV, and will therefore disproportionately affect high redshift SN Ia distance measurements. However, improvements in our understanding of metallicity-SN Ia luminosity correlations will be most likely to come from low-redshift SN Ia data, where distances to the SNe are well-constrained and their progenitors' local environments can be intensively studied. Therefore, efforts to understand and improve ground-based NUV photometry are well worth our while.

1.5 Overview

To use SN Ia distance measurements to constrain the nature of dark energy it is necessary to understand intrinsic SN Ia UV dispersion, SN Ia color corrections, and possible evolution of SN Ia behavior with metallicity. Although challenging, ground based UV observations of nearby SNe Ia will be important to achieving these goals, as these observations provide the most useful combination of SN observations, distance information, and host galaxy data.

In Chapter 2 I describe comparisons of photometry taken of the same SNe by two different surveys: the Carnegie Supernova Project (CSP Hamuy et al. 2006; Contreras et al. 2010; Stritzinger et al. 2011) and the SDSS-II Supernova Search (SDSS Frieman et al. 2008a). In addition to confirming the expected high quality of *BVRI* photometry of both observing programs, this work performs the first direct comparison of ground-based SN Ia U observations, and finds typical U agreement of 0.02 magnitudes and an average dispersion of 0.06 magnitudes. This work has been published (Mosher et al. 2012) and is reproduced here with minimal changes from the refereed version.

In Chapter 3 simulated SN Ia data are used to train the SALT-II SN Ia model and quantify the resulting Hubble diagram bias. For SN Ia models incorporating realistic wavelength-dependent dispersion, we find that the trained color laws are biased at blue wavelengths and observe a redshift-dependent decrease in the SALT-II color correction parameter β. However, standard bias corrections somewhat compensate for this effect. With current training sets, we find model-related bias in the dark energy equation of state parameter w to be on the order of 0.01. This work will be submitted for publication in the near future.

Chapter 4 will briefly discuss the implications of this work.

Chapter 2

Comparison of SDSS-II and CSP SN Ia photometry

Used as standard candles, Type Ia supernovae (hereafter SNe Ia) provided the first direct evidence of cosmic acceleration (Riess et al. 1998; Perlmutter et al. 1999), and hence the existence of dark energy. With cosmic acceleration having been firmly established through both SNe Ia (e.g. Tonry et al. 2003; Riess et al. 2004, 2007; Astier et al. 2006; Wood-Vasey et al. 2007; Freedman et al. 2009; Kowalski et al. 2008; Kessler et al. 2009a; Amanullah et al. 2010; Sullivan et al. 2011) and other cosmological measurements, such as the late-time integrated Sach-Wolfe effect (Giannantonio et al. 2008) and X-ray cluster distances (Allen et al. 2008), sights have now turned to understanding the time-varying nature of dark energy. Distinguishing between competing dark energy theories will require photometric precision of SNe Ia observations on the 1% level or better.

Several recent surveys have discovered and observed more than a thousand SNe Ia extending from intermediate- to high-z. Analysis of the full set of SNe Ia indicates that the precision of cosmology measurements is now limited as much by systematic as by statistical uncertainties (e.g. Hicken et al. 2009a; Kessler et al. 2009a; Guy et al. 2010; Conley et al. 2011; Sullivan et al. 2011). Systematic uncertainties are particularly acute

in the UV, specifically the observer-frame U band (Kessler et al. 2009a; Sullivan et al. 2011).

Performing highly acccurate UV observations is a challenging task. The filter response function in this region is difficult to characterize due to the significant role played by the atmosphere in determining its shape on the blue side. Rest-frame UV response functions are more variable from telescope to telescope than in the other bands, making the accurate characterization of the UV filter response function even more important. The nearby SN sample suffers from both of these problems, since it is a heterogeneous collection of data taken at many telescopes, and most of the light curve data are reported in the Landolt standard system for which the filter-response functions are not well-defined, particularly in U. For this reason, the SALT2 light curve fitter was not trained with observer frame UV (Guy et al. 2007). U-band calibration of the nearby sample was identified by Kessler et al. (2009a) as one of the main sources of the discrepancy between cosmology parameters obtained with the MLCS2k2 and SALT2 light-curve fitting models. Due to these known calibration problems, many analyses, including Kessler et al. (2009a), Conley et al. (2011) and Sullivan et al. (2011), recommend avoiding use of observer-frame UV for fitter training and cosmology.

Significant benefits can be gained from SN Ia observer-frame UV data if systematic calibration uncertainties can be reduced. Spectral observations at high and low redshifts have shown that the UV portion of the Ia spectrum, particularly below 3500 Angstroms, shows increased diversity compared to the optical (Foley et al. 2008; Ellis et al. 2008; Wang et al. 2012; Cooke et al. 2011) , even after accounting for extinction (Ellis et al. 2008). Some degree of diversity is expected due to differences in progenitor metallicities (Hoeflich et al. 1998; Mazzali 2000; Lentz et al. 2000; Timmes et al. 2003; Sauer et al. 2008). However, it is not clear that current metallicity theories can explain the observed range of dispersion (Cooke et al. 2011; Ellis et al. 2008; Wang et al. 2012). Progenitor-stellar companion interaction (Kasen 2010) and asymmetric explosions (Foley & Kasen 2011; Kasen & Plewa 2007) are other possible sources for variations in UV flux.

Although rest-frame UV photometry is arguably easier to obtain at redshifts of $z \approx 0.2$ and higher (e.g. Astier et al. 2006), low-redshift SN observations allow for the acquisition of a much wider range of ancillary data. Spectropolarimetry and very early and late-time supernova spectra are more easily obtained for low-redshift SNe; these provide valuable information about rise times, progenitor interaction, and explosion asymmetry (see for instance Leonard et al. 2005; Foley et al. 2012b; Maeda et al. 2011). Host galaxy metallicity data, especially as pertains to the SN Ia location itself, are also easier to obtain for nearby SNe and can be used to probe the host galaxy-luminosity relationship which has been recently observed by Kelly et al. (2010); Sullivan et al. (2010); Lampeitl et al. (2010); D'Andrea et al. (2011); Gupta et al. (2011). The ability to link any or all of these spectrum-based measurements to observable features in the UV light curve will be valuable for the interpretation of SN Ia observations as a function of redshift. At high redshifts, observed light-curves are limited to the bluer bands in the rest frame. At $z \approx 1.0$, the highest redshift SN observations achievable from the ground, the UV region is critical. Therefore, the interpretation of these high-redshift SNe light curves, or whether they can be used at all for cosmological studies will depend on our understanding of SN Ia rest frame UV models.

In this paper, we examine SN Ia photometry from the Carnegie Supernova Project (CSP; Hamuy et al. 2006) and the SDSS-II Supernova Survey (Frieman et al. 2008b) which are likely to make up significant fractions of future light-curve training sets. Both of these programs have invested substantial time and effort in characterizing their photometric systems and in ensuring accurate photometry. By comparing data from 10 well-observed SNe Ia in common, we will examine the consistency of their overall calibrations, particularly in the rest-frame UV. Results of these tests will help determine the viability of observer-frame UV photometry, and the utility of these data in light curve fitter retraining efforts currently underway.

Ganeshalingam et al. (2010) perform a similar comparison between CfA and LOSS *BVRI* photometry. Although they found photometry agreement to be reasonable, with

mean photometry residuals between 0.01 and 0.02 magnitudes in all bands, their scatter was much larger than expected, ranging from 0.07 to 0.11 magnitudes. It has been postulated by Foley et al. (2011) that the large scatter is due to *S*-corrections, which were not part of the Ganeshalingam et al. (2010) analysis. We will show that by incorporating *S*-corrections, which are not negligible in the redshift range of our overlap objects ($z \in 0.02 - 0.08$), we are able to obtain residual rms scatter of the levels expected, on the order of $\sigma \sim 0.05$ magnitudes.

In Section 2.1 we present an overview of the CSP and SDSS photometry, describe our *S*-correction technique, and tabulate expected systematic uncertainties. Our magnitude data, including *S*-corrected light curves, and magnitude agreement statistics, are described in Section 2.2. In Section 2.3 we look at magnitude agreement in each band in more detail, including a discussion of template vs spectrum based *S*-corrections.

2.1 Photometry

Between 2005 and 2007 the CSP low-redshift program and SDSS-II supernova survey observed 16 common objects, of which ten are spectroscopically confirmed Ia supernovae. One of these ten (SN 2006fw) has image registration discrepancies, and has been excluded from our analysis. We use the remaining nine SN Ia, listed in Table 2.1, as our sample. In subsections 2.1.1 - 2.1.4, we give an overview of how photometry was acquired and how the data were placed on a common system. Accompanying this information, Table 2.2 summarizes the AB offsets used to transform synthetic CSP and SDSS AB magnitudes to their native systems. Subsection 2.1.5 describes how interpolation was used to transfer SDSS photometry onto the observation dates of the CSP data. Subsection 2.1.6 details the systematic uncertainties expected for this analysis.

Table 2.1. Spectroscopically confirmed overlap SNe Ia

SDSS-II ID	SN IAU name	z[a]	peak MJD	Δm_{15}	MWG A_v[b]	CSP phot. version	peculiar
4524	2005gj	0.0616	53658.0	···	0.312	Prieto et al.	yes[c]
5944	2005hc	0.0459	53666.6	0.85	0.092	Contreras et al.	
6558	2005hj	0.0574	53673.9	0.72	0.121	Stritzinger et al.	yes[d]
7876	2005ir	0.0764	53684.3	0.84	0.095	Contreras et al.	
8151	2005hk	0.0131	53684.8	···	0.077	Phillips et al.	yes[e]
10805	2005ku	0.0455	53697.7	1.02	0.095	Stritzinger et al.	
17784	2007jg	0.0371	54367.0	1.17	0.330	Stritzinger et al.	
17886	2007jh	0.0401	54366.0	1.77	0.321	Stritzinger et al.	yes[f]
18890	2007mm	0.0664	54392.2	1.91	0.113	Stritzinger et al.	yes[g]

[a]Redshifts are in heliocentric frame.

[b]Taken from Schlegel, Finkbeiner, & Davis (1998) dust maps.

[c]SN 2002ic-like.

[d]SN 2005-hj like.

[e]SN 2002cx-like.

[f]SN 1986-G like.

[g]SN 1991-bg like.

Table 2.2. AB offsets for the SDSS and CSP photometric systems

	u	g	r	i
SDSS	-0.069 ± 0.005	0.021 ± 0.004	0.005 ± 0.004	0.018 ± 0.009
CSP	-0.050 ± 0.017	-0.017 ± 0.009	-0.005 ± 0.017	0.002 ± 0.017

Note. — As pointed out in Holtzman et al. (2008), the SDSS AB offsets are derived by comparing native and synthetic AB magnitudes of the solar analog stars P330E, P177D, and P041C. CSP AB offsets are obtained by comparing native and synthetic AB magnitudes of the CALSPEC standard BD+17°4708, and are consistent with zeropoints published in Contreras et al. (2010).

2.1.1 SDSS-II Supernova Survey

The SDSS-II Supernova Survey was one of three main scientific programs carried out by the SDSS-II. Supernova candidates were discovered by repeated imaging scans of a 300 deg^2 patch of sky over three fall observing seasons in 2005-7. SDSS-II *ugriz* (Fukugita et al. 1996) imaging was obtained with the SDSS camera (Gunn et al. 1998) attached to the SDSS 2.5 m telescope (Fukugita et al. 1996; Gunn et al. 2006) located at the Apache Point Observatory [APO]. Preliminary photometric processing was carried out at APO (Stoughton et al. 2002; Tucker et al. 2006). Photometric zero points for nightly frames were obtained from field stars in the Ivezić catalog (Ivezić et al. 2007). Off-site, supernova candidates were flagged for spectroscopic followup (Sako et al. 2008), and SN magnitudes were extracted from images using scene-modeling photometry (Holtzman et al. 2008) and reported in the SDSS natural magnitude system (Smith et al. 2002; Lupton et al. 1999). For a technical summary of the SDSS see York et al. (2000); further information can be found in Hogg et al. (2001), Pier et al. (2003) and Abazajian et al. (2009).

It has recently been determined that the SDSS-II SN photometry requires declination-

dependent corrections to compensate for flat-fielding issues with the PT telescope. These corrections are described in Betoule et al. (2012a); updated photometry will be released in Sako et al. (2012), and is used for this work.

In combination with the absolute flux standard BD+17°4708, the SDSS photometric system is defined by its photon-weighted filter response functions, which include SDSS filter, CCD response, telescope transmission and 1.3 standard airmass transmission. Absolute flux calibration, tying SDSS native magnitudes to the AB system, has been determined using SDSS Photometric Telescope (PT) observations of CALSPEC solar analog stars (Tucker et al. 2006). This process is described in detail in Holtzman et al. (2008). We have updated the AB offsets to reflect three recent revisions: (1) the February 2010 CALSPEC release, which altered the solar analog SEDs slightly, (2) SDSS 2.5m filter response functions (Doi et al. 2010), which apply specifically to observations taken in 2004 or later, and (3) updated SDSS PT to 2.5m linear magnitude and color transformation equations used to transfer the observed solar analog magnitudes to the SDSS 2.5 meter system. Of these three changes, the filter response function update has the largest effect, particularly on the *u*-band offset which decreases by 0.0316 magnitudes. The changes in *gri* offsets are at the millimag level or smaller.

The AB offsets $m_{AB} - m_{SDSS}$ used in this work are -0.069 ± 0.005, $+0.021 \pm 0.004$, $+0.005 \pm 0.004$ and $+0.018 \pm 0.009$ for *ugri*, respectively, where uncertainties have been calculated as per the description in Kessler et al. (2009a). These take into account internal consistency of the solar analogs as well as the uncertainty in the central wavelengths of the filter response functions.

2.1.2 CSP Supernova Program

The CSP optical (*ugriBV*) follow-up campaigns were carried out with the Direct CCD Camera attached to the Henrietta Swope 1 m telescope located at the Las Campanas Ob-

servatory (LCO). A subset of field stars from the published Smith catalog[1] were used to calibrate the local sequences used to derive nightly zeropoints. Similarly to the SDSS survey, CSP magnitudes are published in the native photometric system, defined by the SWOPE filter response functions of Stritzinger et al. (2011) and the primary standard BD+17°4708.

Preliminary throughput curves given by Hamuy et al. (2006) were updated by Contreras et al. (2010), who emphasized that the *u*-band curve remained uncertain. Definitive measurements of the CSP filter throughput curves were carried out at the telescope in 2010 using a monochromator and calibrated photodiodes (Rheault et al. 2010; Stritzinger et al. 2011). We adopt these curves in the present analysis. As with the SDSS, CSP throughput curves include filter transmission, CCD response, telescope transmission, and 1.3 standard airmass transmission.

Absolute flux calibration for the CSP *ugri* photometry is taken from the published Smith et al. (2002) magnitudes of the SDSS primary standard star BD+17°4708. Color terms are used to transform these magnitudes into the CSP native system. Analogous to the SDSS procedure, AB offsets are determined by comparing expected native CSP magnitudes with synthetic CSP photometry of BD+17°4708.[2] Using this method, the following *ugri* offsets were obtained: -0.050, -0.017, -0.005, 0.002. These values are consistent with the zeropoints published in Contreras et al. (2010). We use color term uncertainty as a proxy for the CSP offset uncertainty. Uncertainties are 0.017, 0.009, 0.017 and 0.017 mag for *ugri* (Hamuy et al. 2006). A summary of calibration information is provided in Table 2.2.

[1] As the CSP observed with both Sloan and Johnson *B* and *V* filters, only stars common to both the Landolt (Landolt 1992) and the Smith catalogs were used for calibrating the photometry of the local sequences.

[2] The specific version used for this work is bd17d4708_sticsnic_002.ascii, which may be obtained from the website `http://www.stsci.edu/hst/observatory/cdbs/calspec.html`.

Table 2.3. CSP SDSS-II Calibration Star Comparison

SN	$avg\Delta u$	$avg\Delta g$	$avg\Delta r$	$avg\Delta i$
SN 2005gj	0.014(49), 9	-0.005(31), 13	-0.008(33), 13	-0.016(57), 13
SN 2005hc	-0.041(12), 2	-0.065(104), 3	-0.028(52), 3	-0.010(40), 3
SN 2005hj	-0.093(119), 4	0.024(11), 8	0.009(12), 8	0.024(42), 8
SN 2005ir	-0.014(58), 7	0.019(30), 14	0.015(14), 14	0.017(16), 14
SN 2005hk	-0.005(46), 12	0.018(15), 15	0.019(10), 15	0.019(14), 15
SN 2005ku	0.212(764), 3	-0.017(297), 7	0.070(105), 7	0.085(78), 7
SN 2007jg	0.018(58), 8	-0.012(26), 11	-0.016(17), 11	-0.021(66), 11
SN 2007jh	0.069(68), 8	-0.037(20), 11	-0.019(20), 11	-0.003(16), 11
SN 2007mm	0.093(18), 4	0.009(46), 8	-0.0002(40), 8	0.005(61), 8

Note. — CSP stellar magnitudes have been transformed into the SDSS-II photometric system, compared with the SDSS-II magnitudes, and agreement statistics for each SN calculated. The numbers in parentheses are the rms differences given in units of thousandths of magnitudes, followed by the number of stars in common for the listed SN and band. SN 2005ku stands out as having especially poor agreement, with CSP calibration stars appearing dimmer than SDSS calibration stars by 0.2 magnitudes in the *u* bandpass. Based on this evidence, SN 2005ku has been omitted from our analysis .

2.1.3 Calibration Star Comparison

Magnitudes of calibration stars in common were transformed to the SDSS native system and compared. For the SDSS-II, we chose to use SDSS Data Release 8 (SDSS DR8; Aihara et al. 2011) "ubercal" magnitudes rather than Ivezić catalog magnitudes, to match the recalibrated SDSS-II SMP photometry data. Each bandpass of each supernova had between 2 and 14 calibration stars in common. Table 2.3 shows mean and rms calibration star agreement as a function of SN and filter. SN 2005ku stands out as having particularly poor agreement, with three of four bands differing by more than 0.06 magnitudes. The *u* band in general is notable for its lack of agreement, with four of nine SNe having mean calibration star differences of more than 0.06 magnitudes. Rather than exclude poorly agreeing SNe from our already-small data set, we have chosen to combine mean calibration star difference in quadrature with photometric uncertainty.

2.1.4 *S*-correction Procedure

Before comparing photometry from CSP and SDSS-II for a given SN Ia, it is necessary to transform the photometry to a common photometric system. This is accomplished through the use of *S*-corrections (Stritzinger et al. 2002). *S*-corrections account specifically for differences between filter response functions and are computed synthetically based on the redshift and spectral energy distribution (SED) of the object. Therefore they require models for both the native photometric system of the data and the common system to which we wish to transform to, as well as a reasonable model for the SED. Since SN Ia SEDs evolve with time, *S*-corrections must be calculated for each observed epoch. Depending on the amount of difference between filters and the underlying SED, *S*-corrections can be minimal to quite significant. As shown in the right-hand panel of Figure 2.1 , CSP to SDSS *S*-correction magnitudes for a mean SN Ia observed at a redshift of 0.04 (the typical redshift of our sample) are on the order of -0.1 magnitudes for the *u*, +0.05 magnitudes for *i*, and 0.01 magnitudes for *g* and *r*.

Table 2.4. Systematic Errors affecting synthetic CSP magnitudes

source of uncertainty	u	g	r	i
AB Offset Uncertainties	0.018	0.010	0.017	0.019
SDSS Absolute Flux Calibration	0.006	0.009	0.003	0.004
S-Correction Template	0.012	0.005	0.000	0.001
Interpolation	0.006	0.001	0.005	0.002
Total	0.023	0.014	0.018	0.020

Note. — This table summarizes sources and magnitudes of systematic errors introduced by placing CSP and SDSS photometry on a single system. In the first row, CSP and SDSS AB offset uncertainties have been combined by addition in quadrature. Row two shows the difference in SDSS magnitude that would be obtained were the absolute flux calibration to be tied to BD+17°4708 rather than Solar Analogs. Row three gives estimates of magnitude differences due to the use of templates rather than spectra in S-correction calculations. Row four gives uncertainty in the mean due to interpolation biases. For more information, see sections §2.1.1, §2.1.2, and §2.1.6.

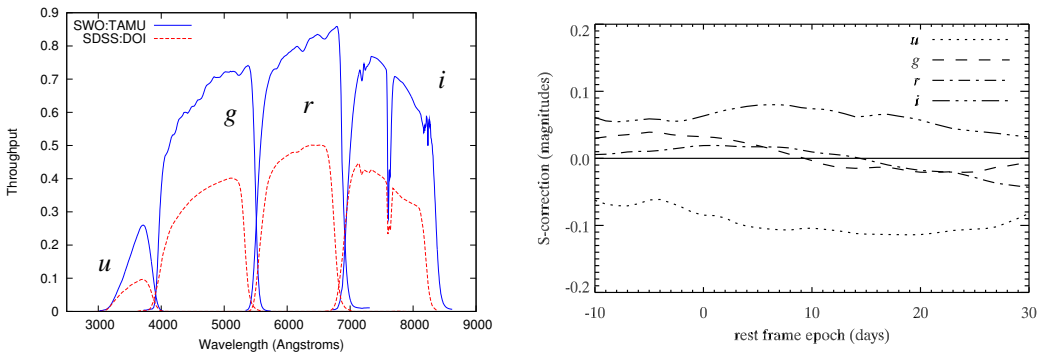

Figure 2.1 CSP and SDSS throughputs are plotted in the left panel. The right panel shows *S*-corrections for a mean SN Ia observed at a redshift of 0.04 (the average redshift of the SNe in our sample) as a function of time. A solid line has been drawn at *S*-correction equals zero to guide the eye. Descriptions of the filter response functions used can be found in Doi et al. (2010) and Stritzinger et al. (2011). Hsiao SN Ia templates have been used as a proxy for the mean SN Ia spectral energy distributions.

The *S*-correction technique described by Suntzeff (2000), Stritzinger et al. (2002), and Phillips et al. (2007) was used to transform CSP photometry to the native SDSS system. The gist of the technique is to adjust the colors of an appropriate supernova SED until they match the observed colors in the original system, then to use the adjusted template to compute synthetic photometry in the new system.

Since we do not have observed spectra corresponding to each photometric measurement, Hsiao templates[3] (Hsiao et al. 2007), were used as proxies for the time-evolving SN Ia SED. The templates were linearly interpolated to the desired rest frame epoch, redshifted, adjusted to the appropriate Milky Way Galaxy extinction using the CCM extinction law (Cardelli et al. 1989) and the dust maps of Schlegel et al. (1998), and color-matched to CSP observed photometry for the x^{th} and $(x+1)^{th}$ bands (e.g., for g-band *S*-corrections, the template was color-matched to $g-r$)[4]. Following Nugent et al. (2002),

[3]http://www.astro.uvic.ca/ hsiao/uber/index.php

[4]Since CSP optical photometry only extends through i, CSP r and i-bands were used for i -band *S*-corrections.

color-matching was done via the CCM dust extinction law (Cardelli et al. 1989). For each desired *S*-corection, a Monte Carlo routine was used to determine the variance in synthetic magnitude resulting from observed photometry uncertainties.

2.1.5 Interpolation

We interpolate SDSS light curves to obtain SDSS magnitudes on the dates of CSP photometry. Although interpolation with light-curve fitters was considered, ultimately the choice was made to use cubic splines. This decision allowed us to treat Branch-normal and peculiar SNe identically, and avoided potential systematic uncertainties that could be introduced by the set of SN data used to train the light-curve fitter. Since five of our nine SNe are peculiar (see see §2.1.6 or Table 2.1), the use of a model-independent interpolation technique was especially important for this work. We did use the MLCS2k2 light curve fitter for a limited epoch range near peak *i* band where splines had difficulty reproducing the shape of the light curve. To ensure interpolation quality, to be included in our analysis CSP photometry had to be bracketed by SDSS photometry, with at least one of those bracketing points being observed within 2 observer-frame days of the CSP epoch. We also required that interpolated magnitudes have uncertainties less than or equal to 0.05 magnitudes (0.06 magnitudes for *u*).

For most of the SNe, CSP and SDSS have very similar sampling rates. Because the rolling SDSS search discovered most of these SNe, interpolating SDSS data allows inclusion of slightly more data near peak. Therefore, seven of the nine supernovae were interpolated from SDSS photometry onto CSP observation dates. For the other two objects, SN 2005hc and SN 2007jg, we interpolated from CSP onto SDSS dates. SN 2005hc was located on the overlap area between the two SDSS-II observing strips where calibrations do not align exactly, leading to difficulties with an SDSS spline interpolation. SN 2007jg was better sampled by the CSP.

Table 2.5. SN Ia Used For *S*-Correction Uncertainty Estimation

SN IAU name	peculiar	reference	phases
u-band comparison			
1960R	·	Blaylock et al. (2000)	29
1981B	HVG	Branch et al. (1983)	0
1994D	·	Patat et al. (1996)	−11, −4, 24
1996X	·	Salvo et al. (2001)	0, 1, 7, 56, 57, 87
1999ee	·	Hamuy et al. (2002)	−11
2002bo	HVG	Benetti et al. (2004)	4, 43
2004dt	HVG	Altavilla et al. (2007)	−9, −7, −6, −4, 2, 3, 4, 10, 14
2004eo	IVG	Pastorello et al. (2007a)	−3, 2
2005cf	·	Pastorello et al. (2007b)	−8, −7, −6, −3, −2, −1, 5
gri-band comparison			
1994D	·	Patat et al. (1996)	−5, −4, −2, 2, 4, 10, 11, 24, 26, 50, 76
1998bu	·	Cappellaro et al. (2001)	10
2002bo	HVG	Benetti et al. (2004)	−4, −3, −2, −1, 4, 28, 38
2002er	·	Kotak et al. (2005)	−8, 0, 2, 4, 5, 10, 12, 13, 16, 17,20, 34
2003cg	·	Elias-Rosa et al. (2006)	−8, −7, −6, −5, −1, 1, 12, 16,26, 43
2003du	·	Stanishev et al. (2007)	−11, −7, −5, −3, −2, 1, 2, 3, 4, 6, 9, 10, 13, 17, 21, 24, 34, 37, 39, 51, 63, 72

Table 2.6. Magnitude agreement statistics: pooled data

		residual		
band	N	mean [mags]	scatter[mags]	scatter[σ]
u	32	0.001 $\pm$ 0.014	0.077	1.01
g	62	-0.002 $\pm$ 0.006	0.043	0.97
r	60	-0.002 $\pm$ 0.005	0.049	1.24
i	59	-0.011 $\pm$ 0.005	0.050	1.32

Note. — Residual is defined as CSP magnitude minus interpolated SDSS magnitude. CSP magnitudes have been *S*-corrected onto the SDSS photometric system. Residual mean and scatter have been calculated using the inverse variance as weight. To test gaussianity of the statistical errors, we have also calculated the scatter in units of the error $\equiv \Delta m/\delta m$. If errors are random, we expect this quantity to be 1.

2.1.6 Systematic Uncertainties

In this section, systematic uncertainties introduced by calibration, *S*-correction, and interpolation will be discussed and quantified. A summary of the systematic error attributable to each source is given in Table 2.4.

Absolute flux calibration and AB offsets

As described earlier in §2.1.1 and §2.1.2, SDSS-II calibration is tied to solar analog magnitudes whereas CSP calibration is tied to BD+17°4708 . If SDSS used BD+17°4708 as its absolute flux calibration, SDSS AB offsets would change to -0.0629, 0.0122, 0.0023

0.0144 magnitudes for *ugri* respectively. The differences between these two sets of offsets, 0.006, 0.008, 0.003 and 0.004 for *ugri* respectively, should be considered systematic uncertainties and are listed in row 2 of Table 2.4. We also include the CSP and SDSS AB offset errors, combined in quadrature, as systematic uncertainties.

Mismatches Between SED and Template

The *S*-correction procedure requires the use of a template SN Ia SED. Templates can introduce a systematic error in two ways. First, if the template features do not reflect average SN Ia features, the ensemble of *S*-corrections derived from the template may be biased. The Hsiao template used in this work was designed specifically to address this issue. Its features were determined by taking a weighted average of a large number of observed SN spectra, such that it represents a mean SN Ia; its suitability has been tested for K-corrections from observed frame to the rest frame *B* band, for the redshifts $0.0 < z < 0.75$. Minimal systematic offsets were observed in this band and redshift range, so long as the proper broad-band colors are used to adjust the template (Hsiao et al. 2007).

The second way in which a template SED may introduce a systematic error is if it is used with spectroscopically peculiar SNe Ia. This is a particular concern for our sample, since five of our nine supernovae are spectroscopically peculiar (see Table 2.1) . Three of these, SN 2005gj (Aldering et al. 2006; Prieto et al. 2007), SN 2005hj (Quimby et al. 2007), and SN 2005hk (Phillips et al. 2007) have been discussed in the literature. Furthermore, we have identified two more of our SNe (SN 2007jh and SN 2007mm) as peculiars using available spectra and the photometric criteria detailed in Krisciunas et al. (2009). For SN 2007jh , spectra have features consistent with a 1986G-like object: near peak this SN has a large Si II at 5800 Å to Si II at 6200 Å ratio, characteristic of fast-decliners, but lacks the strong Ti II absorption features seen in 1991bg-like objects. In addition, the *i* peak date relative to B_{max} and the weak secondary maximum are indicators of a 1986-G type fast-decliner. Only one very early (rest frame epoch -8) spectrum is available for SN 2007mm. A `SNID` fit (Blondin & Tonry 2007) of this spectrum agrees with a peculiar

classification, with 6 of the top 7 matches belonging either to SN 1999by or SN 1986G. The SN 2007mm light curve lacks a secondary peak in i and its primary maximum falls after the B_{max} date, typical of a 1991bg-like SN.

Multiple steps have been taken to minimize the effects of actual vs. template SED mismatch. For the 1986-G and 1991-bg like objects SN 2007jh and SN 2007mm, we use the Nugent 1991bg templates[5] (Nugent et al. 2002) rather than those of Hsiao. The other four peculiars have multiple observed spectra during the overlap time period. For these objects, in *gri* bands, we include only those epochs for which observed spectra were available to compute the *S*-corrections.

Finally, we quantify the systematic and statistical uncertainties in *S*-correction due to SED mismatch by calculating *S*-correction differences between observed spectra and a corresponding set of template spectra. Because we had very few spectra from the Branch-normal SNe in our sample, we used `SNID` (Blondin & Tonry 2007) to identify similar SNe for which spectra were publicly available through the SUSPECT Supernova Database[6]. In this manner, a set of 75 spectra from six SNe Ia were chosen as a comparison set for our data sample. A list of comparison SNe and references to their spectra is given in Table 2.5. To be included in this data set, the spectra had to span the rest frame g, r, and i bands, and have rest frame epochs between -20 and 80 days of peak B-band magnitude. Each SUSPECT database spectrum was warped to match the colors of its corresponding Hsiao spectrum, and *S*-corrections and *S*-correction differences were calculated for a redshift of 0.04, the mean redshift of our sample. In a similar manner, a smaller set of 32 spectra from 9 SUSPECT Supernovae was chosen to make u-band *S*-correction difference estimates. Because the numbers of spectra with rest-frame u-band coverage are small, any SN Ia spectrum with adequate wavelength coverage was used. The list of comparison u SNe is also given in Table 2.5.

Observed spectrum- template spectrum *S*-correction differences were used to calcu-

[5]Templates may be downloaded from http://supernova.lbl.gov/ nugent/nugent_templates.html

[6]http://suspect.nhn.ou.edu/ suspect/

Table 2.7. Magnitude agreement statistics: SN data

		residual	
band	SNe	mean [mags]	scatter[mags]
u	4	-0.008 $\pm$ 0.016	0.038
g	7	-0.002 $\pm$ 0.006	0.028
r	6	0.011 $\pm$ 0.005	0.025
i	7	-0.012 $\pm$ 0.005	0.032

Note. — Residual is defined as CSP magnitude minus interpolated SDSS magnitude. CSP magnitudes have been *S*-corrected onto the SDSS photometric system. Residual mean and scatter have been calculated using the inverse variance as weight.

late mean and rms scatter *S*-correction differences. Mean *S*-correction differences have been included as a systematic uncertainty, and listed in row three of Table 2.4. We find mean differences between template and spectrum-based *S*-corrections to be no greater than 0.005 magnitudes in the *g*,*r*, and *i* bands. The mean difference in *u* is 0.012 magnitudes.

The rms scatter in *S*-correction differences was found to be 0.055, 0.017, 0.012, and 0.016 for *ugri*, respectively. To properly account for spectrum-template mismatch uncertainties, these values are added in quadrature with the statistical uncertainties of each template *S*-corrected data point.

Color-matching technique

As mentioned briefly in §2.1.4, part of the *S*-correction process is the adjustment of the colors of the SN SED to match the observed SN colors. These color matching techniques have been discussed extensively in K-correction literature, which we summarize here. As

with *S*-corrections, SN Ia K-corrections are commonly computed by using a template to represent the actual supernova SED, and accounting for differences between individual SNe Ia by adjusting the colors of the template to match those computed from broad-band photometry (Nugent et al. 2002). This procedure works because K-corrections are primarily determined by the shape of the SN continuum. Two main color-adjustment techniques are in use. Nugent et al. (2002) use the CCM extinction law (Cardelli et al. 1989) to match a single color, spanning the two bands around the spectral region of interest. Others, including Hsiao et al. (2007), have suggested that a multi-color adjustment process results in a better match between the template and the actual SED, and therefore yield more accurate K-corrections compared to those made with a single-color adjustment.

However, if the single color is chosen carefully so that it spans the filter for which the magnitude is needed, there is a minimal difference between the results of the two techniques (see Hsiao et al. 2007; Figure 9). Analysis pipelines such as `SNANA` (Kessler et al. 2009b) use the single-color method because it is simpler to implement. In our case, we opt for the single-color CCM adjustment technique to enable the inclusion of *S*-corrections calculated from observed spectra. Very few observed spectra span a wavelength range that permits even a two-color adjustment. We have implemented a color selection mechanism similar to that described by Kessler et al. (2009a) to ensure that we are using the best color for a given filter and redshift. Tests have been done to check consistency between our CCM implementation and multi-color adjustment techniques. No differences have been detected for this work; therefore, our choice of color-matching is not a significant source of systematic error.

Interpolation

Based on our relatively small SN sample dominated by peculiars, and on our desire to minimize the possibility of bias in the *u*-band, it was decided to use a spline interpolation to transfer CSP magnitudes to the dates of the SDSS-II observations.

The main drawback to this choice is the potential for introducing extra scatter in the

magnitude difference results. For SNe with relatively large time gaps between data points, or relatively fast changes in light-curve shape, splines may systematically under or over-estimate magnitudes. We expect this effect to be largest in the *i*-band, due to the rapid changes in magnitude associated with the light curve secondary maximum. MLCS fits to *i* were considered, but found to also have trouble reproducing fluxes in this region. Since the magnitude of the secondary maximum is not well-correlated with width-luminosity parameters (see for example Folatelli et al. 2010), it is likely that any current model would have similar difficulties. As a precaution, our data set excluded those CSP epochs for which the nearest SDSS epoch was more than 2 rest-frame days away.

Simulations were used to test the effects of our interpolation scheme on magnitude residuals and scatter. A set of 500 low redshift (z $<=$ 0.08) SNe were simulated with a simple stretch- and color-based spectral model in `SNANA`. Since the main goal of this simulation was to test the impact of the observing cadence on interpolation uncertainties, a reasonable approximation of a SN Ia light curve was adequate. The simulations were produced with a cadence of 1 observer-frame day. From this pool of “perfect" SNe light curves, a redshift-weighted "match" was randomly chosen for each SN in our sample (excluding peculiars). The cadences of the observed data were used to create “SDSS" and “CSP" sub-sets of the simulated light curve. Finally, the “SDSS" simulation was splined onto the CSP observation dates, and the interpolations compared to the “CSP"data. A total of 200 realizations of the data set were obtained and analyzed for each filter. The same cuts were applied to the simulations as to the real data. In all cases, shifts to the mean CSP-SDSS magnitude difference due to our interpolation scheme were less than 0.006 magnitudes. These shifts are reported in the fourth row of Table 2.4, and are included as systematic uncertainties.

2.2 Results

Plots of the light curves of the SNe Ia in our sample are shown in the left panels of Figures 2.2 – 2.10. The plotted magnitudes are all in the SDSS photometric system. Photometric data used in these calculations are compiled in Tables 2.12–2.9. Magnitude residuals passing quality cuts have been plotted on the right hand panels of Figures 2.2 – 2.10 (quality cuts have been described in section §2.1.5). Two sets of error bars have been used to differentiate between uncertainty with and without calibration star disagreement. It should be noted that only some of the residuals displayed in the right hand panels of Figures 2.2 – 2.10 have been included in the data analysis. In particular, none of the template-corrected magnitudes for the spectroscopic peculiars SN 2005gj, SN 2005hj, or SN 2005hk were included. These points have been displayed in the figures to illustrate the differences between template and observed spectrum *S*-corrections. Because specialized templates were used for fast-decliners SN 2007jh and SN 2007mm, their template-corrected magnitudes have been included in the data analysis.

Two separate methods were used to obtain mean magnitude differences for each filter. First, all data for a given filter was pooled and *ugri* magnitude residual weighted means and standard deviations were calculated. These results are listed in Table 2.10. Second, individual SN mean magnitude residuals were calculated, then these values were combined. Figure 2.11 shows the SN-by-SN mean magnitude residuals as a function of filter, and the combined mean magnitude residuals are given in Table 2.11. The first method measures the typical difference and scatter in the difference for a single photometry measurement in a given filter. The second method quantifies the typical difference and scatter in the difference for any one supernova.

For the *u*, *g*, and *i* filters, these two methods give consistent agreement estimates. Two of the four mean magnitude differences, *u* and *g*, are consistent with zero – indicating agreement between the CSP and SDSS data sets – at the 1-2σ level. From this agreement, we conclude that the likelihood of significant systematic error is small in these bands. The rms error in *g* is also fairly small: 68% of individual photometry observations

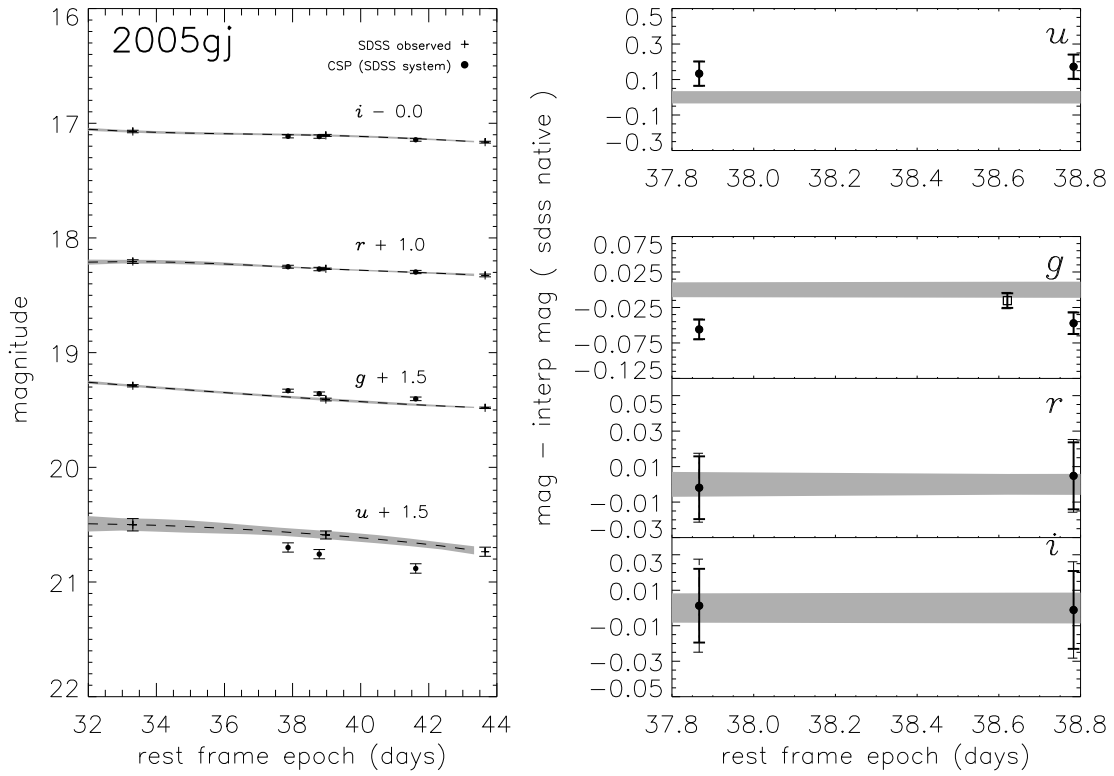

Figure 2.2 SN4524 / SN 2005gj : SDSS native photometry, *S*-corrected CSP photometry and spline fits to the SDSS photometry are shown in the left panel. The right panels show Δm, defined as *S*-corrected CSP magnitude minus interpolated SDSS magnitude plotted as a function of rest frame epoch. The shaded gray bars show the uncertainty in the interpolated SDSS magnitude. The *u*-band data are included when available.

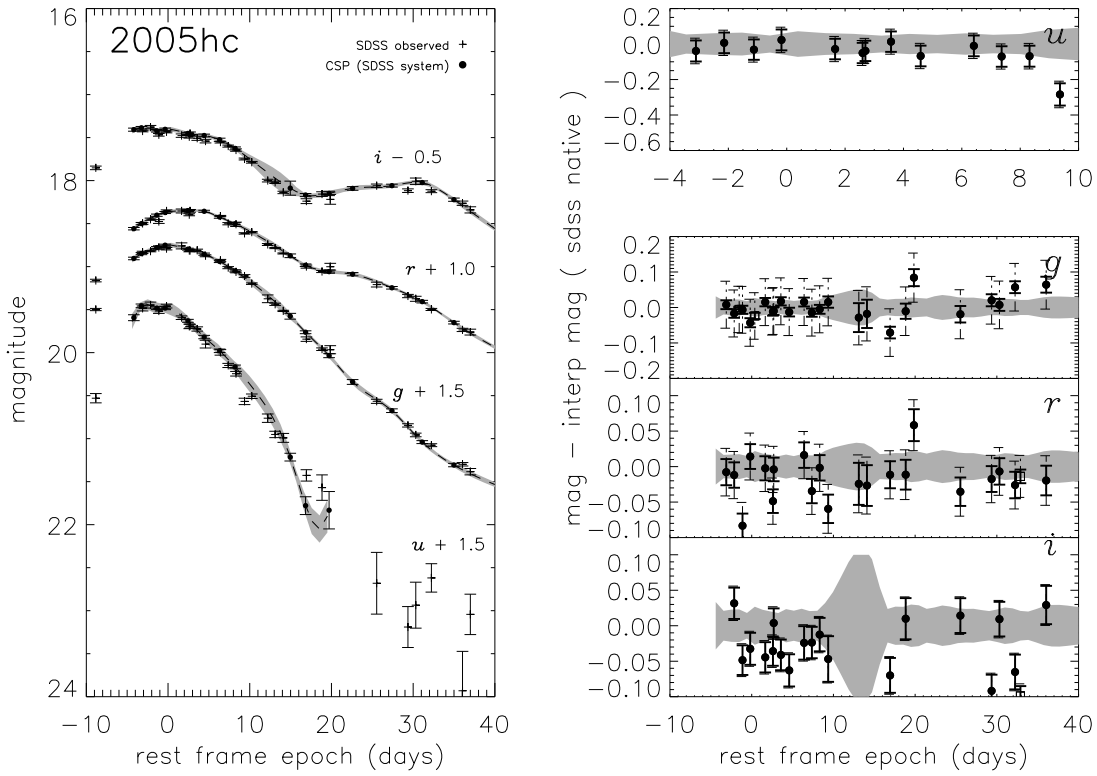

Figure 2.3 SN5944 / SN 2005hc : SDSS native photometry, *S*-corrected CSP photometry and spline fits to the CSP photometry are shown in the left panel. The right panels show Δm, defined as interpolated *S*-corrected CSP magnitude − SDSS magnitude plotted as a function of rest frame epoch. The shaded gray bars show the uncertainty in the SDSS magnitudes.

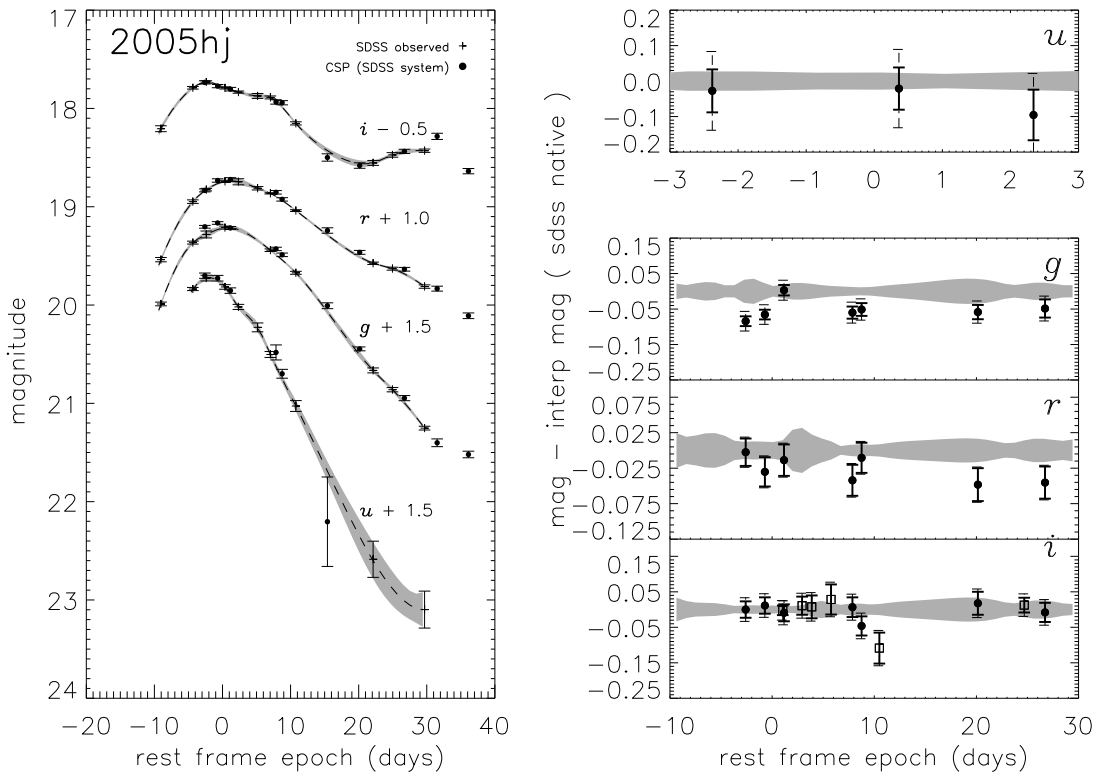

Figure 2.4 SN6558 / SN 2005hj : quantities plotted are as described in Figure 2.2.

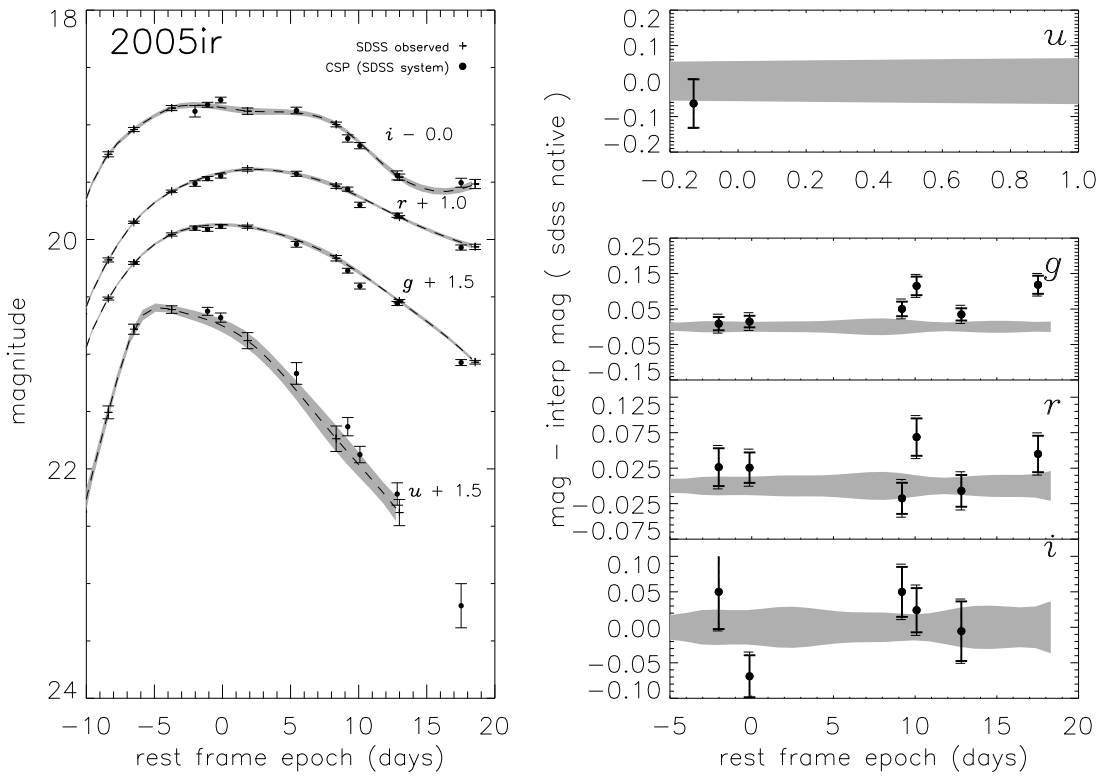

Figure 2.5 SN7876 / SN 2005ir : quantities plotted are as described in Figure 2.2.

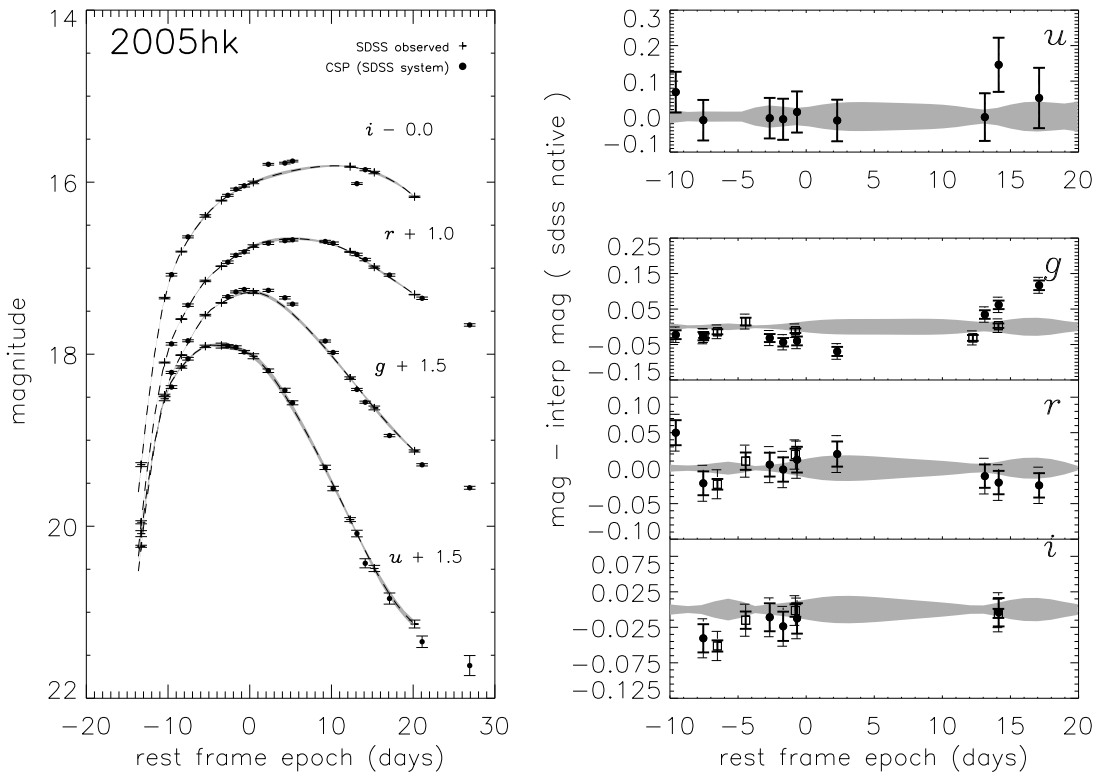

Figure 2.6 SN8151 / SN 2005hk : quantities plotted are as described in Figure 2.2.

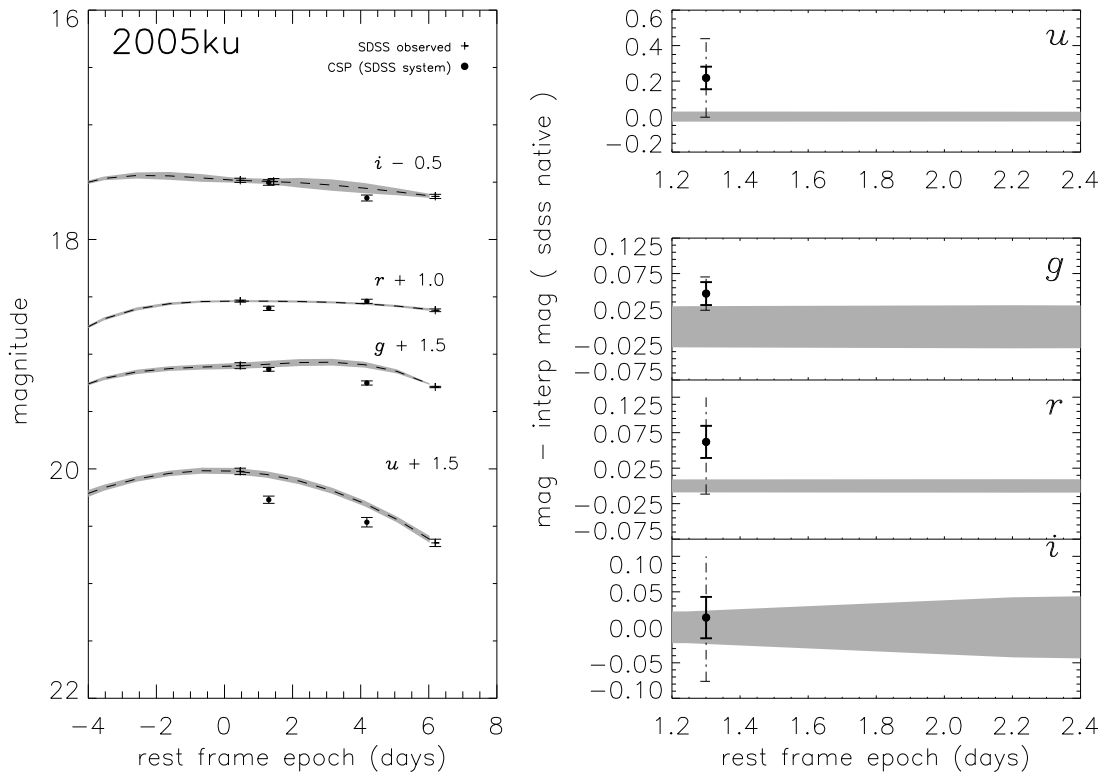

Figure 2.7 SN10805 / SN 2005ku : quantities plotted are as described in Figure 2.2.

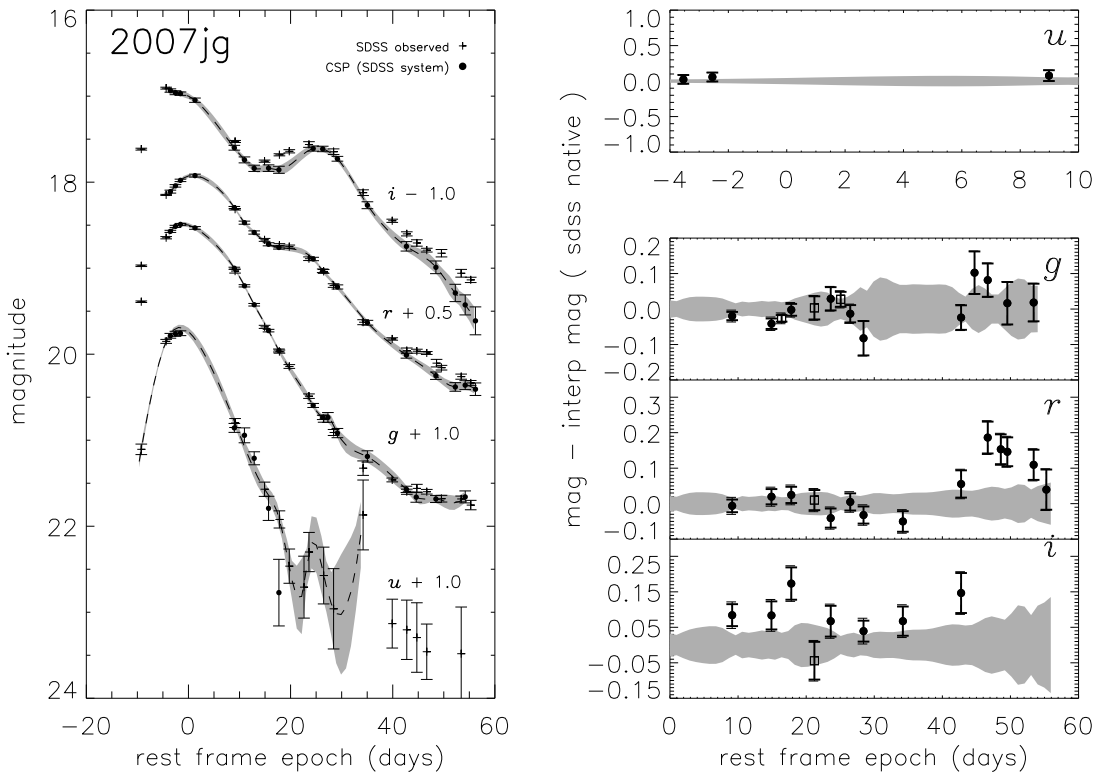

Figure 2.8 SN17784 / SN 2007jg : quantities plotted are as described in Figure 2.3.

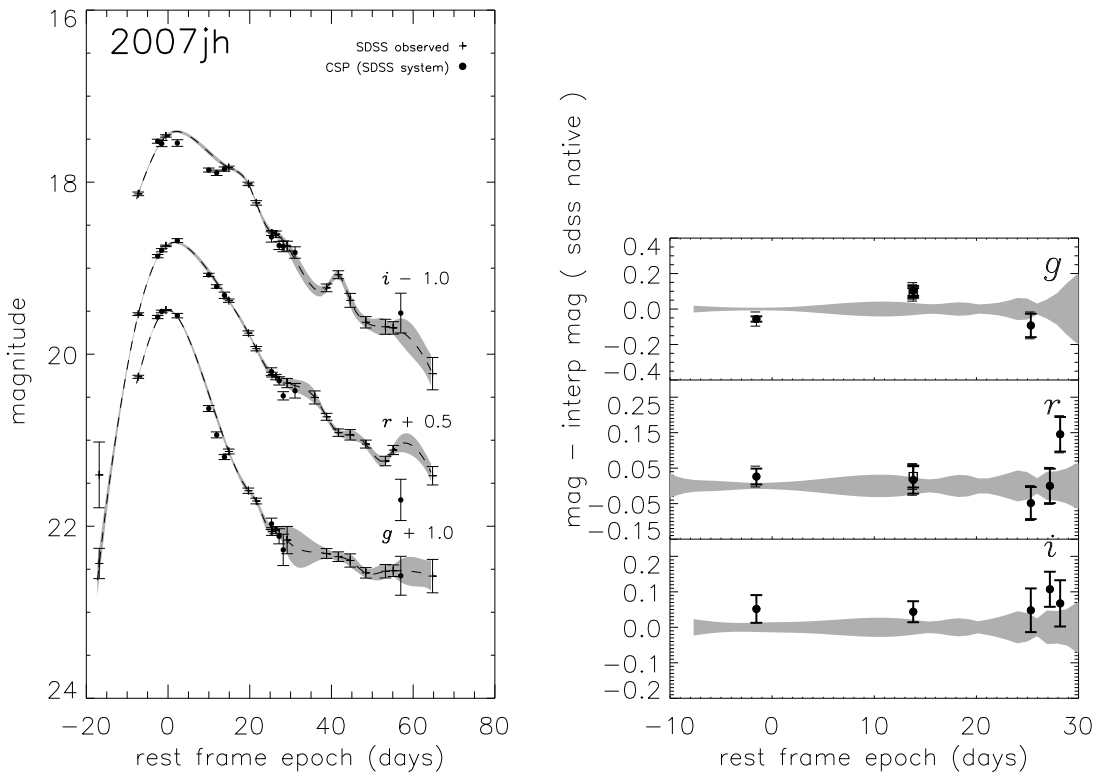

Figure 2.9 SN17886 / SN 2007jh : quantities plotted are as described in Figure 2.2.

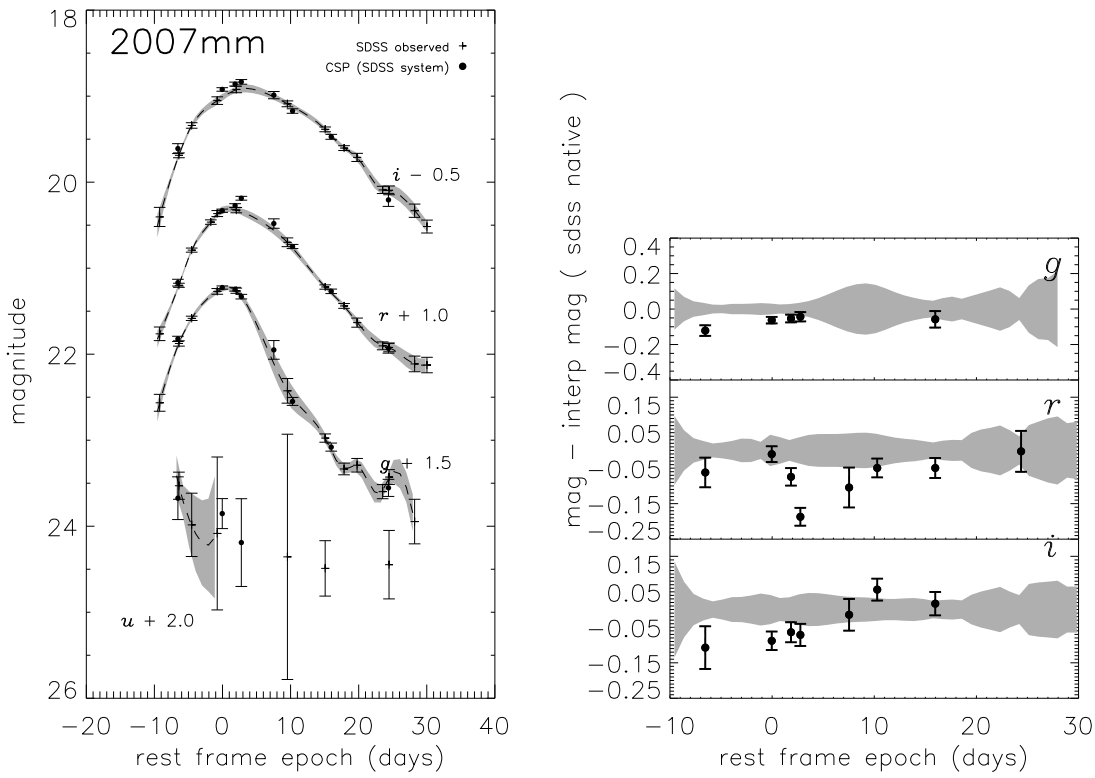

Figure 2.10 SN18890 / SN 2007mm : quantities plotted are as described in Figure 2.2.

Table 2.8. Magnitude data - *r* band

IAU	MJD	CSP(SDSS)	SDSS(native)	spectrum(1=yes)
2005hc	53663.3	17.4912(0.010)	17.4990(0.010)	0
2005hc	53664.4	17.4371(0.009)	17.4490(0.013)	0
2005hc	53665.4	17.3927(0.007)	17.4760(0.022)	0
2005hc	53666.4	17.3672(0.008)	17.3530(0.013)	0
2005hc	53668.3	17.3506(0.007)	17.3530(0.023)	0
2005hc	53669.3	17.3483(0.006)	17.3970(0.012)	0
2005hc	53669.4	17.3480(0.006)	17.3520(0.016)	0
2005hc	53673.3	17.4282(0.009)	17.4120(0.007)	0
2005hc	53674.3	17.4665(0.007)	17.5010(0.013)	0
2005hc	53675.3	17.5063(0.009)	17.5080(0.025)	0
2005hc	53676.4	17.5545(0.013)	17.6140(0.008)	0
2005hc	53680.3	17.7597(0.025)	17.7840(0.007)	0
2005hc	53681.4	17.8203(0.024)	17.8470(0.006)	0
2005hc	53684.3	17.9885(0.011)	18.0000(0.018)	0
2005hc	53686.3	18.0456(0.014)	18.0570(0.012)	0
2005hc	53687.4	18.0594(0.016)	18.0010(0.039)	0
2005hc	53693.3	18.1736(0.013)	18.2090(0.028)	0
2005hc	53697.3	18.3245(0.009)	18.3420(0.019)	0
2005hc	53698.3	18.3672(0.010)	18.3740(0.029)	0
2005hc	53700.3	18.4720(0.010)	18.4980(0.012)	0
2005hc	53704.3	18.7164(0.014)	18.7360(0.019)	0
2005ir	53682.1	18.5120(0.022)	18.4856(0.013)	0
2005ir	53684.2	18.4458(0.015)	18.4201(0.013)	0
2005ir	53694.2	18.5608(0.015)	18.5783(0.017)	0
2005ir	53695.2	18.6981(0.021)	18.6293(0.015)	0
2005ir	53698.1	18.7881(0.016)	18.7951(0.013)	0
2005ir	53703.2	19.0699(0.020)	19.0249(0.017)	0
2005ku	53699.1	17.5999(0.016)	17.5379(0.009)	0
2007jg	54376.5	17.8088(0.009)	17.8150(0.009)	0
2007jg	54382.5	18.1906(0.015)	18.1710(0.017)	0
2007jg	54385.5	18.2596(0.017)	18.2350(0.020)	0
2007jg	54391.5	18.3493(0.022)	18.3900(0.021)	0
2007jg	54394.5	18.5428(0.018)	18.5380(0.022)	0
2007jg	54396.5	18.6699(0.018)	18.7020(0.021)	0
2007jg	54402.5	19.0779(0.024)	19.1280(0.029)	0
2007jg	54411.3	19.5144(0.035)	19.4590(0.031)	0
2007jg	54415.4	19.6723(0.042)	19.4860(0.017)	0
2007jg	54417.4	19.7573(0.039)	19.6040(0.044)	0
2007jg	54418.4	19.8032(0.037)	19.6570(0.027)	0
2007jg	54422.4	19.8705(0.040)	19.7610(0.030)	0
2007jg	54424.3	19.8735(0.054)	19.8340(0.028)	0
2007jh	54364.4	18.3229(0.016)	18.2965(0.008)	0
2007jh	54380.4	18.8176(0.035)	18.8008(0.024)	0
2007jh	54392.4	19.6852(0.042)	19.7335(0.031)	0
2007jh	54394.3	19.7882(0.046)	19.7882(0.039)	0
2007jh	54395.4	19.9599(0.046)	19.8144(0.040)	0
2007mm	54385.2	20.1710(0.039)	20.2331(0.026)	0
2007mm	54392.2	19.3080(0.016)	19.3185(0.045)	0
2007mm	54394.2	19.2470(0.019)	19.3214(0.030)	0
2007mm	54395.1	19.1608(0.020)	19.3478(0.039)	0
2007mm	54400.2	19.4571(0.054)	19.5616(0.049)	0
2007mm	54403.2	19.7147(0.022)	19.7641(0.047)	0
2007mm	54409.2	20.2400(0.023)	20.2895(0.023)	0
2007mm	54418.2	20.9156(0.056)	20.9182(0.047)	0
2005hc	53701.0	18.5340(0.010)	18.5478(0.017)	1
2007jg	54389.0	18.2992(0.028)	18.2892(0.021)	1
2007jh	54380.4	18.8293(0.031)	18.8028(0.023)	1
2005gj	53699.0	17.2536(0.009)	17.2639(0.006)	1
2005hk	53678.2	16.2680(0.007)	16.2907(0.008)	1
2005hk	53680.3	16.0621(0.012)	16.0522(0.005)	1
2005hk	53684.0	15.8228(0.008)	15.8036(0.011)	1

Note. — ΔS values used in this analysis may be calculated by taking the difference of the CSP and SDSS magnitudes, and combining an extra 0.009 magnitudes in quadrature with the given uncertainties, to account for template-spectrum mismatch uncertainties.

Table 2.9. Magnitude data - *i* band

IAU	MJD	CSP(SDSS)	SDSS(native)	spectrum(1=yes)
2005hc	53664.4	17.9096(0.011)	17.8780(0.019)	0
2005hc	53665.4	17.9195(0.009)	17.9680(0.015)	0
2005hc	53666.4	17.9015(0.012)	17.9340(0.011)	0
2005hc	53668.3	17.9325(0.010)	17.9770(0.020)	0
2005hc	53669.3	17.9552(0.008)	17.9910(0.015)	0
2005hc	53669.4	17.9568(0.008)	17.9530(0.018)	0
2005hc	53670.3	17.9669(0.011)	18.0080(0.024)	0
2005hc	53671.4	17.9781(0.013)	18.0410(0.021)	0
2005hc	53673.3	18.0288(0.014)	18.0530(0.010)	0
2005hc	53674.3	18.0753(0.012)	18.0990(0.012)	0
2005hc	53675.3	18.1325(0.014)	18.1450(0.014)	0
2005hc	53676.4	18.2021(0.026)	18.2490(0.011)	0
2005hc	53684.3	18.6690(0.016)	18.7390(0.028)	0
2005hc	53686.3	18.6669(0.022)	18.6570(0.027)	0
2005hc	53693.3	18.5743(0.016)	18.5600(0.020)	0
2005hc	53697.3	18.5252(0.013)	18.6170(0.021)	0
2005hc	53698.3	18.5173(0.016)	18.5080(0.038)	0
2005hc	53700.3	18.5578(0.016)	18.6230(0.017)	0
2005hc	53704.3	18.7922(0.019)	18.7630(0.025)	0
2005ir	53682.1	18.8816(0.049)	18.8316(0.024)	0
2005ir	53684.2	18.7843(0.023)	18.8533(0.024)	0
2005ir	53694.2	19.1188(0.030)	19.0689(0.019)	0
2005ir	53695.2	19.1819(0.025)	19.1578(0.018)	0
2005ir	53698.1	19.4412(0.038)	19.4467(0.026)	0
2005ku	53699.1	18.0034(0.022)	17.9897(0.024)	0
2007jg	54363.3	17.9352(0.017)	17.9743(0.020)	0
2007jg	54364.4	17.9596(0.021)	17.9978(0.020)	0
2007jg	54376.3	18.5998(0.026)	18.5276(0.012)	0
2007jg	54378.4	18.7409(0.033)	18.6534(0.012)	0
2007jg	54383.3	18.8369(0.037)	18.7547(0.012)	0
2007jg	54385.4	18.8559(0.040)	18.6956(0.012)	0
2007jg	54392.3	18.6087(0.028)	18.5657(0.033)	0
2007jg	54397.2	18.7282(0.026)	18.7050(0.032)	0
2007jg	54403.3	19.2684(0.039)	19.1936(0.032)	0
2007jg	54411.3	19.7462(0.054)	19.6081(0.025)	0
2007jh	54364.4	18.5514(0.034)	18.4944(0.013)	0
2007jh	54380.4	18.8483(0.023)	18.7984(0.020)	0
2007jh	54392.4	19.6366(0.059)	19.5835(0.031)	0
2007jh	54394.3	19.7361(0.046)	19.6203(0.045)	0
2007jh	54395.4	19.7462(0.062)	19.6713(0.044)	0
2007mm	54385.2	20.1100(0.057)	20.2173(0.030)	0
2007mm	54392.2	19.4221(0.018)	19.5101(0.038)	0
2007mm	54394.2	19.3601(0.021)	19.4240(0.036)	0
2007mm	54395.1	19.3341(0.025)	19.4055(0.044)	0
2007mm	54400.2	19.4877(0.041)	19.5024(0.036)	0
2007mm	54403.2	19.6725(0.024)	19.6163(0.032)	0
2007mm	54409.2	19.9729(0.027)	19.9563(0.024)	0
2005hc	53701.0	18.5667(0.014)	18.6656(0.023)	1
2007jg	54389.0	18.5739(0.053)	18.6181(0.022)	1
2005hj	53675.0	18.3083(0.013)	18.3105(0.009)	1
2005hj	53677.0	18.3595(0.026)	18.3486(0.012)	1
2005hj	53678.0	18.3716(0.032)	18.3640(0.019)	1
2005hj	53680.0	18.4047(0.042)	18.3763(0.019)	1
2005hj	53685.0	18.5242(0.044)	18.6328(0.015)	1
2005hj	53700.0	18.9963(0.021)	18.9838(0.022)	1
2005hk	53678.2	16.4768(0.008)	16.5281(0.013)	1
2005hk	53680.3	16.2838(0.012)	16.2988(0.009)	1
2005hk	53684.0	16.0581(0.009)	16.0595(0.011)	1
2005hk	53699.1	15.8532(0.006)	15.8586(0.010)	1

Note. — ΔS values used in this analysis may be calculated by taking the difference of the CSP and SDSS magnitudes, and combining an extra 0.014 magnitudes in quadrature with the given uncertainties, to account for template-spectrum mismatch uncertainties.

Note. — See comments forTable 2.13.

in *g* agree at better than 0.043 magnitudes, and 68% of individual SNe will have mean photometry agreeing within 0.028 magnitudes. The *u* band scatter is quite a bit larger, with an individual data point having a 68% chance of agreeing within 0.077 magnitudes. The four SNe in our sample with 3 or more data points have an rms scatter of 0.038 magnitudes. In the *i* band, we observe an overall systematic offset of -0.011 magnitudes, inconsistent with zero at the 2.2 σ level. The scatter around this value is slightly larger than in *g*, with an point-by-point rms of 0.050 magnitudes, and a SN by SN rms of 0.032 magnitudes. Finally, the *r* band gives slightly inconsistent results between point-by-point or SN-by-SN measurements. Based on the SN-by-SN measurements shown in Table 2.11 and Figure 2.11, it appears that there is a slight systematic difference of 0.011 magnitudes between CSP and SDSS observations in this filter. The point-by-point calculation is pulled lower by some severe outlier points in SN 2007mm, which will be discussed in more detail in section §2.3.1.

Absolute magnitude differences in all bands, including *u*, are at or below 0.012 mag, regardless of the method used to compute them. In all cases magnitude differences are comparable to or smaller than the systematic uncertainties listed in Table 2.4. The rms mean scatter scales roughly as one would expect, given uncertainties from photometry, interpolation, and template mismatch. For the pooled filter averages, we also calculate the scatter in units of the error [7]. If our uncertainties are gaussian and correctly estimated, bias should follow a gaussian distribution, and should therefore have a standard deviation consistent with one. For the *u* and *g* bands, this is the case, indicating that the uncertainties are reasonable. The *r* and *i* band show slightly larger scatter, but in general are consistent.

To study our residuals in greater detail, we plot them as a function of phase, as shown in the left hand panels of Figure 2.12. For the *u* and *g* bands, outliers are randomly distributed among SNe. For instance, in the *g* band, there are 5 data points with residual magnitudes larger than $\pm$ 0.1, belonging to four different supernovae. The phases of

[7] To be precise, for the weighted average we calculate a chi-squared value rather than the bias standard deviation, but functionally they amount to the same thing.

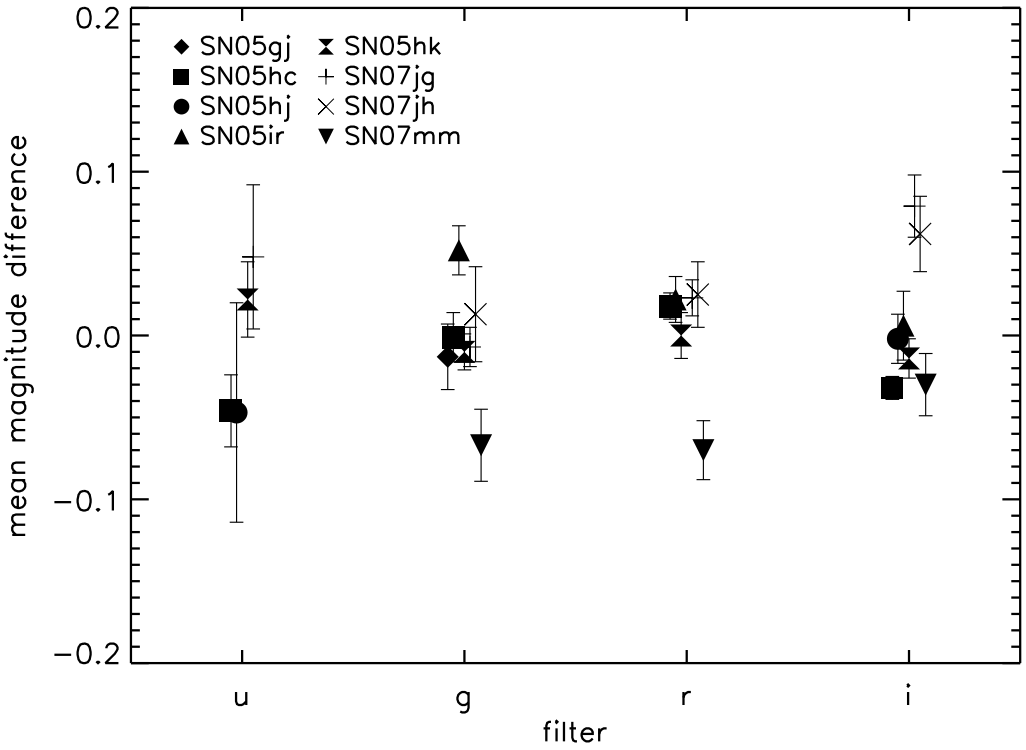

Figure 2.11 For each supernova with at least three points in a given filter, magnitude residuals have been combined into a single mean residual and plotted as a function of filter.

these points are fairly evenly distributed across the observed range of -10 to 40 rest frame days. This is less the case with the *r* band where four of the five residuals larger than 0.08 mags belong to the same supernova, SN 2007jg, and are at predominantly late times, phases larger than 30. In *i*, there appears to be a slight trend in the residual as a function of phase. A closer look at the individual SNe reveals that SN 2005hc, SN 2005hk, SN 2007jg, and SN 2007mmall show signs of residual magnitude increasing as a function of phase, particularly between phases -10 to 5. However, a fit to the residual shows no significant correlation. The right hand panels of Figure 2.12 demonstrate that all residual distributions are reasonably gaussian.

2.3 Discussion and Conclusions

In this work we have chosen to make a direct comparison of the absolute flux calibrations of the CSP and SDSS supernova surveys. This comparison is particularly interesting with respect to the observer frame *u* band, where such direct absolute flux measurements are rare, and the potential impact on cosmology results is significant. By opting for a quantitative comparison of actual SN Ia observations, we are including all possible effects that could influence agreement of SN Ia flux measurements: calibration differences, pipeline differences, S-correction differences, and template selection. These are the very same effects that will be present when this data is used for light curve fitting or light curve training. In this sense the comparison is more realistic than a calibration star analysis. On the other hand, the sample size available to us is very small (especially in the *u*-band), and the results of all of these effects are mingled. This makes it difficult for us to attribute the observed scatter in *u* (0.038 magnitudes from supernova to supernova) to any single source.

We can speculate as to the origins of the scatter. For instance, the well-observed Branch-normal SN 2005hc was located on the overlap between the SDSS-II N and S data strips, and shows a systematic offset in SDSS magnitudes between these two sets of data.

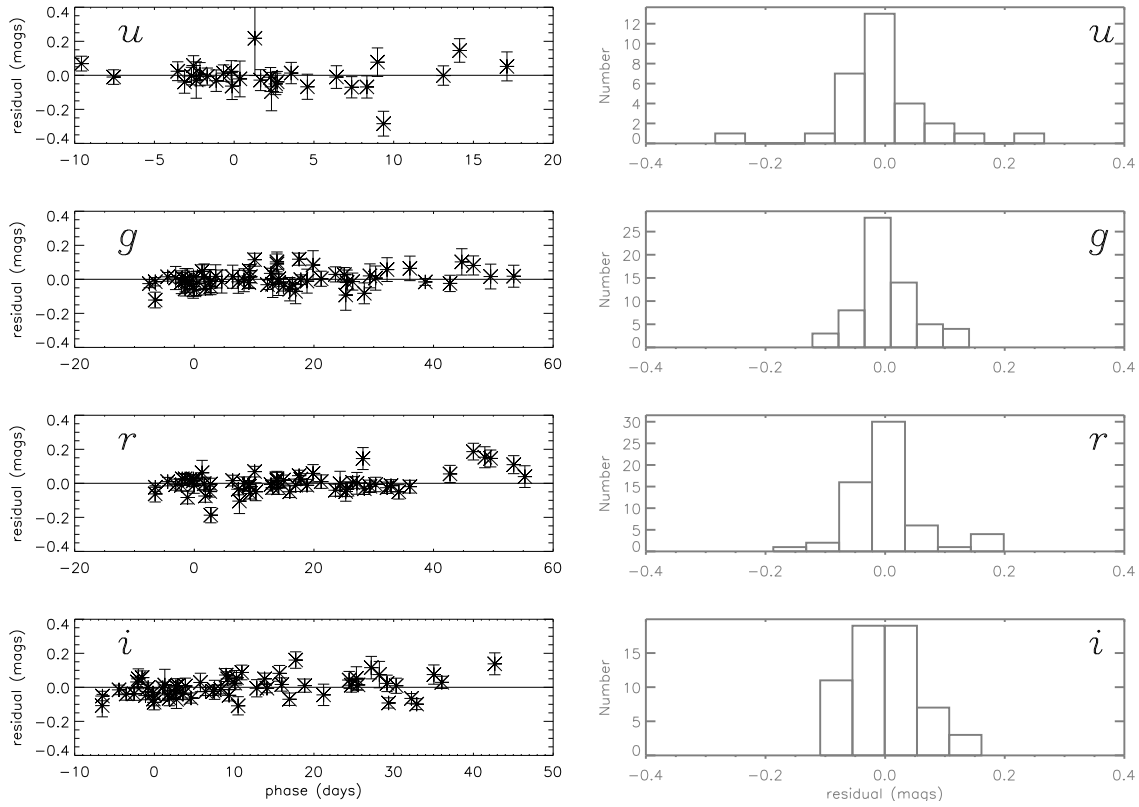

Figure 2.12 Magnitude residuals between CSP and SDSS-II data are plotted as a function of phase, and binned into histograms. A slight trend in *i*-band residual as a function of phase is observed. Similary, *i*-band residuals do not appear to be gaussianly distributed. All other bands show minimal residual variation with phase, and reasonably gaussian distributions centered on a 0.0 magnitude difference.

SN 2007jg, also a Branch-normal, had a large gap in SDSS observations near peak, and may be more likely than the rest to suffer from interpolation errors. The remaining two SNe, SN 2005hk and SN 2005hj, are both spectroscopic peculiars for which no observed *u*-band spectra are available to evaluate the suitability of the template. However, to convincingly disentangle these effects would require either a larger sample size or a selection of observed spectra for each supernova spanning at least the 3000 to 6000 Angstrom wavelength range in the supernova rest frame.

In the *gri* bands for which more data and more observed spectra are available, agreement is more convincing. As shown in Figure 2.11, the majority of the SNe cluster at similar magnitude offsets in each filter, well within the expected systematic uncertainty limits we have quantified in Table 2.4. Even so, there are one or two outliers in each band which merit discussion.

2.3.1 Outlier SNe in *gri*

As Figure 2.11 makes clear, several SNe have photometry which disagree badly in the *g*, *r*, or *i*-bands. The object SN 2007mm has a mean magnitude difference of approximately -0.07 mags in both *g* and *r*. With the exception of a ten-day gap in SDSS *g*-band coverage, it is well-enough sampled by both groups that interpolation errors should not be a problem. Based on a single early-time spectrum and the overall color evolution of this object, we have tentatively classified it as 1991-bg like, and used the Nugent 1991bg templates for its *S*-corrections. No observed spectra were available with which to check the *S*-corrections. The other fast-decliner in our sample, SN 2007jh, is an outlier in *i*. Unlike SN 2007mm, SN 2007jh does have a large gap in SDSS observations around peak B-band maximum which could possibly impact interpolated data points at the edges of the gap. This appears to be the case for the *g*-band point at rest-frame epoch 13, where both the template and the observed-spectrum *S*-corrected CSP photometry disagree with their SDSS counterpart. However, problems in *i* are not solely due to interpolation difficulties. As shown in the left-hand panel of Figure 2.9, CSP and SDSS both observed

this object near rest frame epochs -1.5 and 25.3, and in neither case is a good agreement between *S*-corrected CSP photometry and SDSS photometry obtained. Although these two objects are the faintest in our data set, the pattern of magnitude differences observed is inconsistent with CSP-SDSS galaxy subtraction differences. Therefore, we conclude that the most likely cause for the observed *g* and *r* discrepancy with SN 2007mm and *i* discrepancy with SN 2007jh is template mismatch.

Another outlier seen in the *i*-band is SN 2007jg. As with SN 2007jh, there are several points observed simultaneously by both groups whose photometry differs even after *S*-correction, suggesting that interpolation is not the source of the discrepancy. The good agreement between SN 2007jg photometry when an observed spectrum is used suggests that the observed *i* disagreement results from template mismatch. Finally, some mention should be given to SN 2005ir which shows quite a large mean magnitude disagreement in *g*-band. This supernova has the highest redshift of any of our sample, and is situated near the core of its host galaxy.The pattern of magnitude disagreement with rest frame epoch is suggestive of a galaxy subtraction difference between the two groups.

2.3.2 Stellar calibration and SN 2005hc

In order to achieve a somewhat normal distribution of outliers, it was necessary to take into consideration the individual objects' calibration star differences. Calibration star discrepancies were largest in *u*, but were instrumental in reducing outliers in *g* and *i* as well. SN 2005ku was found to have especially poor calibration star agreement. A full analysis of the calibration stars is beyond the scope of this work. A joint effort between the SDSS and SNLS collaborations includes an in-depth analysis of the those two surveys' inter-calibration, and will address in detail the discrepancies observed in the SDSS photometry and the fixes that have been deployed.

As mentioned earlier in this work, the SDSS-II Supernova Survey suffers from flat-fielding issues which have necessitated declination-dependent corrections to the photometry. Particularly affected by these flat-fielding problems were objects located on the over-

lap between the SDSS-II N and S data strips such as SN 2005hc. This Branch-normal object was very well-observed by both the SDSS and the CSP, makes up a large percentage of our data set, and continues to be over-represented in individual two and three sigma outlier data points, particularly in the *u* and *i* bands.

The effects of the combination of photometry taken on two separate CCD's on alternating observation passes can be seen in Figure 2.3. The SDSS photometry for this object shows a stair-step effect in all four bands, with the magnitude difference between the two sets of observations varying as a function of epoch. It appears that one set of observations agrees better with the CSP measurements than the other. Since this object makes up 25% of our data sample, we chose not to eliminate it, and minimized the effects of the offset by interpolating the CSP rather than SDSS data. The calculation of *S*-correction difference information from observed spectra requires interpolating both sets of photometry. Thus, interpolation difficulties with the SDSS data are the likely cause of the large discrepancy of the single observed spectrum data point in *i*.

2.3.3 Conclusions

Using SN Ia photometry, spectra, and templates, we have checked the consistency of CSP and SDSS SN Ia data. Overall, our analysis gives results well in line with expectations: in *gri* bands, we obtain photometry agreement at or below the 1% level in flux with typical epoch-to-epoch scatter no greater than 0.05 magnitudes. These results serve as a sanity check on our comparison technique. In the *u*-band, we also find observations of the CSP and SDSS to be consistent, and to agree to better than 1% in flux. At 0.077 magnitudes, the rms scatter on individual observations is larger than in the *gri* bands, but is consistent with the correspondingly larger template - spectrum *S*-correction uncertainty. However, at 0.038 magnitudes, supernova to supernova scatter is fairly large in the *u* band and our sample size is small, making it difficult to disentangle calibration, pipeline, and *S*-correction differences. Applying a conservative interpretation, we conclude that systematic offsets in observer frame *u* are equal to or less than 0.04 magnitudes, smaller

than the uncertainties currently being added to light curve fitters such as SALT2, and a promising result for ground-based observer frame *u*.

Through simulations and use of catalog spectra, we were able to quantify the biases introduced into our analysis by interpolation and the use of templates for *S*-corrections. These biases were found to be small in comparison with calibration systematics. Uncertainties due to template use were also estimated and included in our error models. Based on a selection of SUSPECT database spectra chosen to match our sample, we found that template-spectrum mismatch was much higher for the *u* band (0.055 magnitudes) than in *gr* and *i* (0.012 - 0.017 magnitudes). Therefore, more observed spectra covering the rest-frame *u* band would be required to improve this measurement.

Finally, two key points should be emphasized. First, our data set was small, and we were therefore obliged to include SNe that we might otherwise have chosen to cut. Five of the nine SNe in our sample are spectroscopic peculiars. For three of these, SN 2005gj, SN 2005hj, and SN 2005hk, we had at least some usable observed spectra, and we chose to use only this data for our *gri* sample. For others, particularly the fast-decliners SN 2007jh and SN 2007mm, we made use of specialized templates. None of the available observed spectra covered the rest frame *u* band. As a result, all of our *u*-band *S*-corrections rely on color-corrected templates. A sixth object in our data set, SN 2005hc, sat on the overlap between the SDSS-II N and S data strips, and shows a systematic offset in magnitudes between these two sets of data. Second, by using a direct comparison of supernova observations to calculate the absolute flux calibration of these two surveys, we are tacitly comparing two separate pipelines, with different photometric methods and different host galaxy subtractions. These confounding factors may be muddying the picture.

Table 2.10. Magnitude agreement statistics: pooled data

		residual		
band	N	mean [mags]	scatter[mags]	scatter[σ]
u	32	0.001 $\pm$ 0.014	0.077	1.01
g	62	-0.002 $\pm$ 0.006	0.043	0.97
r	60	-0.002 $\pm$ 0.005	0.049	1.24
i	59	-0.011 $\pm$ 0.005	0.050	1.32

Note. — Residual is defined as CSP magnitude minus interpolated SDSS magnitude. CSP magnitudes have been *S*-corrected onto the SDSS photometric system. Residual mean and scatter have been calculated using the inverse variance as weight. To test gaussianity of the statistical errors, we have also calculated the scatter in units of the error $\equiv \Delta m/\delta m$. If errors are random, we expect this quantity to be 1.

Table 2.11. Magnitude agreement statistics: SN data

		residual	
band	SNe	mean [mags]	scatter[mags]
u	4	-0.008 $\pm$ 0.016	0.038
g	7	-0.002 $\pm$ 0.006	0.028
r	6	0.011 $\pm$ 0.005	0.025
i	7	-0.012 $\pm$ 0.005	0.032

Note. — Residual is defined as CSP magnitude minus interpolated SDSS magnitude. CSP magnitudes have been *S*-corrected onto the SDSS photometric system. Residual mean and scatter have been calculated using the inverse variance as weight.

Table 2.12. Magnitude data - *u* band

IAU	MJD	CSP(SDSS)	SDSS(native)
2005hc	53663.3	17.9470(0.020)	17.9860(0.029)
2005hc	53664.4	17.9538(0.017)	17.9470(0.035)
2005hc	53665.4	17.9856(0.013)	18.0170(0.027)
2005hc	53666.4	17.9823(0.019)	17.9590(0.022)
2005hc	53668.3	18.0659(0.015)	18.0940(0.021)
2005hc	53669.3	18.1445(0.013)	18.1950(0.026)
2005hc	53669.4	18.1535(0.013)	18.1920(0.022)
2005hc	53670.3	18.2385(0.013)	18.2250(0.025)
2005hc	53671.4	18.3337(0.017)	18.4010(0.045)
2005hc	53673.3	18.4868(0.017)	18.4970(0.032)
2005hc	53674.3	18.5788(0.014)	18.6490(0.024)
2005hc	53675.3	18.6767(0.019)	18.7450(0.027)
2005hc	53676.4	18.7829(0.028)	19.0670(0.037)
2005ir	53684.2	19.1805(0.039)	19.2437(0.056)
2007jg	54363.3	18.7860(0.026)	18.7620(0.025)
2007jg	54364.4	18.7633(0.028)	18.7057(0.028)
2007jg	54376.3	19.8565(0.051)	19.7794(0.051)
2005hj	53671.4	18.1984(0.023)	18.2260(0.029)
2005hj	53674.3	18.2949(0.020)	18.3160(0.023)
2005hj	53676.4	18.4235(0.044)	18.5190(0.026)
2005hk	53675.1	16.8820(0.013)	16.8131(0.015)
2005hk	53677.1	16.5532(0.012)	16.5634(0.015)
2005hk	53682.1	16.4040(0.012)	16.4085(0.032)
2005hk	53683.1	16.4199(0.015)	16.4274(0.029)
2005hk	53684.1	16.4741(0.015)	16.4612(0.025)
2005hk	53687.1	16.6917(0.018)	16.7027(0.038)
2005hk	53698.1	18.5853(0.037)	18.5868(0.020)
2005hk	53699.1	18.9310(0.052)	18.7850(0.025)
2005hk	53702.1	19.3411(0.064)	19.2887(0.041)

Note. — ΔS values used in this analysis may be calculated directly from the table data by taking the difference of the CSP and SDSS magnitudes. To account for spectrum-template mismatch uncertainties, an extra uncertainty of 0.038 magnitudes should be combined in quadrature with the photometric uncertainties given here.

Table 2.13. Magnitude data - *g* band

IAU	MJD	CSP(SDSS)	SDSS(native)	spectrum(1=yes)
2005hc	53663.3	17.3418(0.007)	17.3340(0.013)	0
2005hc	53664.4	17.3041(0.007)	17.3210(0.007)	0
2005hc	53665.4	17.2714(0.006)	17.2780(0.020)	0
2005hc	53666.4	17.2490(0.008)	17.2920(0.014)	0
2005hc	53668.3	17.2740(0.006)	17.2590(0.035)	0
2005hc	53669.3	17.3012(0.005)	17.3130(0.015)	0
2005hc	53669.4	17.3040(0.005)	17.3140(0.010)	0
2005hc	53670.3	17.3283(0.006)	17.3110(0.014)	0
2005hc	53671.4	17.3610(0.007)	17.3740(0.011)	0
2005hc	53673.3	17.4444(0.008)	17.4290(0.013)	0
2005hc	53674.3	17.4975(0.006)	17.5120(0.012)	0
2005hc	53675.3	17.5558(0.008)	17.5610(0.011)	0
2005hc	53676.4	17.6242(0.012)	17.6090(0.016)	0
2005hc	53680.3	17.9094(0.040)	17.9380(0.013)	0
2005hc	53681.4	17.9970(0.039)	18.0150(0.007)	0
2005hc	53684.3	18.2722(0.013)	18.3430(0.026)	0
2005hc	53686.3	18.4494(0.019)	18.4600(0.015)	0
2005hc	53687.4	18.5501(0.022)	18.4660(0.047)	0
2005hc	53693.3	19.0469(0.021)	19.0660(0.024)	0
2005hc	53697.3	19.3663(0.014)	19.3460(0.019)	0
2005hc	53698.3	19.4643(0.014)	19.4570(0.021)	0
2005hc	53700.3	19.6331(0.013)	19.5760(0.017)	0
2005hc	53704.3	19.8622(0.020)	19.7980(0.020)	0
2005ir	53682.1	18.4005(0.016)	18.3917(0.016)	0
2005ir	53684.2	18.3855(0.013)	18.3708(0.014)	0
2005ir	53694.2	18.7716(0.018)	18.7213(0.022)	0
2005ir	53695.2	18.9059(0.024)	18.7907(0.018)	0
2005ir	53698.1	19.0582(0.014)	19.0233(0.014)	0
2005ir	53703.2	19.5733(0.023)	19.4549(0.014)	0
2005ku	53699.1	17.6318(0.013)	17.5850(0.030)	0
2007jg	54376.5	18.0142(0.006)	18.0340(0.023)	0
2007jg	54382.5	18.6406(0.011)	18.6820(0.018)	0
2007jg	54385.5	18.9678(0.013)	18.9700(0.018)	0
2007jg	54391.5	19.5170(0.031)	19.4880(0.026)	0
2007jg	54394.5	19.7368(0.022)	19.7500(0.041)	0
2007jg	54396.5	19.8277(0.047)	19.9100(0.035)	0
2007jg	54411.3	20.5750(0.033)	20.5990(0.030)	0
2007jg	54413.4	20.6624(0.059)	20.5600(0.047)	0
2007jg	54415.4	20.6805(0.046)	20.5990(0.027)	0
2007jg	54418.4	20.6964(0.059)	20.6800(0.039)	0
2007jg	54422.4	20.7014(0.052)	20.6830(0.034)	0
2007jh	54364.4	18.4714(0.011)	18.5278(0.008)	0
2007jh	54380.4	20.0991(0.026)	19.9968(0.035)	0
2007jh	54392.4	20.9677(0.065)	21.0601(0.047)	0
2007mm	54385.2	20.2828(0.028)	20.4044(0.033)	0
2007mm	54392.2	19.6799(0.015)	19.7425(0.030)	0
2007mm	54394.2	19.6984(0.019)	19.7518(0.029)	0
2007mm	54395.1	19.7796(0.024)	19.8230(0.037)	0
2007mm	54409.2	21.5620(0.045)	21.6200(0.049)	0
2005hc	53665.0	17.2857(0.007)	17.2912(0.015)	1
2005hc	53667.0	17.2582(0.009)	17.2821(0.025)	1
2007jg	54384.0	18.8091(0.009)	18.8353(0.016)	1
2007jg	54389.0	19.2766(0.033)	19.2733(0.024)	1
2007jg	54393.0	19.6526(0.021)	19.6252(0.032)	1
2007jh	54380.4	20.0876(0.027)	19.9969(0.034)	1
2005gj	53699.0	17.8867(0.010)	17.9020(0.011)	1
2005hk	53677.2	16.3364(0.006)	16.3616(0.005)	1
2005hk	53678.2	16.1808(0.007)	16.1949(0.008)	1
2005hk	53680.3	15.9741(0.011)	15.9594(0.006)	1
2005hk	53684.0	15.7797(0.006)	15.7907(0.012)	1
2005hk	53697.2	16.7410(0.008)	16.7724(0.016)	1
2005hk	53699.1	16.9971(0.006)	16.9940(0.015)	1

Table 2.13 (cont'd)

IAU	MJD	CSP(SDSS)	SDSS(native)	spectrum(1=yes)

Note. — ΔS values used in this analysis may be calculated by taking the difference of the CSP and SDSS magnitudes, and combining an extra 0.013 magnitudes in quadrature with the given uncertainties, to account for template-spectrum mismatch uncertainties.

Chapter 3

Measuring Hubble Diagram biases with synthetic training tests of SALT-II

3.1 Introduction

In 1998, observations of type Ia Supernovae (SNe Ia) revealed the accelerating expansion of the universe (Riess et al. 1998; Perlmutter et al. 1999), attributable to an unknown energy density called dark energy. SNe Ia-based measurements provide the only direct detection of dark energy, and as such remain a valuable component of the quest to understand this mysterious phenomena.

The cosmological utility of SNe Ia is due to their nature as standardizeable candles. Building on work by Pskovskii (1977), Phillips (1993) was the first to demonstrate that shapes of SN Ia light curves are correlated with their absolute luminosity. A second correlation between SN Ia color and luminosity was shown by Tripp (1998) and quickly confirmed by others. Although other standardization methods exist, including infrared light-curve shapes (Barone-Nugent et al. 2012; Kattner et al. 2012) and spectral ratios

(e.g. Bailey et al. 2009), the ubiquity of optical SN Ia light curve data makes shape and color standardization the most common technique.

SN light curve analysis is the process of training a SN model, using the model to determine SN light curve shape and color information, and deriving the best possible distance measurements from these SN parameters. In this paper, detailed Monte Carlo simulations (MC) are used to rigorously determine biases in the Hubble Diagram (HD) resulting from the full SN light curve analysis procedure.

Light curve analyses are performed within the framework of a SN Ia model.

SN Ia models begin with an assumption about the number of observable SN Ia parameters. As mentioned above, most SN Ia models assume that the family of SNe Ia may be described by two parameters – light curve shape and color. Models define the SN Ia rest frame flux as a function of phase, wavelength, and observable light curve parameters. Since SN Ia progenitors and explosion mechanisms remain ill-defined, models are empirically determined and must be "trained" from a subset of observed SN data for which initial light curve parameter values can be estimated. The training procedure consists of solving for the model parameters which best fit the training set of observed SN Ia data. For example, training of the magnitude-based MLCS2k2 model (Jha et al. 2007) includes solving for bandpass-dependent cofficients which relate magnitudes to light curve shapes. The training of the flux-based model SALT-II (Guy et al. 2007) includes solving for the coefficients of the spline basis functions used to represent SN Ia flux as a function of wavelength and phase.

Once the best-fit model parameters have been found, the model is ready to be used for light-curve fitting. For each SN in the data set, the trained model is used to compute synthetic observed magnitudes in conjunction with minimization routines to "fit" the most likely light curve parameters. With the data set light curve parameters in hand, distances may be calculated and an HD constructed for cosmological parameter determination.

Currently, the main source of SN Ia HD systematic uncertainty is photometric calibration (e.g. Sullivan et al. 2011). However, improved low-redshift SN Ia samples (Hicken

et al. 2009b; Holtzman et al. 2008; Stritzinger et al. 2011), greater attention to calibration (e.g. Betoule et al. 2012b), and upcoming wide-field surveys such as the DES (Bernstein et al. 2012), Pan-STARRS (Kaiser & Pan-STARRS Team 2005) and the LSST (LSST Science Collaboration et al. 2009) are reducing the significance of this contribution, and making it more important to understand systematic uncertainties related to the training and implementation of the light-curve model itself. Because the trained model is used for light-curve fitting, statistical fluctuations in the model parameters become systematic uncertainties for the fitted light curve parameters. In other words, statistical fluctuations in the model are not automatically included in the statistical uncertainties for SN color and light curve shape. Instead, these uncertainties must be added to the overall error budget by hand.

The choices of SN Ia model, training procedure, and training set can all introduce uncertainties that may affect light curve parameter measurement, and hence cosmology parameter measurement.

One way to determine model-related systematic uncertainties is to compare cosmology results from the same set of SN Ia observations evaluated with different SN Ia models. The most notable studies of model-related systematic uncertainties have been undertaken by Kessler et al. (2009a) (K09), comparing the MLCS2k2 and SALT-II models, and Guy et al. (2010) (hereafter G10), comparing SALT-II and SiFTO (Conley et al. 2008). K09 found a significant difference between MLCS2k2 and SALT-II derived cosmology parameters, which they attributed to the different handling of color for the two models and the fact that MLCS2k2 training is much more reliant on observer-frame observations in the ultraviolet region. G10 found that SALT-II and SiFTO produced consistent cosmology results.

A second approach is to estimate model uncertainties as a function of redshift directly from the model training itself. The most extensive work in this area has been done by G10 for the SALT-II model. In section 5.4.2 of their paper, G10 identify three main components of model-related systematic uncertainties in SN Ia distance measurements:

1) model choice, 2) finite training samples, and 3) wavelength-dependence of the scatter between the model and the data. As shown in Figure 16 of G10, these uncertainties have been estimated as a function of wavelength for the SALT-II model.

While these two approaches are used to estimate the model uncertainty, the true model bias cannot be determined from SN Ia observations. Therefore it is possible that systematic offsets in the trained model parameters may propagate as-yet unknown biases onto the final HD. Properly determining these biases is the focus of this work and will be instrumental to correctly interpreting SN Ia cosmology data, constructing future training sets, and designing the next generation of SN Ia models.

In this work we use simulated SN Ia samples to directly evaluate systematic biases and uncertainties originating from the SN Ia light curve analysis, with a specific focus on model training and bias corrections. We use the SALT-II model exclusively: the most recent, most precise SN Ia cosmology results are based on SALT-II light curve fits (Sullivan et al. 2011), making this state-of-the-art model an ideal choice for these systematics studies. In addition, its automated training process makes it straightforward to generate the multiple training iterations needed to evaluate biases.

We have upgraded existing SN Ia Monte Carlo simulation routines from the SN analysis software package `SNANA` (Kessler et al. 2009c) to enable accurate random realizations of the light curve and spectral data samples forming the basis of the most recent published SALT-II model training. There are two key parts to this upgrade. First, we have added a spectral simulation component, which uses an SN Ia SED model and a library of existing SN Ia spectral observations to produce spectra with realistic signal-to-noise ratios, resolution, cadences, wavelength coverage, and galaxy contamination. Second, we have added several new intrinsic scatter models (described in K12), as well as the machinery to apply them to simulated light curves or spectra.

In addition to measuring biases introduced by the training, our multiple training set realizations are used to check estimates of the statistical uncertainty of SALT-II model parameters due to the finite sizes of existing training sets and directly measure uncertainties

resulting from different choices of training parameters.

Most importantly, because the underlying cosmology and parameter distributions of the simulated training sets are known, we are able to carry out complete light curve analyses for each set of input models, all the way from model training through HD construction and cosmology fits. We use this information to evaluate HD bias as a function of redshift, and biases in the best-fit value of the dark energy equation of state parameter w. This is the first systematic study in which simulations are used to directly test uncertainties and biases resulting from SN Ia light curve analysis. The software used to run these light curve analysis tests is part of the publicly available `SNANA` supernova software package; these tools can be adapted to test any SN Ia model and data sample. This work is part of the SDSS+SNLS joint analysis.

The outline of the paper is as follows. A brief introduction to the SALT-II model and its training procedure will be given in Section §3.2. Our simulations and the data sets upon which our simulations are based will be described in Section §3.3. Section §3.4 details the input models which will be used for this work, followed by discussion of the parameters with which training results will be evaluated and the selection bias corrections that will be performed in Sections §3.5 and §3.6.

We then describe in Section §3.7 the idealized model developed as an initial test for our training and analysis pipeline, and present the results of those tests. The results of our regularization tests are presented in Section §3.8. In Section §3.9 the details of the full realistic training set are laid out, and our measurements of systematic uncertainty and bias are given. Finally we summarize the implications of the results of these tests for further SALT-II training, light curve model development, and training set observations in Section §3.10.

3.2 Training SALT2

The SALT2-II model describes SNe Ia with three components: a mean spectral time series (M_0), a shape-dependent spectral time series (M_1), and a color law (CL). The component M_0 is identified as the mean SN Ia spectral energy distribution (SED); component M_1 is associated with light curve width variations. The mean color-correction law CL incorporates all wavelength-dependent time-independent color differences regardless of origin. No assumptions about dust or extinction laws are made a priori. In addition to the best fit model, the training process also produces model uncertainties.

The flux for an individual SN Ia is determined by these components and the supernova-specific parameters x_0, x_1, and c:[1]

$$F(p,\lambda) = x_0\,[M_0(p,\lambda) + x_1 M_1(p,\lambda)]\; exp[c\,CL(\lambda)]. \tag{3.1}$$

Many more details on the SALT-II model may be found in Guy et al. (2007) and G10.

3.2.1 SALT-II model configuration

Solving for the best-fit model consists in varying the model parameters $\mathbf{M}$ to minimize the difference (i.e. χ^2) between the training set SN fluxes f and corresponding model fluxes $f_{\mathbf{M}}$. Training set fluxes obtained from spectra are compared directly with model fluxes of the same wavelength λ, whereas fluxes obtained from broad-band photometry are compared with the convolution of the model and the appropriate broad-band filter. In either case, the model is redshifted to match the redshift z of the training set SN prior to flux comparison.

Since the model fluxes depend on x_0, x_1, and c, the set of these parameters $\mathbf{x}$ must be estimated for each SN in the training set prior to calculating the χ^2:

[1] In terms of SN observables, x_0 is related to m_B, x_1 is related to light curve shape, and c is peak B$-$V color.

$$\chi^2 = \sum_{i=1}^{m} \sum_{j=1}^{n_i} \left(\frac{(f_{i,j} - f_{\mathbf{M}}(z_i, \mathbf{x_i}, \lambda_j; \mathbf{M}))^2}{(\sigma_{i,j}^D)^2 + (\sigma_{i,j}^M)^2} \right). \quad (3.2)$$

Here the uncertainty includes both the statistical uncertainty of the training flux σ^D and the uncertainty in the model flux σ^M, and the summations are over all n_i observations of all m training set SNe.

Third order b-spline basis functions are used to construct the M_0 and M_1 spectral time series. Closely resembling gaussians, third-order b-spline basis functions are parameterized by knot values, which determine the local region of phase (or wavelength) space to which each basis function contributes, and control points, which determine the vertical scale of each basis function. Only the control points are varied during the SALT-II χ^2 minimization process. The phase range -14 to 50 is spanned by 20 basis functions for a phase resolution of 3.2 days. The wavelength range 2000 to 9200 Å is spanned by 100 splines, or 72 Å per basis function. As in G10, the functional form of the color law is a polynomial with four free coefficients covering the wavelengths 2800 - 7000 Å. The best-fit color law is linearly extrapolated for wavelengths outside these regions.

Regularization

SALT-II is unique among SN Ia models in requiring a training set with flux measurements from both spectra and photometry. If a region of parameter space lacks spectral training data, the M_0 and M_1 components are constrained solely with deconvolved broadband photometry. The deconvolution process introduces high-frequency noise, causing "ringing" in model spectra in the poorly constrained region. An example of a poorly-constrained model spectrum is shown in Figure 3.1.

Extra "regularization" terms can be added to the training χ^2 to disfavor models with rapid fluctuations and to favor models which transition smoothly from one basis function to the next. The addition of these regularization terms reduces the amount of ringing trained into the model, thereby reducing statistical uncertainties on fitted light curve parameters. However, regularization can also bias the best-fit model and must be used

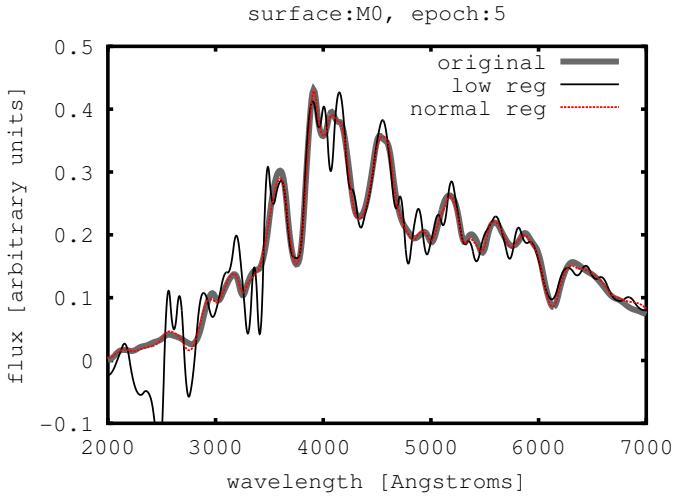

Figure 3.1 M_0 (phase=5) from a training with no spectral data between phases 2 and 8. Weak regularization shown in black, default regularization shown in red; for reference the input model is shown in thick gray.

judiciously.

To confine the effects of regularization to regions most likely to benefit, the regularization χ^2 terms are multiplied by a local weighting function $\omega(p,\lambda)$ inversely proportional to the number of training set spectral flux measurements $n(p,\lambda)$ constraining that region of phase space:

$$\omega(p,\lambda) = \begin{cases} \frac{w}{n(p,\lambda)}, & \text{if } n(p,\lambda) < 1 \\ 0, & \text{if } n(p,\lambda) \geq 1. \end{cases} \tag{3.3}$$

Figure 3.2 shows $n(p,\lambda)$ as a function of wavelength for four different phase values. Near peak, wavelengths between 4000 and 8000 Å do not use regularization, whereas most wavelength bins are regularized at early and late times.

As described in the appendix of G10, two types of regularization are used for the SALT-II model: gradient and dyadic. Gradient regularization penalizes changes in flux with respect to wavelength, whereas dyadic regularization favors fluxes which are simple interpolations from adjacent phase and wavelength grid points. The strength of each type

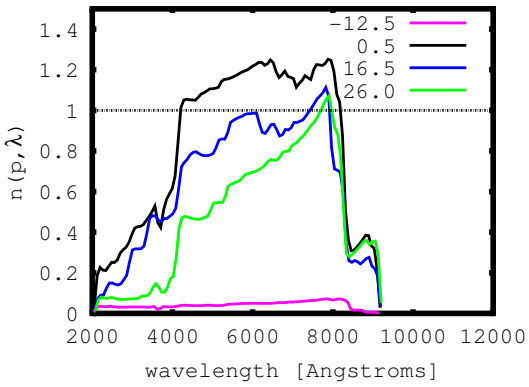

Figure 3.2 The number of spectral flux measurements constraining each phase-wavelength region of the SALT-II model is shown for a selection of phases. The dotted line shows the n value above which regularization weight $\omega(p,\lambda)$ is set to zero.

of regularization can be scaled independently, by altering the parameter w (e.g. Equation (3.3)).

As designed, regularization only affects parameter space regions with little or no spectroscopic data and strongly favors constraining them with nearby flux information, limiting biases on color. Figure 3.3 gives an example of the relative impacts of the n and w values on the best-fitting basis functions for an early phase in the UV region.

The choices of regularization type, weight w, and threshold setting will be discussed further in Section §3.8.

Recalibration

To account for spectral flux calibration inconsistencies, input training spectra are adjusted to match the best-fit model of their input light curve data. The adjustment is done by multiplying the input spectra by the exponential of a polynomial, the order of which is determined by the number of available light curves and the wavelength range of the spectrum. Typically the wavelength node points are separated by 1000 Å, roughly the width of a broad-band filter.

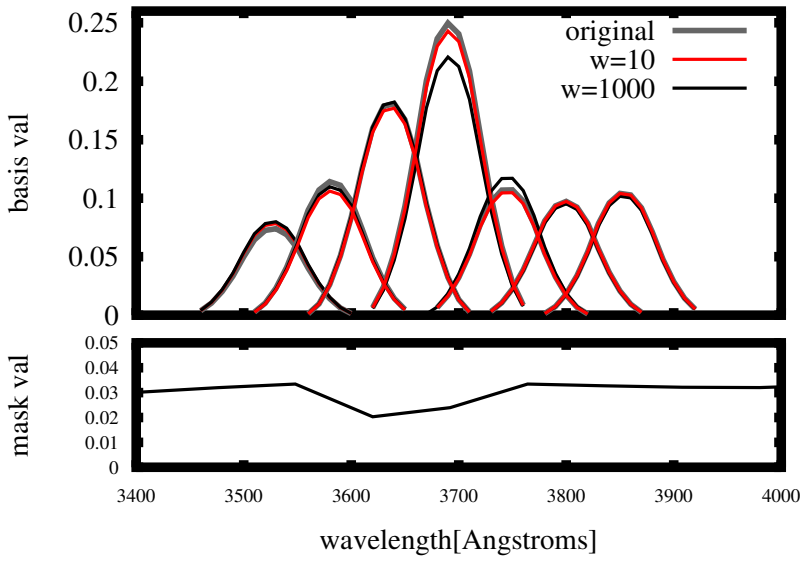

Figure 3.3 The impact of regularization weight components w and $n(p,\lambda)$ on the best-fitting basis splines. The top panel shows best-fit basis functions (phase=-13) for two different dyadic regularization weights: $w = 10$ (red) and $w = 1000$ (black). For comparison, the input model is shown in thick gray. The bottom panel shows the number of spectral fluxes constraining the model as a function of wavelength for this phase value.

3.2.2 SALT-II training process

One of the key strengths of the SALT-II model lies in its comprehensive, self-consistently derived model uncertainties. The sections below explain where and how in the training process each of these is calculated. For reference, a cartoon of the SALT-II training process is shown in Figure 3.4.

Training stage 1: initial error snake calculation

For each set of input light curves, initial values of x_0, x_1 and c are fit via a pair of user-supplied spectral components (i.e. M_0 and M_1). These values serve as starting points for

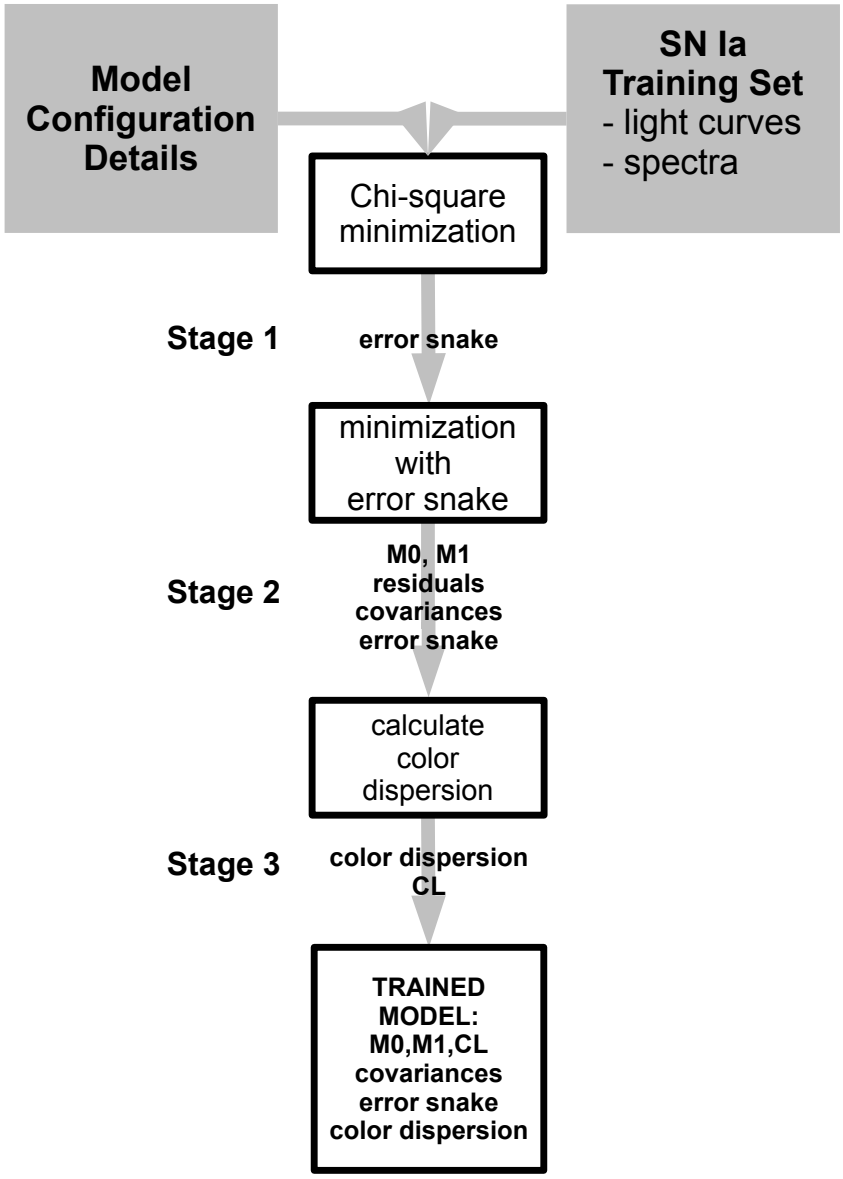

Figure 3.4 The three stages of the SALT-II model training process. Each stage calculates best-fit model parameters using successively improved estimates of model uncertainties.

the optimization of the model M_0, M_1 and CL parameters. By minimizing the chi-squared, the best-fit CL parameters and the best-fit M_0 and M_1 basis parameters are determined.

At the end of Stage 1, a color-independent error scaling factor $S(p,\lambda)$ is determined by requiring light curve training data to have reduced chi-squared values of 1 in any given phase-wavelength bin:

$$\chi^2 \equiv \sum_{i=1}^{m} \sum_{j=1}^{n_i} \left(\frac{(f_{i,j} - f_{\mathbf{M}}(z_i, \mathbf{x_i}, \lambda_j; \mathbf{M}))^2}{(\sigma_{i,j}^D)^2 + (S(p,\lambda) \times \sigma_{i,j}^M)^2} \right) = DOF. \tag{3.4}$$

The default bin size is (6 days) x (1200 Å), but it is increased if there are less than 10 data points in the bin. To ensure the error snake has no color dependence, an overall amplitude adjustment is made to each model light curve M_i for each corresponding data light curve D_i. By including this error scaling factor (hereafter "error snake"), the training accounts for mismatches between the assumed model and the actual underlying SN Ia model.

Stage 2: final M_0, M_1, and errorsnake

Using the components from stage 1 as initial values, the model is refit in stage 2, this time incorporating the error snake uncertainty scaling factors into the chi-squared. The results of this fit are taken to be the final M_0 and M_1 components, and the model covariances and error snake are recalculated.

Stage 3: final color law fitting

Using the model and error snake obtained in stage 2, the input light curves are refit for x_1 and c, and light curve residuals are calculated. The light curve residuals and their uncertainties are used to derive a model of broadband scatter as a function of central filter wavelength by minimizing the log-likelihood function

$$F = R^T W R - log\ det(W) + log\ det(A^T W A). \tag{3.5}$$

Here, R is the vector of light curve residuals, W is the inverse of the residuals covariance matrix, and A is the matrix of model derivatives with respect to all parameters. By using light curve residuals rather than the full training data set we are implicitly assuming that the color dispersion is independent of phase. To simplify the minimization, we also assume that the color dispersion is not correlated with passband and assume that the model derivative matrix A can be written as a function of wavelength $k(\lambda)$:

$$k(\lambda) \equiv k(a_i, \lambda_i; \lambda). \tag{3.6}$$

Therefore, the minimization consists of finding the best fit parameters a_i and λ_i. Incorporating these additional color uncertainties, the color law is refit for a final time.

Ultimately, the trained model consists of the stage 2 M_0 and M_1 components, model covariances, error snake, and the stage 3 color law and color dispersion. When SN light curve data are fit with this model, the model covariances include contributions from the model components M_0 and M_1, the error snake, and the color dipersion.

3.2.3 Training Test Overview

Figure 3.5 gives an overview of the process this work uses to test SALT-II training.

From a SN Ia input model and cosmology, N realizations of SN Ia training sets (light curves and spectra) are generated. These observations (“Training Sets") are used to constrain N new SALT-II models (“Trained Models"). Finally, the trained models are used to fit a single set of SN Ia light curves (“Test Set") generated from the SN Ia input model, resulting in N sets of light curve parameters (x_0, x_1, c_i).

By examining such quantities as training residuals, hubble residuals, and best-fit cosmologies resulting from various training configurations and input training sets we will answer three key questions about SALT-II. We will test the ability of the SALT-II framework to determine the model uncertainty from input data. We will quantify the biases in hubble residuals (and cosmology parameters) due to various choices of regularization. And we will measure biases resulting from mismatches between the underlying model

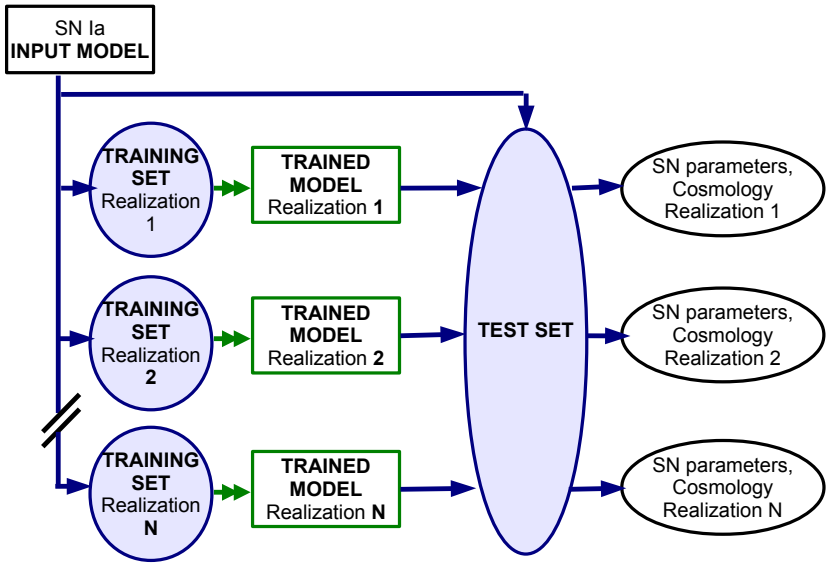

Figure 3.5 Cartoon of training test schematic. From an input SN Ia model and cosmology, N sets of SN Ia training data and a single test set of SN Ia light curves are generated. Each set of training data is used to constrain a new SALT-II model, then each new SALT-II model is used to fit the test set. The resulting sets of light curve parameters are analyzed, yielding N best-fit cosmologies.

and the assumed SALT-II model.

3.3 Simulations

We use the SNANA MC code (Kessler et al. 2009b) to generate realistic SN Ia data for training and testing the SALT-II model. In this section, we describe the data sets after which our simulations are patterned, the techniques we have used to generate simulated light curves and spectra, and the tests we have performed to verify the realism of our

simulations.

3.3.1 The SN Ia Data Samples

To enable comparisons with previous systematics checks of the SALT-II SN Ia model such as those described in G10, as well as recent cosmology results obtained with the SALT-II SN Ia model (Conley et al. 2011) we choose to use simulated SN Ia data patterned after three key data sets: the nearby low-z sample (e.g. Jha et al. 2007), the first-year SDSS-II sample (Holtzman et al. 2008), and the 3-year SNLS3 sample (Conley et al. 2011).

Nearby Low-z

The nearby low-z sample is a heterogeneous data set compiled from an assortment of photoelectric and CCD observations. Its largest components are the Calán/Tololo SN Ia survey (Hamuy et al. 1996) and the first two releases of the CfA monitoring campaign (Riess et al. 1999; Jha et al. 2006). These data cover the redshift range $0.02 - 0.10$ and have been reported in the Landolt system (Landolt 1992). In addition to providing a low-redshift anchor for the Hubble diagram, this data set includes many SNe with more than 10 spectral observations, making it a necessary SALT-II training input.

SDSS-II

The SDSS-II SN survey discovered and spectroscopically confirmed ~ 500 type Ia SNe during its three Fall operating seasons from 2005-2007. All data were acquired on the SDSS 2.5-meter telescope (Gunn et al. 2006) with the SDSS camera (Gunn et al. 1998) and *ugriz* filters (Fukugita et al. 1996; Doi et al. 2010). This set of homogenous observations bridges the gap in redshifts between nearby and high-z SN Ia samples (z $\sim 0.02 - 0.45$), making it interesting for both cosmology and light curve fitter training. Light curves have been released for 146 of these SNe (Holtzman et al. 2008).

SNLS 3-year

The SNLS 3-year data set (Conley et al. 2011) consists of 279 SN Ia discovered and spectroscopially confirmed during the first three years of the SNLS 5-year survey. All data were acquired on the 3.6-meter Canada-France-Hawaii Telescope (CFHT) by the MegaCam imager with $g_M r_M i_M z_M$ filters. These homogeneously observed and reduced light curves cover the redshift range from $\sim 0.2 - 1.0$.

3.3.2 SED-based simulations

The SN Ia simulations used for this work are generated directly from time sequences of spectral energy distributions ("SIMSEDS"). Each spectral energy distribution model consists of a set of fluxes parametrized by phase, wavelength, and two or more model variables. This choice accomplishes two aims. First, it ensures that spectra and light curves for a given simulated SN are consistent. Second, it allows for maximum flexibility in the choice of supernova model parameterizations. SIMSED models based on light curve fitters such as SALT-II may be characterized by light curve observables (i.e. width and color), whereas SIMSED models derived from explosion simulations such as FLASH, Sedona, or Phoenix may be parametrized by more physical quantities (e.g. viewing angle, Ni-56).

Two fiducial SIMSED models are used in this paper. The first model ("GP") has been adapted from the SALT-II surfaces used in G10with the specific goal of SALT-II training compatibility in mind. The second model ("H") is based on the k-correction templates published by Hsiao et al. (2007). Other than the addition of a reasonable width-luminosity relation, no attempt has been made to ensure compatibility with SALT-II. Color variations for each model are based on the color law published in G10. These models are explained in greater detail in §3.4.

Table 3.1. MC x_1 and c Parent Gaussian Distribution Parameters

	mean	σ	gen. range
x_1	0.0	1.0	$-2, +2$
c	0.0	0.1	$-0.3, +0.3$

Note. — The same distributions are used for all training data simulations.

LC Simulation Details

The methods employed by the SNANA MC code to achieve realistic SN light curves have been described in other works (e.g. Kessler et al. 2009a,b). For our SDSS and SNLS light curve simulations we follow the same prescriptions as Kessler et al. (2012) (hereafter K12).

The quality of the simulations for the SDSS-II and SNLS3-Megacam samples is illustrated with several MC/Data comparisons in Figures 3.6 and 3.7.

Most aspects of the MC agree well with the observed data. The largest difference comes in fitted SALT-II color (c) and stretch (x_1) distributions. Although it is well-established that the parent distributions of these parameters are best described by an asymmetric Gaussian (e.g. K12), to simplify training results we've chosen to use symmetric Gaussian distributions. The values for the parent distribution parameters used in this work are given in Table 3.1.

Despite this simplification, our fitted MC mean color and stretch as a function of redshift agree reasonably well with their SDSS and SNLS data counterparts.

SPEC Simulation Details

Through its "SIMLIB" feature (Kessler et al. 2009b), the SNANA MC code is able to produce light curves with realistic signal-to-noise ratios and cadences. We've developed a similar structure to allow the generation of SN spectra with realistic signal-to-noise ratios and cadences. The spectral follow-up information for a survey is stored in a text file called a "SPECLIB", an example of which is shown in Figure 3.8. For SPECLIB SNe with associated observed spectra, each line captures the relevant information of one observed spectrum, including spectrum rest frame epoch, beginning and ending observer frame wavelengths, and spectrum signal-to-noise ratio as a function of observed wavelength. SPECLIB SNe without associated spectra are also included in the library, to ensure that SNe with no spectral follow up are accurately accounted for in the simulation.

When a spectrum MC is begun, the subset of library entries matching the redshift range of the simulation is selected. For each simulated supernova, a library supernova can be chosen at random from this subset, or may be matched by a user-specified function of the parameters z, x_1, and c. A simulated SN spectra is generated for each "MJD" in the library entry. The simulated spectrum observed phase, wavelength range, and S/N are tuned to match the observed spectrum upon which it is based. All valid library entries are used once before any entry may be repeated.

Currently, two spectral libraries exist, a "low-redshift" version (corresponding to the low-z and CfA SN samples used in the G10 SALT-II training), and an SNLS3-Megacam version. New libraries can be easily created to simulate existing or upcoming surveys.

Although the SNLS3 training set only included those spectra judged to have negligible galaxy contamination, we have included galaxy contamination capabilities in our spectral simulator. For each simulated SN a galaxy contamination fraction at M_B peak can be chosen from a parent distribution. A galaxy template is then normalized to the appropriate flux and added to the SN spectra. We focus on contamination from elliptical and normal spiral galaxies, using as templates the sb and elliptical spectra[2] from the Kinney-Calzetti

[2] The template files elliptical_template and sb_template were downloaded from the website

Spectral Atlas of Galaxies (Calzetti et al. 1994; Kinney et al. 1996).

3.4 SN Ia input models

As illustrated in Figure 3.5, all trainings begin with the selection of an appropriate SN Ia input model. For this work three different input models have been used: the SALT-II surfaces published in G10, a specially-designed variant of the SALT-II surfaces published in G10, and a model based on the Hsiao k-correction templates (Hsiao et al. 2007). In this section we will describe the motivation behind the use of each type of model and give a general description of how the models were made.

3.4.1 G10 model

These models are built from the G10 spectral surfaces and the G10 color law, combined as proscribed in Equation (3.1) for a range of x1 and color values. The "S2b" model consists of 1025 separate spectral time series constructed from the G10 surfaces and color law, spanning 25 x_1 values from -3 to 3 and 41 c values from -0.3 to 0.3. Because it contains some negative fluxes, especially at early times in the UV region and late times in the near-IR, this model isn't suitable for our training purposes. However, it makes a good comparison model for Malmquist bias tests.

3.4.2 GP model

A second model "GP" used the Guy10 surfaces as a starting point. To ensure full SALT-II training compatibility, these surfaces were run through a script designed to simultaneously remove negative fluxes and translate them onto the desired training basis. As with the "S2b" model, Equation (3.1) was used to combine the output surfaces with the G10 colorlaw for the same range of x_1 and c values. Since this model is perfectly train-

http://www.stsci.edu/hst/observatory/cdbs/cdbs_kc96.html

able, it is ideal for ensuring that the training process is able to accurately reproduce an input model if given enough input data.

3.4.3 H model

The third type of model we use is based on the Hsiao template (Hsiao et al. 2007). Constructed from a large collection of observed SN Ia spectra, the Hsiao template was designed to represent the mean spectral features of the SN Ia population. As such, it is similar to the G10 M_0 surface, and has no inherent light curve width variation. We have added width variation by applying a stretch function to the flux, such that a supernova with stretch s and peak time t_0 has flux at epoch t and wavelength λ

$$F(t,t_0,s,\lambda) = F(t',t_0,s=1,\lambda), \tag{3.7}$$

where $t' = (t-t_0)/s$. Like the prior two models, the G10 colorlaw was used to add color variation, and the same input range of x_1 and c values was utilized[3].

Since the H model is not an additive model like the SALT-II formalism, it is not clear that the training process will be able to reproduce it. This makes it a reasonable test for the ability of SALT-II to reproduce arbitrary SN Ia models.

3.4.4 Intrinsic scatter models

Fits of SNe Ia typically include an intrinsic scatter term on the order of ~ 0.15, representing the amount of extra uncertainty required to be added in quadrature such that cosmology fits to SN Ia-derived distance moduli obtain reduced chi-squared values of ~ 1. Historically, this extra uncertainty has been associated with the peak B-band magnitude parameter M_B. However, several recent papers have shown evidence suggesting that the SN Ia scatter varies as a function of wavelength, producing not just magnitude scatter but also color scatter (Guy et al. 2010; Foley & Kasen 2011; Chotard et al. 2011; Marriner et al. 2011) and that the assumptions we make about this scatter affect extinction laws

[3]From Guy et al. (2007), $s = 1.00 + 0.091 * x1 + 0.003 * x1^2 - 7.5e^{-4} * x1^3$

and cosmology derived from our SN data sets. The underlying source of this scatter is a subject of ongoing study. A recent work by Kessler et al. (2012) has evaluated models of intrinsic brightness variation. We chose three of these intrinsic scatter models, FUN-COH, G10, and C11_0, to test the effects of different intrinsic scatter forms on SALT-II training.

These models are defined as wavelength-dependent perturbations to the underlying input model. By design, perturbations average to zero so that the underlying SN Ia model is not changed. All models used in this work are independent of redshift and epoch. Combining these smearing models with our base Hand GP models gives us six total input models to choose from.

Coherent scattering: FUN-COH

Coherent magnitude shifts are the simplest form of scatter to add to our base model. For each SN, a shift in flux s is chosen from a gaussian distribution of mean zero and standard deviation equal to the desired scatter ($\sigma_{COH} = 0.13$ for this work). The underlying SN Ia flux is multiplied by 1+s, then spectra and magnitudes are computed as usual. This scattering model produces a coherent shift in magnitudes; as such it only changes the SN Ia parameter M_B and produces no change in color c, and is the most similar to the traditional form of intrinsic scatter.

G10

This model of scatter is based on the wavelength-dependent magnitude dispersion measured from the G10 SNLS3 training set during the SALT-II training process (Fig. 8 of G10). To create a perturbation which can be applied to our SED-based input models, independent scatter values are chosen from the measured dispersion at 800Åwavelength intervals and then joined by a sine interpolation. Because the interpolation slightly reduces the total amount of scatter, the measured G10 magnitude dispersion is increased by an overall factor of $1 + (\lambda_{rest}2157)/9259$. An additional coherent scattering term of

$\sigma_{COH} = 0.09$ has also been included. This scattering model produces an uncorrelated color scatter, as well as a magnitude scatter.

C11_0

Our last scatter model is based on a covariance magnitude scatter matrix from the Chotard et al. (2011) analysis of high quality Nearby Supernova Factory spectra. The original scatter matrix was extended by Kessler et al. (2012) to cover the full wavelength range required by SALT-II training. As with the G10 scatter model, the C11 scatter is determined for broadband wavelengths. To apply it directly to our input models, six random magnitude shifts [U'UBVRI] are drawn from the covariance matrix and then connected with the same sine interpolation used for the G10 model. As with the former model, the magnitude shifts must be scaled up (here by a factor of 1.3) to compensate for the reduction in scatter caused by the interpolation. This scattering model produces a correlated color scatter, in addition to a magnitude scatter.

3.4.5 Input model naming conventions

To be clear about which model is being used to train SALT-II, a compound name will be used to describe the input. For example, an input data set created with the GP base model altered by a G10 color smear will be called GP-G10. Table 3.2 summarizes the various training options used in this work.

3.5 Analysis

In this section we describe the quantities that will be used to evaluate the results of the training tests.

3.5.1 Quantities Derived From Training

To evaluate the success of the training procedure, we begin by examining the training products themselves. The training process and products have been outlined in Figure 3.4 and described in Sec §3.2.

Final M_0 and M_1 components, color laws, and color dispersions will be compared directly with those of the input model.

3.5.2 Quantities Derived From Light Curve Fitting

Other quantities, such as HD bias, can be obtained from the light curve fit results.

Recall that each realization of a particular training test is subsequently used to fit a test set of SNe light curves generated from the same input model (see Figure 3.5). For each test set SN, the best-fitting scale (x_0), stretch (x_1), and color (c) parameters are determined by minimizing a χ^2 based on the difference between the SN photometry and synthetic photometry of the model flux. For each SN, the fitted distance modulus is given by

$$\mu_{fit} = m_B - \mathbf{M_B} + \alpha x_1 - \beta c \tag{3.8}$$

where the effective B-band magnitude m_B is defined as $m_B = -2.5\ log_{10}(x_0) + 10.635$ and the global parameters α, β, and $\mathbf{M_B}$ are determined by a fit of the entire test set using the "`SALT2mu`" program described in Marriner et al. (2011).

For a given training test, it is interesting to compare the mean recovered α and β parameters with their input values. Various quantities may also be constructed from the fitted distance moduli μ_{fit}. These are described in the following subsections.

Hubble scatter

The simplest quantity to calculate from the fitted distance moduli is the Hubble scatter. This quantity is defined as the dispersion on $\Delta\mu$, the difference between the fitted distance modulus and the distance modulus calculated from the best-fit cosmological parameters.

Like K12, we simplify this quantity slightly by computing the dispersion of

$$\Delta\mu \equiv \mu_{fit} - \mu_{calc}(z, \Omega_M, \Omega_\Lambda, w) \tag{3.9}$$

where the fitted distance modulus μ_{fit} comes from (3.8) and the calculated distance modulus μ_{calc} is obtained by assuming a ΛCDM cosmology with $\Omega_M = 0.3$, $\Omega_\Lambda = 0.7$, and $w = -1$.

Hubble bias

For a single test SN i, we begin by calculating the average fitted distance modulus over all training realizations N:

$$< \mu_{fit,i} > \equiv (\sum_{j=1}^{N} \frac{\mu_{i,(fit,j)}}{N}). \tag{3.10}$$

We can then define the Hubble bias $\Delta < \mu_i >$ as the difference between the average fitted distance modulus (3.10) and the actual distance modulus μ_{sim}:

$$\Delta < \mu_i > \equiv < \mu_{fit,i} > - \mu_{sim,i}. \tag{3.11}$$

In figures, this quantity has been binned as a function of redshift and the mean bias has been plotted against the mean redshift in each bin. Therefore, as plotted, the Hubble bias tells us on average how correct a training's measured distance modulus is for a supernova in a particular redshift bin. We expect that an ideal training should have bias measurements consistent with zero in all redshift bins.

Training model scatter

For a single test SN i, we define the training model scatter $\delta\mu_i$ as the dispersion of the fitted distance moduli $\mu_{(fit,i),j}$ (where j runs over training realizations 1 to N) about the mean fitted distance modulus $< \mu_i >$:

$$\delta\mu_i \equiv \sqrt{\sum_{j=1}^{N} \frac{(\mu_{i,(fit,j)} - < \mu_{fit,i} >)^2}{N-1}}. \tag{3.12}$$

This quantity tells us how reproducible an individual SNe's measured distance modulus is from realization to realization for a particular training test. In figures, this quantity has been binned as a function of redshift and the mean model scatter has been plotted against the mean redshift in each bin. Therefore, this plot tells us how stable a training's average distance modulus is for a supernova in a particular redshift bin. In the limit of a perfect training, the model uncertainty should go to zero in all redshift bins.

3.5.3 Best-Fit Cosmologies

Finally, for each training test we can determine the ensemble of best-fit cosmology parameters recovered from the test set.

We'd like to know whether our trained models are able to accurately recover the input cosmology, or whether the training procedures result in a systematic bias. To measure these biases, we fit the simulated Hubble diagram in a manner similar to the *FwCDM* fits described in Kessler et al. (2009a).

To obtain best-fit cosmology parameters, SN distance moduli are combined with Baryon Acoustic Oscillation (BAO) and Cosmic Microwave Background (CMB) constraints.

For the BAO constraint, we use the quantity A defined by Eisenstein et al. (2005),

$$A(z_1; w, \Omega_M, \Omega_{DE}) = \frac{\sqrt{\Omega_M}}{E(z_1)^{1/3}} \times \left[\frac{|\Omega_k|^{1/2}}{z_1} \mathscr{S}_k \left(|\Omega_k|^{1/2} \int_0^{z_1} \frac{dz'}{E(z')} \right) \right]^{2/3}, \quad (3.13)$$

and for the CMB we use the shift parameter R

$$R(z_{CMB}; w, \Omega_M, \Omega_{DE}) = \sqrt{\Omega_M} \int_0^{z_{CMB}} \frac{dz'}{E(z')}. \quad (3.14)$$

Rather than taking the best fit A and R values from data, we calculate them from the SN simulation cosmology parameters ($H = 70, \Omega_M = 0.3, \Omega_{DE} = 0.7, w = -1.0, \Omega_k = 0.0$) and the experimentally determined redshifts $z_1 = 0.35$ and $z_{CMB} = 1090$ (Eisenstein et al.

2005; Komatsu et al. 2009). However, we keep the published uncertainties, yielding the constraints

$$\chi^2_{BAO} = [(A(0.35; w, \Omega_M, \Omega_{DE}) - 0.487)/0.017]^2 \tag{3.15}$$

and

$$\chi^2_{CMB} = [(A(1090; w, \Omega_M, \Omega_{DE}) - 1.750)/0.019]^2 . \tag{3.16}$$

In the absence of input SN data, these constraints yield the best-fit cosmology parameters $\Omega_M = 0.299 \pm 0.052$ and $w = -1.010 \pm 0.3$.

3.6 Redshift-dependent Bias Corrections

Before presenting the results of our training tests, it is worth explicitly detailing one more portion of our data analysis: redshift-dependent bias corrections. Any redshift-dependent bias affecting our data will affect cosmology parameter measurements. As such, we must identify and attempt to remove these biases as best we can.

3.6.1 Overview of "Malmquist Bias" Correction Techniques

To obtain accurate cosmology parameters, flux-limited SN surveys must account for the impact of selection effects on distance modulus measurements. Typically, SN Ia light curves are simulated from parameter distributions (color,stretch,M_B) consistent with the observed data, and selection biases are evaluated from these simulations. Slight variations exist in the ways the simulated light curves are deployed and the biases are evaluated.

Most papers applying a selection bias correction analyze the simulated data in an identical manner to the real data; in other words, the simulated light curves are generated and fit from the chosen SN Ia model, and subjected to any additional processing (i.e. global parameter fitting if using SALT) necessary to obtain distance measurements. The fitted distances are then compared with the underlying distances $\mu(z, \Omega_i, H_0)$ to obtain the recovered distance modulus bias as a function of redshift and the real data is corrected

accordingly. Papers using this method include Astier et al. (2006)[4], Wood-Vasey et al. (2007), and Kessler et al. (2009a).

The SNLS3 cosmology analysis (Sullivan et al. 2011) takes a slightly different tack. As described in a companion paper by Perrett et al. (2010), simulated SNe light curves are generated independently from the SNLS3 fitting models (SALT-II and SIFTO), inserted directly into search images, and run through the discovery pipeline in the same manner as the actual data. The simulations are configured such that each simulated SN Ia's actual Δm_B (including both stretch and intrinsic dispersion variations) is known a priori. For the set of detected SNe Ia, the applied selection bias correction comes from the recovered $\langle \Delta m_B \rangle$ as a function of redshift. The simulated data is never fit.

In all of the papers referenced above, the applied corrections are described as "Malmquist bias" or "selection bias" corrections. However, by including light curve fitting (and global parameter fitting, for SALT-based fits) as part of the process, the first method implicitly corrects for fitting biases as well as selection biases. As such, it is not truly a "Malmquist Bias" correction, and is fitter-dependent as well as survey-dependent. By contrast, the method used for the SNLS3 cosmology results is a true "Malmquist bias" correction.

For our work, we use the first technique ("$TOTAL$") rather than the second, due to limitations imposed by our current spectral simulation technique. In order to generate a SN Ia model training sample with consistent light curves and spectra, the intrinsic scatter model must be applied to the spectrum as a whole, rather than to the individual broad-band magnitudes as is done by Sullivan et al. (2011). Therefore, we know the pre-intrinsic scatter simulated m_B and the recovered (post-lightcurve fit) $m_{B,fit}$, but not the actual m_B.

3.6.2 Individual Components of Redshift-dependent Bias

It is interesting to try to decompose the total bias into consituent parts: selection bias ("$MALM$"), model bias ("MOD") , and width and color correction ("WCC") bias. Al-

[4]Ultimately the authors deemed the recovered selection bias insignificant compared with other sources of uncertainty, and chose not to apply the correction.

though we cannot do this in a fit-independent way, we approximate the Perrett et al. (2010) technique by simulating a realistic full SN Ia sample (i.e. no efficiency cuts are applied), fitting it with minimum selection cuts, and comparing the distance moduli thus derived to either the simulated distance moduli or the distance moduli from a "detected" sub-sample (i.e. those passing our efficiency cuts). Within this framework, we define the following biases:

$$MOD = < m_{B,i} - M_B^{fit} + \alpha^{sim} x_{1,i} - \beta^{sim} c_i - \mu_i^{sim} >_{FULL}, \tag{3.17}$$

$$WCC = < (\alpha^{fit} - \alpha^{sim}) x_{1,i} - (\beta^{fit} - \beta^{sim}) c_i >_{FULL}, \tag{3.18}$$

and

$$MALM = < \mu_i^{fit} >_{DETECTED} - < \mu_i^{fit} >_{FULL} . \tag{3.19}$$

Here, $m_{B,i}$, $x_{1,i}$, and c_i are individual SN Ia parameters derived from model fits of the data; M_B^{fit}, α^{fit}, and β^{fit} are global model parameters obtained from a SALT2mu fit of the individual SN Ia parameters; and α^{sim} and β^{sim} are the global model parameters used to simulate the light curve data. All averages are over redshift.

In terms of these same variables the $TOTAL$ bias we apply prior to cosmology fits is:

$$TOTAL = < m_{B,i} - M_B^{fit} + \alpha^{fit} x_{1,i} - \beta^{fit} c_i - \mu_i^{sim} >_{DETECTED} \tag{3.20}$$

Here again the average is over redshift. We emphasize that the $TOTAL$ bias corrects for all three components – $MALM$, WCC, and MOD – simultaneously.

Because these biases are derived from fitted quantities, their values as a function of redshift are fit model and survey specific. Because these biases depend on simulations, they also depend on the input model used to simulate the SNe. Plots of the individual biases for each set of realistic models will be shown and discussed in Section §3.10.

3.6.3 Details of our Bias Correction Method

We perform our *TOTAL* redshift-dependent bias corrections as follows. The test data are fit with the SN Ia model to obtain values of α, β, and parameter distributions for x_1 and c. Using the observed parameter distribution[5] and the fitted values of α and β, the trained SN Ia model is used to generate and fit a large simulated SN Ia data set ($N \sim 10,000$), yielding distance modulus measurements for each of the simulated SN. To be clear, this simulation includes intrinsic scatter of the G10 form, with the node values described in K12replaced by the trained model broadband dispersion (i.e. Figure 4.3). Finally, the average difference in distance modulus $\langle \Delta\mu(z) \rangle \equiv \langle \mu_i^{sim}(z) - \mu_i^{fit}(z) \rangle$ is calculated as a function of redshift and used to correct the observed distance moduli such that $\mu(z)_i^{corr} = \mu(z)_i^{fit} + \langle \Delta\mu(z) \rangle$. The uncertainty of $\langle \Delta\mu(z) \rangle$ is assumed to be the rms of the $\mu_i^{sim}(z) - \mu_i^{fit}(z)$ values used to calculate it, and is added in quadrature to obtain $\delta\mu(z)_i^{corr}$.

MALM bias corrections are performed similarly. The main differences are 1) the simulation is performed with no efficiency cuts at all, 2) the light-curve fits use very minimal light-curve quality cuts, and 3) the bias corrections are calculated according to Equation(3.19). Changes 1) and 2) enable us to obtain a "FULL" data set. Once this data has been fit, efficency cuts may be applied to extract the subset of "DETECTED" SNe.

3.7 Test Case 1: Ideal Training

We are working under the hypothesis that given enough input data, the SALT-II training process will produce a reasonable copy of the input model, and that light curve fits made with such a model will allow us to recover input cosmology to high accuracy. For the purposes of this work, we define an "Ideal" training as one in which a comprehensive, high-quality data set is used as input. In this section, we will describe the data set used

[5]The fitted parameter distributions themselves must be corrected for selection bias. Examples of this correction can be found in Kessler et al. (2009a) and D'Agostini (1995). However, we approximate this correction by using the parameter distribution fitted from an ideal test set.

Table 3.2. Main Training Options

input model	color smear	training set	test set
H	none	ideal	ideal
GP	COH	real	REAL
	C11		
	G10		

Note. — Main training options used in this work. Particular training tests will be identified by a concatenation of options. For instance, a training test based on the Hinput model with a C11 color smear trained with an ideal training set and tested on a realistic test set would be called H-C11-ideal-REAL.

for these trainings, and the results of our training tests for both the GP-NONE-IDEAL and H-NONE-IDEAL input models (definitions of the various training model options are given in Table 3.2).

3.7.1 Training Set Composition

Our ideal training set consists of 200 simulated SNe drawn from a flat redshift distribution spanning z of 0.01 to 0.4. Half of these supernovae have photometry in the SDSS *ugriz* system, the other half have photometry in the Landolt *UBVRI* system. The photometry is of very high quality, with two-day cadence (observer frame) and signal-to-noise ratios of 2000 at peak *B*-band (or *g*-band) regardless of redshift. Spectrometry is of similarly high quality. Seven spectra are generated for each supernova, with the first observation date randomly chosen between rest frame epochs -14 and -4, and the remaining spectra spaced every 10 (rest frame) days thereafter. This selection mechanism results in a flat spectrum

distribution with phase for the entire sample. All spectra span rest frame wavelengths 2000 to 9200 Å, and have signal-to-noise ratios of 1000 defined on a bin size of 100 Å.

3.7.2 Training Configuration

Given the high-quality, high-cadence input data, the training configuration is adjusted accordingly. The flux scale uncertainty parameter is set to 0, such that observer-frame U/u data is not deweighted during the training. Because our training set spectra have no calibration errors, we effectively turn off photometry-based spectral rescaling by increasing the calibration wavelength step from 800 Å to 100,000 Å. Finally, the high sampling of the input data makes regularization irrelevant.

3.7.3 Test Set Composition

Once training is complete, the new "IDEAL" models are tested by using them to fit large, similarly high-quality data sets. These data sets (which we also call "IDEAL") are made up of 4000 SDSS and 4000 SNLS SNe. The relevant spectroscopic selection efficiencies have been applied to the data set, but the exposure times of the simulations have been adjusted to give photometric data with signal-to-noise ratios of 1000 in the B-band at peak. The SDSS fits use all available *ugri* photometric data, the SNLS fits use all available *griz* photometric data. The fitted light curve parameters are then used to determine the global best-fit M_B, α and β values and best-fit cosmology parameters Ω_M and w for each training realization, as described earlier in §3.5.2 and §3.5.3.

3.7.4 Ideal Training Results

Model Residuals

Because we have tailor-made our fiducial GP SN Ia model to match SALT-II training capabilities (see §3.4.2), synchronized our simulation software with our training software, and trained with extensive, high signal-to-noise ratio training sets, we expect that the

resulting GP-NONE-IDEAL trained models will match the input model to better than one percent in flux in all bands. No effort was made to match the H model to SALT-II, so we don't expect H-NONE-IDEAL trained models to reach the same level of agreement.

Plots of surface residuals bear out these expectations. Figure 3.9 shows the mean integrated flux residuals and mean color law residuals for the GP ideal training test.

The GP mean flux residuals are smaller than 0.5% in flux in all bands except U (which agrees to 1.0% in flux), indicating excellent agreement between the input and trained model surfaces. Color law residuals show similarly small differences. As shown in Figure 3.10, the average H-trained model has similarly small integrated flux residuals near peak but larger residuals at early and late times. We attribute this difference to the inability of the SALT-II formalism to exactly reproduce the H stretch model. H color law residuals are very similar to their GP counterparts, topping out at 0.005 at the edges of the wavelength range.

Cosmology Residuals

Each of the 10 trained models was used to fit a single ideal set of 8000 test SNe light curves. `SALT2mu` was applied to the resulting light curve parameters to obtain 10 sets of best-fit model values M, α and β, and 10 sets of distance moduli to use for cosmology fits. Assuming a flat λCDM cosmology, a chi-squared minimization was used to determine the most likely cosmology parameters w and Ω_M for each realization. The mean recovered values of α, β, and w are shown in Table 3.3.

Both trainings recovered mean α values quite a bit smaller than the input value of 0.10: 0.094 was recovered for the GP model (a 6% discrepancy) and 0.090 for the H model (a 12% discrepancy). A discrepancy in α is somewhat expected for the Hmodel, since the stretch function used to create the SED width-magnitude relation cannot be described with the SALT-II linear combination of surfaces. On the other hand, the two training tests were able to recover β and w correctly, as expected. With our ideal test

Table 3.3. Recovered Fit and Cosmology Parameters - IDEAL TRAININGS

model	α	β	w(raw)	w	σ_{int}	$\tilde{\chi}^2$
NZ*	0.094 ± 0.002	3.201 ± 0.007	-1.005 ± 0.005	-1.000 ± 0.005	0.000	0.080
HRK*	0.090 ± 0.002	3.202 ± 0.009	-0.998 ± 0.005	-1.003 ± 0.005	0.000	0.163

*Trainings are of the type <model>-NONE-IDEAL-IDEAL

Note. — Mean cosmology parameters recovered by ideally trained models on ideal data sets. The training sets were created with input parameters $\alpha = 0.100$(GP), $\alpha = 0.102$(H), $\beta = 3.2$, and w$= -1.0$. For each training, we have shown both the original w and the Malmquist-bias corrected w. Our Malmquist bias correction technique is described in section §3.6. All errors are errors in the mean.

set, Malmquist bias is minimal: both the fitted w and the Malmquist-bias corrected w are recovered within the 1-sigma limit of 0.005.[6]

Figure 3.11 shows the Hubble bias as a function of redshift for the H and GP trainings. The average fitted distance modulus $\langle \mu(z)_{fit} \rangle$ differs from the actual distance modulus $\mu(z)_{sim}$ by less than 0.003 magnitudes in all redshift bins. As with the training surface residuals, the GP input model gives better results than the H input model. However, in either case, the redshift-dependent bias is tiny (0.002 magnitudes). data are sparse.

3.7.5 Ideal Training Test Conclusions

With the exception of slightly low recovered α values, ideal training tests give the outcomes we expected: training the SALT-II model with a complete, well-sampled, high quality set of data allows us to recover the input model with good accuracy. For both models, the mean SED broadband-integrated flux is recovered to better than 2 percent in all bands for phases between -10 and +10 days of B-band maximum. At late times, the

[6]As of Feb 6, 2013, the MBCORR w values have been performed with the "ideal" Malmquist bias correction. I'm in the process of rerunning these using the "traditional" method, and will update the paper when I'm finished. The difference between the two corrections is described in Section §3.6.3.

maximum flux difference seen for the H model is 3 percent, and for the GP model, only 0.5 percent.

When applied to an ideal set of training data, mean hubble residuals as a function of redshift are less than 0.003 magnitudes at all redshifts, and the cosmology parameter w is recovered with high accuracy. After applying Malmquist bias corrections, the less-easily trainable H mean w differs by 0.003 ± 0.005; the GP mean w is -1.000 ± 0.005.

From this ideal training test, we conclude that the training process can indeed recover the correct model, given enough input information. In the next sections, we explore the effects of training changes. Section §3.8 explores the impact of regularization on realistically trained models. In Section §3.9, we determine the average Hubble bias for realistically trained models, and explore the effects of different color smearing models .

3.8 Regularization

As described in Section §3.2, "regularization" refers to the addition of extra terms to the χ^2, with the goal of reducing the amount of high-frequency ringing trained into regions of the best-fit model where input data is sparse. Ringing in the best-fit model adds extra scatter to light-curve fits, thereby reducing the precision with which distances and cosmology parameters can be measured. On the other hand, the addition of regularization terms can systematically bias the best-fit model. Therefore, uncertainties due to regularization must be measured and accounted for in the distance modulus error budget.

The forms of regularization used in this work are described in section §3.2.1. The overall strength of each term is determined by a weight chosen at the time of training. G10 evaluated the change in mean distance modulus as a function of redshift for two different choices of normalization. They found the change to be small, less than or equal to 0.005 magnitudes for redshifts below 1.

Using our simulation techniques we seek to confirm these findings. We will also explore whether one type of regularization does better than another at minimizing bias

and statistical error.

3.8.1 Description of our tests

GP-NONE-REAL trainings have been run for three sets of regularization weights: "nominal", "high" (10x larger than nominal) and "low" (10x smaller than nominal). Here the nominal regularization weight is 10 for the gradient term and 1000 for the dyadic term. The same regularization terms and weights are applied to both M_0 and M_1. Nominal weights are equivalent to those used in the G10 training.

To determine the optimal regularization, we compare average Hubble biases and Hubble scatter (see §3.5.2) for the three trainings. Results of these comparisons are shown in Figure 3.12.

For the low and nominal regularizations, Hubble bias $\Delta < \mu >$ is equivalent to within 0.005 magnitudes at redshifts between 0.2 and 1.0. This finding is consistent with the regularization tests described in Guy10. High regularization results in greater changes in Hubble bias, approaching 0.015 magnitudes at redshifts of 0.3 and 0.8. Hubble scatter is smallest when the nominal regularization is used. The low and high regularization weights worsen scatter by 0.02 magnitudes.

These tests suggest that the nominal regularization is the best training choice. It doesn't add any extra distance bias compared to low regularization weights, and does a better job of reducing Hubble scatter. It should be noted that these results have been calculated with simulated values of alpha and beta (0.11 and 3.2 respectively), rather than with the `SALT2mu` fitted values (which change from realization to realization). However, using the fitted values does not substantially alter the test results.

3.9 Test Case 2: Realistic Training

Having established that the training procedure is able to reproduce the input model under ideal conditions (i.e. full phase-space coverage by the training set, no intrinsic scatter),

and having established the optimal level of regularization, we proceed to test SALT-II training with more realistic training data.

Eight types of realistic trainings have been performed: GP-NONE-REAL, GP-COH-REAL, GP-G10-REAL, GP-C11-REAL, H-NONE-REAL, H-COH-REAL, H-G10-REAL, and H-C11-REAL. Model naming conventions are described in Table 3.2.

As with the ideal training test, we examine training results in terms of trained model residuals, light curve fitting results, and cosmology results. With more realistic input training data, we expect the differences between H and GP models to be greatly reduced: the added uncertainties will obscure the real but small differences between the linear and stretch-based models. As far as intrinsic scatter is concerned, we expect the NONE scatter models to be quite similar to the COH models, with the main difference lying in scatter about the mean (COH should have larger scatter than NONE). On the other hand, we expect the G10 and C11 scatter models to differ from each other, as well as to differ substantially from both the COH and NONE models, due to the relative "trainability" of the G10 intrinsic scatter model compared to the C11 intrinsic scatter model. The three K12 scatter models used in this work have been summarized in §3.4.4.

The following subsections will briefly describe the training set compositions, the training configuration, and the test set make-up used in our realistic trains, followed by a presentation of the realistic training test results.

3.9.1 Training Set Composition

Our realistic training sets consist of 220 SNe designed to mimic the data qualities of the low-z sample and the SNLS3 sample. Details of the light curve and spectral simulations have been given in sections §3.3.2 and §3.3.2.

3.9.2 Training Configuration

Training is similar to that used in the G10 paper. We use nominal regularization (see section §3.8.1), and a spectral recalibration step size of 800Å corresponding to the typical width of a broadband filter. Unlike trainings with real data, we keep our flux scale uncertainty parameter set to 0, such that observer-frame U/u data is not deweighted.

3.9.3 Test Set Composition

As with the ideal training tests, we evaluate our trained models by using them to fit large test sets of SN Ia light curve data drawn from the same input models and parameter distributions as the training sets. We continue to use an "Ideal" data set (as described in §3.7.3), and add to these fits and analyses of "Realistic" data sets. "Realistic" data sets include not only realistic spectroscopic selection efficiencies, but also realistic photostatistics.

3.9.4 Realistic Training Results

Analogous to our presentation of the ideal training tests, we start by examining residuals of the trained surfaces and color laws with respect to the input models. We compare the obtained statistical and systematic uncertainties (particularly model scatter $\delta\mu$, §3.5.2) with the estimates made in G10. Finally, we examine how well trained-model fits are able to recover input cosmology parameters, and determine the recovered distance modulus biases as a function of redshift.

In general, all eight trainings recover the M_0 surface reasonably well. Figures 3.13 and 3.14 show light curve residuals ($x_1 = 0$) as a function of phase for realistic GP and H trainings, respectively.

More variation about the mean U residual is seen for trainings with C11 scatter than G10 scatter. Early phases ($p < -5$) show sinusoidal structure in the mean residual for all combinations of input model, though in the H versions the pattern is confined to the U

and B wavelengths whereas in the GP versions it extends to V. For the H models the mean U residuals increase after $p \sim 15$ from zero to a maximum of two and a half percent for the G10 scatter version, and to four percent for the C11 scatter model. The same trend is not observed for the GP models. This being said, with the exception of the earliest epoch of the GP-G10 training in the U, all residuals are consistent with zero.

Color law residuals, defined as the difference between the new CL and the input CL, are a different story. As seen in Figure 3.15, the coherent scatter trainings return color laws in good agreement with the input model. However, the other scatter models show deviations from the input at wavelengths below 3500 Å and, for the C11 scatter in particular, above 7000 Å. Overall, the shapes of the color law residuals are similar for the two C11 trainings, regardless of which base model is used: at the smallest wavelengths, the new color laws have 15-25% more extinction than the input color laws. However, the GP-G10-REAL color law residual looks similar to the GP-C11-REAL color law residual, whereas the H-G10-REAL color law residual is quite different in shape from the H-C11-REAL color law residual; of the four trainings shown in Figure 3.15, H-G10-REAL is the only one with less extinction in the bluest wavelengths than the input model.

Finally, we can compare the recovered broad-band color dispersions with the input models. Figure 4.3 shows the input and recovered output dispersions as a function of wavelength for the two realistic intrinsic scatter models G10 and C11. The input broad-band dispersion is recovered reasonably well for the C11 scatter models. The recovered G10 scatter models are quite different in the near UV, both GP and H versions obtaining dispersions at least 25% lower than input with 4-σ significance.

Bias and Cosmology Residuals

Fits of realistically trained models on realistic test data yield the mean recovered values of α, β, and w shown in Table 3.4. To enable comparisons with the results in K12, we have also included results for G10 fits of light curve data simulated with the G10 model and either the G10 or C11 color smear (these are labeled “G10-G10” and “G10-C11”

Table 3.4. Recovered Fit and Cosmology Parameters - REAL-REAL TRAINS

model	α	β	w(raw)	w(TOTAL)	w(MALM)	σ_{int}	$\tilde{\chi}^2$
NZ-G10	0.084 ± 0.013	2.912 ± 0.089	-0.991 ± 0.004	-1.007 ± 0.004	-1.008 ± 0.004	0.124	0.979
HRK-G10	0.091 ± 0.011	2.832 ± 0.089	-0.984 ± 0.004	-1.007 ± 0.004	-0.999 ± 0.005	0.119	0.973
NZ-C11	0.102 ± 0.018	2.647 ± 0.110	-1.004 ± 0.005	-1.024 ± 0.005	-1.023 ± 0.005	0.124	0.966
HRK-C11	0.103 ± 0.020	2.680 ± 0.093	-0.996 ± 0.005	-1.012 ± 0.005	-1.012 ± 0.005	0.126	0.974
G10-G10*	0.112	3.036	-0.985 ± 0.020	-1.000 ± 0.020	-0.995 ± 0.020	0.104	0.984
G10-C11*	0.116	2.737	-0.986 ± 0.020	-1.015 ± 0.020	-0.982 ± 0.020	0.114	0.966

*These tests do not include retraining. Lightcurves are made from the G10 model with G10 or C11 dispersion and fit with the G10 model.

Note. — Mean cosmology parameters recovered by realistically trained models on realistic data sets. All errors are errors in the mean. Input model parameters are α=0.1, β=3.2. A discussion of the α values we expect to recover is given in Appendix A.

respectively).

As described in Appendix A, we expect some mixing between x_1 and c parameters during training. This is especially true for models to which intrinsic scatter has been applied. Expected values of α are listed in Table A.1. After taking this effect into account, our recovered α parameters agree reasonably well with expectations.

None of the test sets recover the input value of β. Because our realistic test data suffers from selection effects, some decrease in β is to be expected. However, our β values vary with input scatter model. The trainings with G10 color smears have an average β of ~ 2.9, whereas the trainings with C11 color smears have average $\beta \sim 2.7$ K12 also reported scatter model-dependent differences in recovered β. Our Table 3.4 results are most similar to the G10 and C11_0 results of the "Nearby + SDSS-II + SNLS3" sample shown in K12 Table 6: they observe a ~ 0.4 difference between the G10 and C11_0 β values. Although our difference is smaller (closer to ~ 0.2), the trend is in the same direction. The offsets between the β values in K12 Table 6 and our corresponding G10-G10 and G10-C11 β values are due to the different distributions of x_1 and c used for our simulations.

Table 3.5. HD bias - LOWZ Sample

redshift	N	GP-G10	GP-C11	H-G10	H-C11
0.007	571	-0.005(0.005)	-0.016(0.004)	-0.002(0.005)	-0.010(0.004)
0.016	343	-0.000(0.006)	0.000(0.006)	-0.002(0.005)	0.005(0.006)
0.024	234	0.012(0.008)	-0.005(0.007)	0.009(0.007)	0.002(0.007)
0.033	133	-0.001(0.010)	-0.015(0.010)	-0.007(0.009)	-0.006(0.010)
0.042	47	0.027(0.020)	0.026(0.020)	0.018(0.018)	0.032(0.020)
0.050	70	0.008(0.014)	0.006(0.016)	-0.006(0.016)	0.013(0.017)
0.054	9	0.031(0.033)	-0.018(0.041)	-0.014(0.031)	-0.016(0.044)
0.067	29	-0.017(0.025)	0.008(0.031)	-0.023(0.021)	0.019(0.032)
0.077	33	0.018(0.023)	-0.020(0.033)	-0.009(0.027)	-0.009(0.033)
0.088	12	-0.045(0.033)	0.029(0.036)	-0.015(0.048)	0.036(0.041)

Note. — HD biases have been corrected for selection effects with TOTAL method. All training tests are REAL-REAL.

Also shown in Table 3.4 are our recovered "raw" and bias-corrected values of the dark energy equation of state parameter w. We show results for two kinds of bias corrections: the "TOTAL" correction used by K12 (Equation (3.20)) and the "MALM" bias correction (Equation (3.19)) most similar to what is done by SNLS3. After corrections, the two G10 scatter model trainings recover a value of w within 2-σ of the input value. The two C11 scatter model trainings give biased w results: the H-C11-REAL w_{corr} is -1.012(significance of 2.4σ) and the GP-C11-REAL w_{corr} is -1.024(significance of 4.8σ). The type of bias correction used has no significant effect on the results.

Mean distance bias $\langle \Delta\mu \rangle$ as a function of redshift for each of the four training configurations is shown in Figure 3.17. Both the raw and corrected biases are displayed. The mean distance modulus bias is listed as a function of redshift and scatter model in Tables 3.5, 3.6, and 3.7.

Table 3.6. HD bias - SDSS Sample

redshift	N	GP-G10	GP-C11	H-G10	H-C11
0.048	47	0.000(0.015)	-0.012(0.016)	-0.024(0.016)	-0.009(0.016)
0.088	131	-0.020(0.010)	-0.015(0.007)	-0.008(0.009)	-0.010(0.008)
0.129	277	-0.010(0.007)	-0.006(0.006)	0.006(0.006)	-0.009(0.007)
0.171	537	0.003(0.005)	-0.001(0.005)	0.004(0.005)	-0.003(0.005)
0.214	763	0.007(0.005)	0.004(0.005)	0.005(0.004)	0.005(0.005)
0.254	790	-0.005(0.005)	-0.002(0.005)	-0.006(0.005)	0.003(0.005)
0.296	495	0.001(0.008)	-0.003(0.008)	-0.006(0.007)	-0.008(0.008)
0.340	315	0.016(0.011)	0.021(0.011)	0.007(0.010)	0.018(0.011)
0.384	225	-0.006(0.014)	-0.009(0.015)	-0.007(0.015)	-0.005(0.015)
0.425	105	-0.049(0.022)	-0.034(0.024)	0.018(0.021)	-0.031(0.024)

Note. — HD biases have been corrected for selection effects with TOTAL method. All training tests are REAL-REAL.

Table 3.7. HD bias - SNLS Sample

redshift	N	GP-G10	GP-C11	H-G10	H-C11
0.263	123	0.008(0.010)	-0.008(0.009)	0.002(0.010)	-0.005(0.009)
0.338	197	0.001(0.008)	0.007(0.008)	0.017(0.007)	0.006(0.008)
0.414	293	0.008(0.007)	-0.001(0.008)	0.011(0.006)	-0.001(0.008)
0.491	354	0.005(0.006)	0.027(0.008)	0.011(0.006)	0.018(0.008)
0.569	472	0.002(0.007)	0.012(0.007)	0.002(0.006)	0.002(0.007)
0.645	508	0.012(0.007)	0.009(0.008)	0.019(0.007)	0.012(0.008)
0.720	570	0.016(0.008)	0.027(0.008)	0.021(0.008)	0.019(0.009)
0.799	557	-0.015(0.011)	-0.001(0.009)	0.001(0.011)	-0.006(0.010)
0.874	457	-0.002(0.013)	-0.013(0.013)	-0.006(0.012)	-0.000(0.012)
0.949	297	0.022(0.015)	-0.060(0.018)	-0.029(0.014)	0.003(0.016)

Note. — HD biases have been corrected for selection effects with TOTAL method. All training tests are REAL-REAL.

3.10 Discussion

In the following subsections, we will discuss some of the implications of these biases, examine procedures for bias correction, and remark on implications for optical SN Ia cosmology and future model training.

3.10.1 Training with intrinsic scatter biases color laws

Adding realistic intrinsic scatter to the SALT2 training set yields biased models. Although the M_0 surfaces do not appear to be impacted (i.e. Figures 3.13 and 3.14), all four realistic scatter color laws show at least a 1-sigma bias at wavelengths bluer than approximately 3000 Angstroms (Figure 3.15). In addition, the two G10 scatter trains significantly underestimate broadband dispersion at wavelengths bluer than 3000 Angstroms (Figure 4.3).

Figure 3.18 shows the difference between the recovered and the input color law for the four realistic-intrinsic-scatter models. The difference between the G10 color law and the CCM (R_v = 3.1) color law is shown on the same panel as a reference. The observed color law biases from our training tests are small and constrained to the region below 3000 Angstroms. However, three of the four input models give biases in the same direction, such that $A_{\lambda,new} - A_{\lambda,old}$ is positive. This trend agrees with Maguire et al. (2012), who found that the SALT-II color law overcorrected SN Ia spectra in the NUV.

In terms of our ability to recover cosmological parameters, the size of this effect is not large. As shown in Table 3.4, the best-fit equation of state parameter w is underestimated by as much as 0.025, depending on the choice of input scatter model.

3.10.2 Implications of a Biased Color Law

NUV biases in the color law and color dispersion affect the ability of the model to correctly fit for the color parameter c in redshift regimes where rest-frame near-UV and U are important. As discussed by K09 and G10, these sorts of biases will result in redshift-

dependent values of β even if the underlying SN Ia β is constant. This effect can be seen in our test samples.

We have divided our test samples into redshift bins of width=0.1 and fit each group individually for β. The resulting values of $\beta(z)$ are shown in Figure 3.19. Included in this figure are results from our ideal and realistic test sets, as well as the $\beta(z)$ values observed by G10 from SNLS3 data. Training tests with no added intrinsic scatter show minimal(no) change in β when applied to ideal(realistic) test samples. When intrinsic scatter is added, both ideal and realistic training tests have identical $\delta\beta/\delta z$ until a redshift of 0.65 when Malmquist bias causes the realistic test sample $\delta\beta/\delta z$ to decrease more rapidly. The mean $\beta(z)$ obtained from our simulated samples is in good agreement with G10 SNLS3 results (see Figure 17, Guy et al. (2010)).

Because the recovered value of β is so sensitive to small biases in the color law and broadband dispersion, it is not productive to interpret this value as a physical quantity.

3.10.3 Impact of scatter models on SALT-II training and HD biases

A similar examination of HD biases as a function of scatter model was undertaken by K12. However, they did not retrain the SALT-II model as part of their work. Comparing our scatter tests with theirs[7], we make the following observations. First, despite our differences in simulated sample x_1 and c distributions, we are able to reproduce their results. Our "NOTRAIN" results (Table 3.4) find that the G10 scatter w is recovered with no bias, whereas the C11 scatter w has a post-correction bias of -0.015 compared to their -0.017. Second, even after retraining, we both find an overall bias in recovered w of ~ 0.02.

[7]The most apt comparisons are the G10 and C11_0 scatter models from the Nearby + SDSS-II + SNLS3 set of data, K12 Table 6

We find that when the full training procedure is used, the strong G10/C11 demarcation observed by K12 decreases. For instance, K12 found G10 w values to be unbiased regardless of the application of a bias correction, whereas C11_0 w values changed significantly and remained biased even after correction. On the other hand, we find that bias corrections change the raw w by about the same amount (0.02) for both G10 and C11, and that the average difference in w between the two scatter models is only ~ 0.01, a 2-σ improvement from K12. On the other hand, we find that bias corrections make the C11 w bias worse whereas they tend to improve the G10 w bias. We emphasize – as did K12– that these results are specific to the combination of surveys used in the tests, and may not apply to analyses with other data.

3.10.4 Statistical Uncertainty Estimates for SALT-II Model Training

Using multiple training set realizations, we have been able to directly measure the scatter in SN Ia distance measurements as a function of redshift due to training statistics. In Figure 3.20, we compare our results with estimates calculated by G10. Becuase our distance scatter measurements include both wavelength dispersion uncertainty and training statistical uncertainty, we've combined the analogous components of the G10 estimates (e.g. the "statistical uncertainty of the training" and "residual scatter model" portions of G10 Figure 16). We find that the scatter in distance measurements ranges from 0.03 to 0.09 at z=1, with the GP-G10 model having the lowest scatter and the H-C11 model having the most scatter, and that the G10 estimates agree well with our results for all intrinsic scatter models.

3.10.5 Using these results to improve constraints on Dark Energy

We have used a series of MC samples to train the SALT-II model and measure HD biases as a function of redshift. Our MC samples were specifically designed to match the SNLS3 SN Ia cosmology sample (e.g. Conley et al. 2011). Because our HD bias measurements

incorporate uncertainties due to SN Ia model, intrinsic scatter, regularization, global parameter values (e.g. β), and bias corrections in a self-consistent way, they may be used to update those portions of the systematic error estimates from the most recent SNLS3 cosmology analysis (Sullivan et al. 2011). In keeping with the treatment described in Conley et al. (2011) we use the bias results from Tables 3.5-3.7 to make covariance matrices for each of the data sets represented in our simulations. The improvements in cosmology constraints solely due to this work are shown in the contour plot in Figure 3.21. The model uncertainties calculated using our technique show that the systematics associated with the SALT-II model are negligible.

3.11 Conclusions

We have used simulated SN Ia samples to determine that SALT-II model training, fits, and bias correction of the current SNLS3 cosmology sample introduces a redshift-dependent HD bias, ultimately resulting in a ~ 0.02 bias on w, significantly smaller than the corresponding systematic bias reported by Sullivan et al. (2011). In order to perform these tests, we have upgraded the SN analysis software package `SNANA` to enable spectrum simulations incorporating realistic photo-statistics, galaxy contamination, and intrinsic scatter.

When the SALT-II model is trained on a SN Ia spectral time series with no intrinsic scatter and a high-quality MC training set, we find that we are able to recover the input model components M_O, M_1, and CL, and obtain a HD with no biases. When the training set is made more realistic via the addition of intrinsic scatter to the input model and a reduction in the training set size and signal-to-noise ratios, our results agree well with the w bias estimates of K12, the $\partial\beta/\partial z$ measurements of G10, and the statistical uncertainty estimates of G10. Because our results agree well with expectations, we conclude that our method is robust.

We identify biases in the UV portion of the trained SALT-II color law and wavelength-

dependent dispersion as the sources of the HD bias. These biases alter the measurement of individual SN Ia color parameters c as a function of redshift, and cause the recovered color correction parameter β to be systematically underestimated. The extent to which the recovered β deviates from the input β depends on the form of the intrinsic color scatter which is applied. Scatter of a form trainable by SALT-II (i.e. G10) results in smaller β biases than scatter with covariances (i.e. C11) which the SALT-II formalism is currently unequipped to handle. Because the color correction parameter β is so sensitive to scatter model, it is unproductive to interpret this value as a physical quantity.

Although the scatter models we use in this work have been thoroughly tested (K12) and found to reproduce key photometric observables such as photo-z residuals, Hubble scatter, and color dispersion, they are solely dependent on wavelength, and as such are somewhat unrealistic. Real SN Ia scatter probably results from a combination of effects, including metallicity, viewing angle, and progenitor. As such, scatter probably depends on phase, stretch, color, and redshift as well. An improved understanding of the origins and nature of intrinsic scatter will be important to reducing systematic uncertainties in SN Ia distance measurements.

The HD biases measured in this work will be used to reduce model-related systematic uncertainties in an upcoming SNLS3 publication (Betoule et al. in preparation). Although our HD bias measurements are model and survey specific, our procedure is general and may be adapted to test any SN Ia model and data sample.

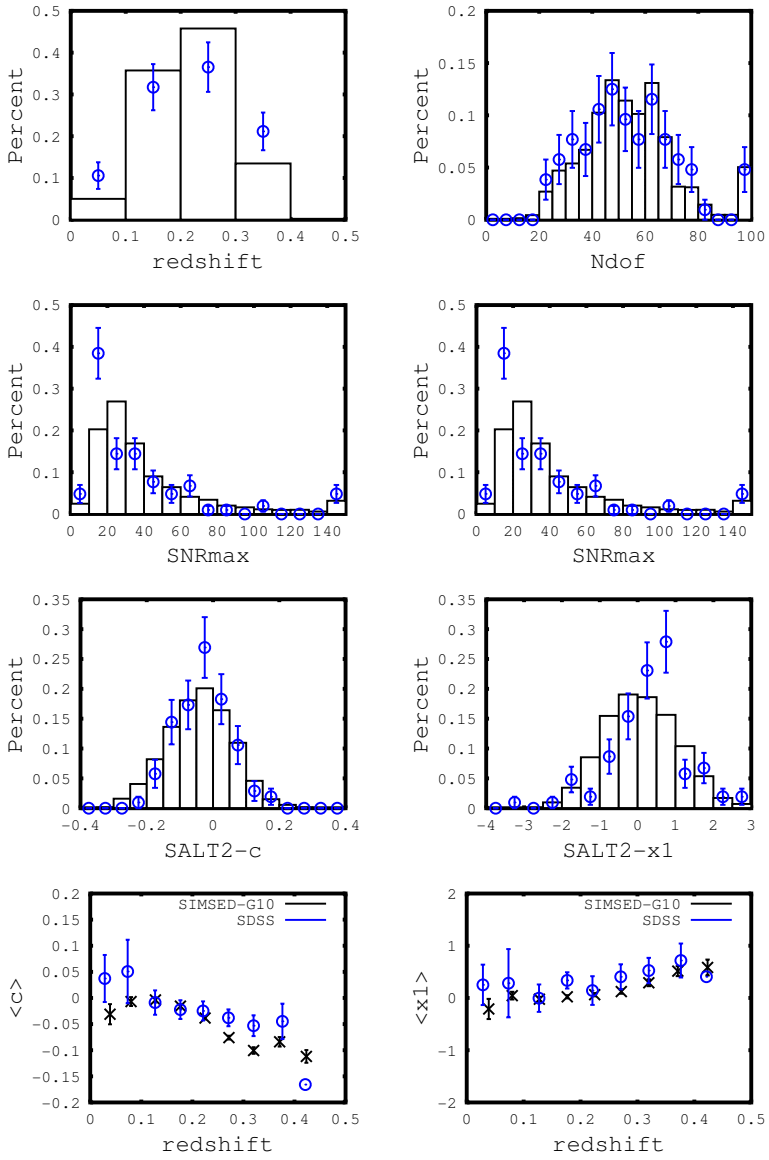

Figure 3.6 Comparison of DATA SET distribution for SDSS-II data (blue circles) and SIMSED MC (black histograms/stars). From top-to-bottom and left-to-right, the distributions are redshift, number of degrees of freedom in the SALT-II light curve fit, maximum fitted S/N, maximum fitted S/N, fitted SALT-II color (c), and stretch parameter (x_1). The bottom two panels show the mean fitted SALT-II color (c) and shape parameter (x_1) versus redshift.

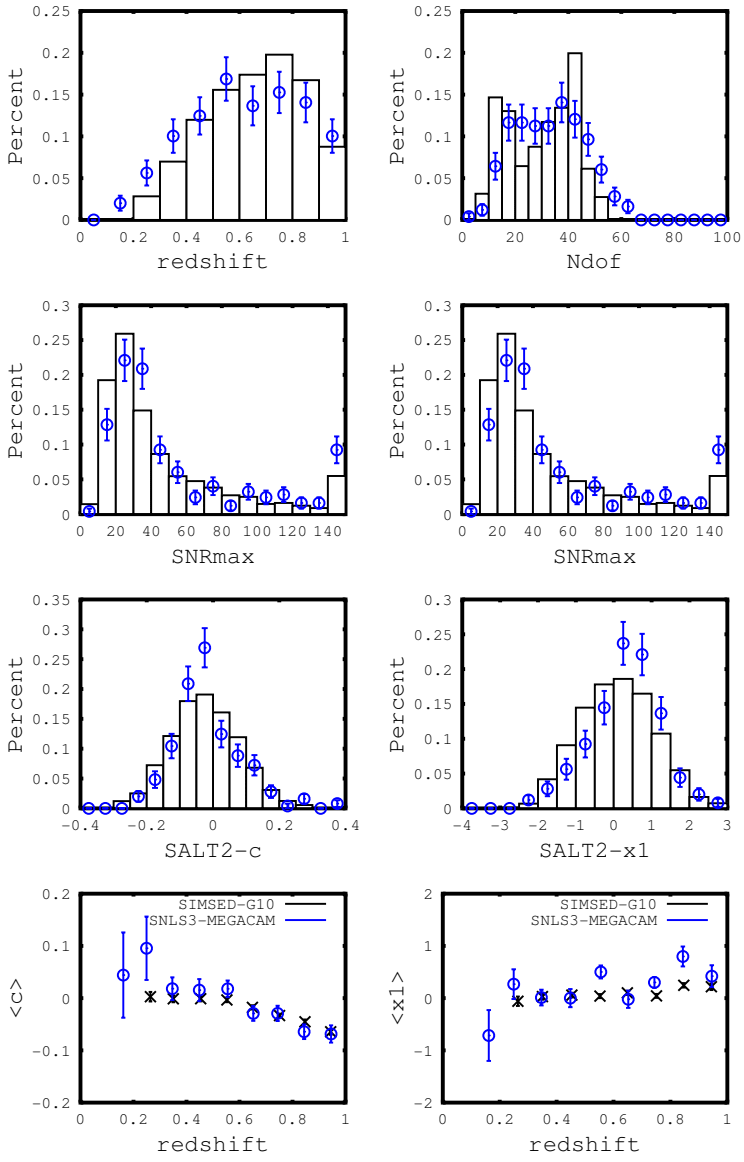

Figure 3.7 Same as Fig 3.6, except for SNLS3-Megacam sample.

```
LIBID: 1 (03D1au)
Z_HELIO: 0.5043                PEAK_MJD: 52909.839  0.308
G10c: -0.015  0.031         G10x1: 1.342  0.218
NSPEC: 1

       MJD    IDTEL  FIRSTWAVE  LASTWAVE  BINWAVE  SNRNBIN  SNR2000  SNR3000  SNR4000  SNR5000 <...> SNR10000
S: 52905.000  30     3739.25    8953.21          5.00     10       -9.00    -9.00    4.13     10.90          -9.00
END_LIBID: 1

#--------------------------------------------------
LIBID: 2 (03D1aw)
Z_HELIO: 0.5820                PEAK_MJD: 52902.946   0.409
G10c: -0.019  0.038        G10x1: 1.342  0.218
NSPEC: 1

       MJD    IDTEL  FIRSTWAVE  LASTWAVE  BINWAVE  SNRNBIN  SNR2000  SNR3000  SNR4000  SNR5000 <...> SNR10000
S: 52905.000  30     3740.71    8961.70          5.00     10       -9.00    -9.00    0.46     7.29           -9.00
END_LIBID: 2

#--------------------------------------------------
LIBID: 3 (03D1ax)
Z_HELIO: 0.4960                PEAK_MJD: 52915.961   0.140
G10c: -0.111  0.032        G10x1: -0.564  0.132
NSPEC: 0

END_LIBID: 3

#--------------------------------------------------
LIBID: 4 (03D1co)
Z_HELIO: 0.6790                PEAK_MJD: 52954.548   0.430
G10c: -0.048  0.065        G10x1: 0.875  0.467
NSPEC: 3

       MJD    IDTEL  FIRSTWAVE  LASTWAVE  BINWAVE  SNRNBIN  SNR2000  SNR3000  SNR4000  SNR5000 <...> SNR10000
S: 52947.000  34     5203.19    9323.19   5.00     10       -9.00    -9.00    -9.00    -9.00          -9.00
S: 52947.000  31     4254.63    8939.63   5.00     10       -9.00    -9.00    -9.00     1.15          -9.00
S: 52965.000  30     3755.00    8950.00   5.00     10       -9.00    -9.00     0.01     1.19          -9.00
END_LIBID: 4

etc...
```

Figure 3.8 Excerpt from a SPECLIB for the SNLS3 SN survey.

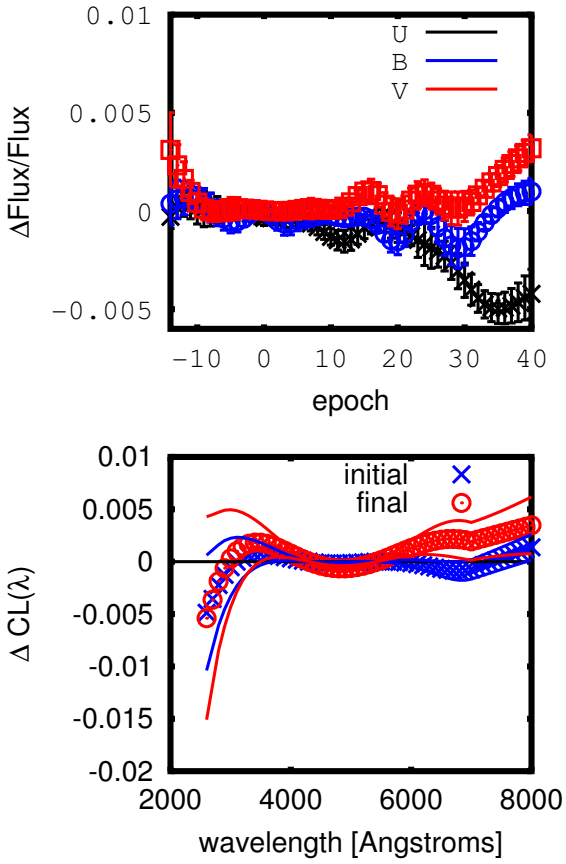

Figure 3.9 Mean flux and color law residuals from the GP ideal training test. The top panel shows the flux residuals for U(black), B(blue), and V(red). The bottom panel shows the color law residuals (C=1). Blue crosses represent the difference between output and input CL after the first stage of training, and red triangles show the same quantity for the final CL. RMS scatters for each set of data are given by corresponding solid lines.

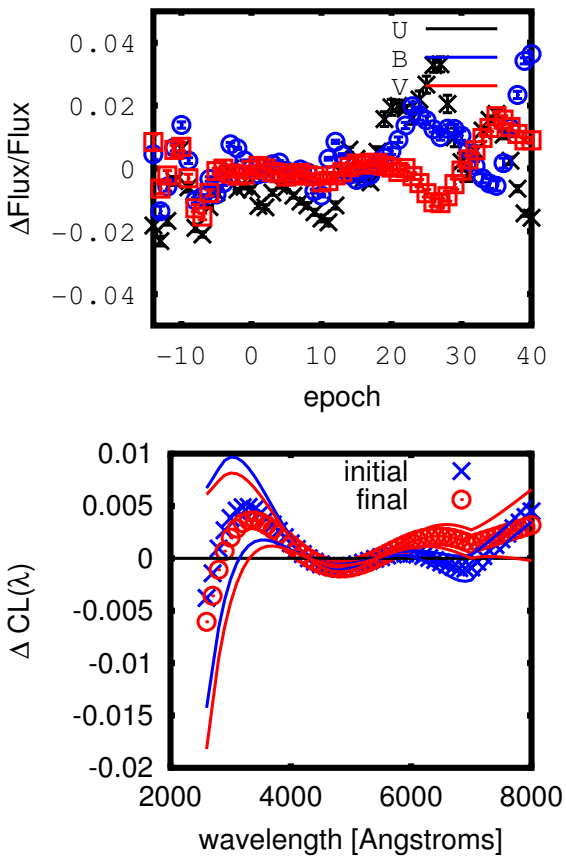

Figure 3.10 Mean flux and color law residuals from the H ideal training test. Plot descriptions are identical to Figure 3.9.

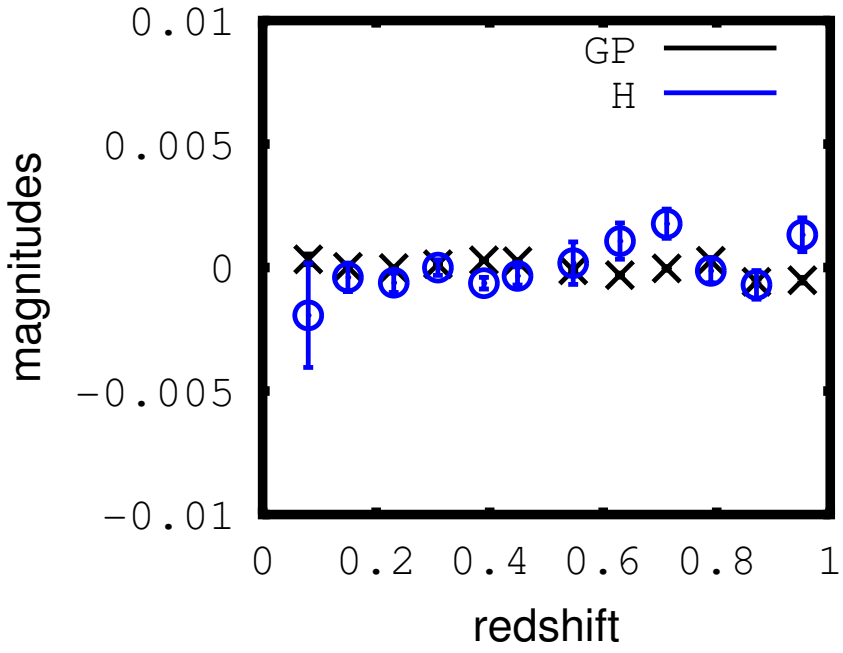

Figure 3.11 Hubble residual bias for the GP and H ideal trainings evaluated with ideal data sets. Both sets of trainings show small bias with minimal redshift dependency.

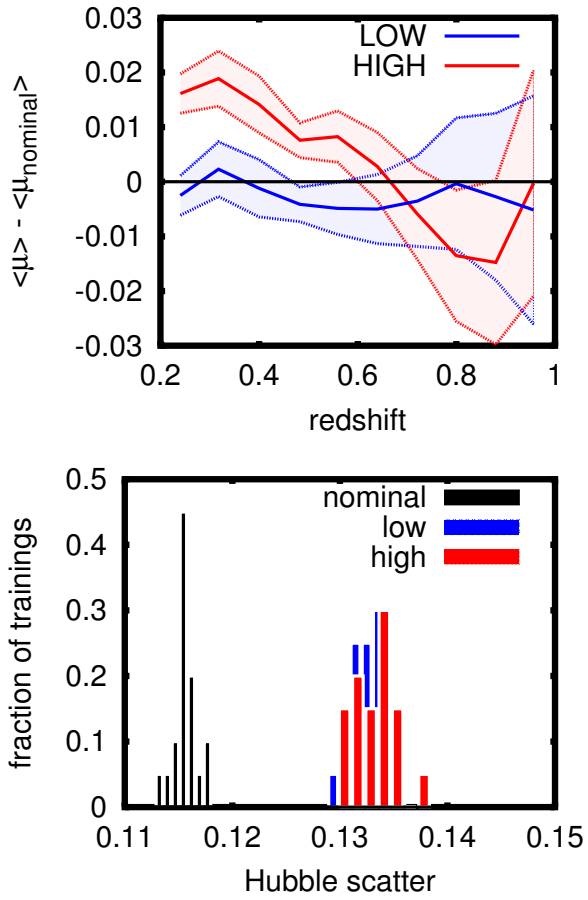

Figure 3.12 Hubble bias and Hubble scatter (§3.5.2) as a function of regularization weight. Distance modulus μ and Hubble scatter have been calculated with simulated values of α and β. Results shown are for GP-NONE-REAL trainings tested with realistic SN Ia data. Model naming conventions are described in Table 3.2. *Top:* Systematic uncertainty of the average distance modulus μ (in redshift bins of 0.1) due to regularization. The low (blue) and high (red) lines compare $10\times$ less and $10\times$ more regularization with nominal regularization. Shaded regions indicate one sigma uncertainties. *Bottom:* Hubble scatter distributions for GP-NONE-REAL trainings with differing levels of regularization: nominal (red), $10\times$ smaller (blue) and $10\times$ larger (red). Twenty realizations were run for each training. The resulting distributions have been normalized to 1.

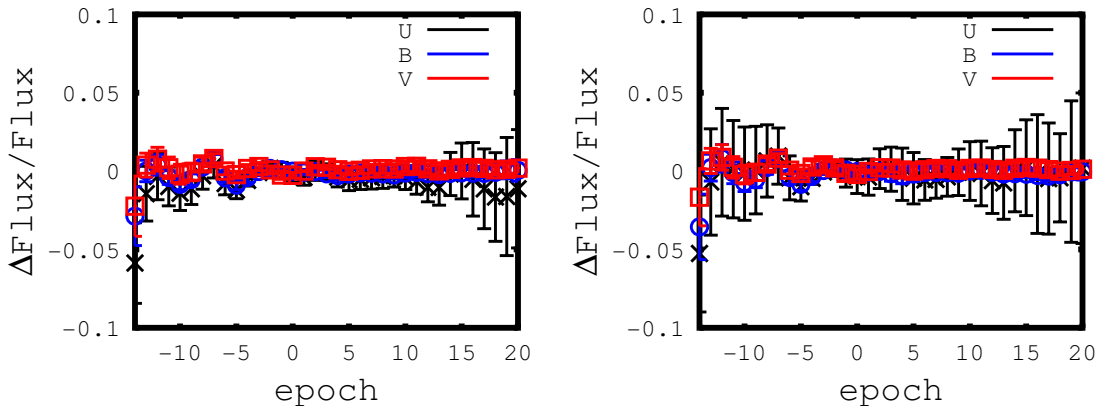

Figure 3.13 Mean M_0 surface residuals from the GP-G10-REAL(left) and GP-C11-REAL(right) training tests. Model naming conventions are described in Table 3.2.

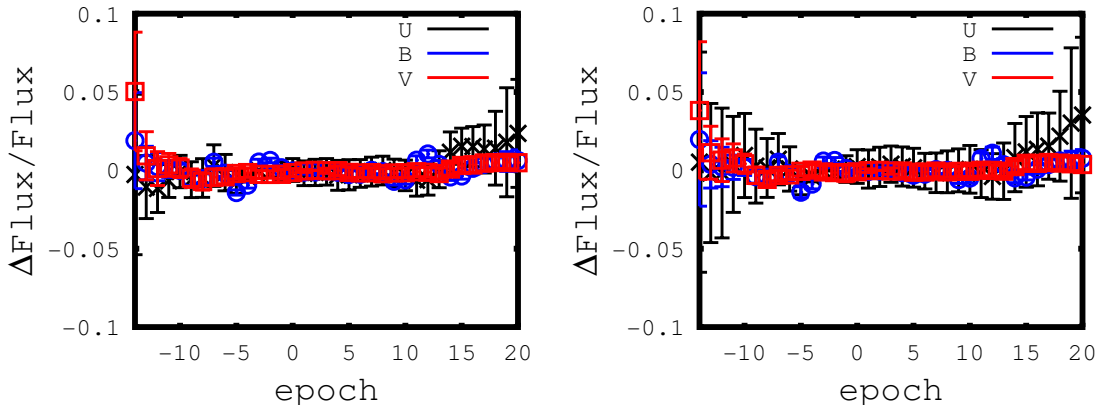

Figure 3.14 Mean M_0 surface residuals from the H-G10-REAL(left) and H-C11-REAL(right) training tests. Model naming conventions are described in Table 3.2.

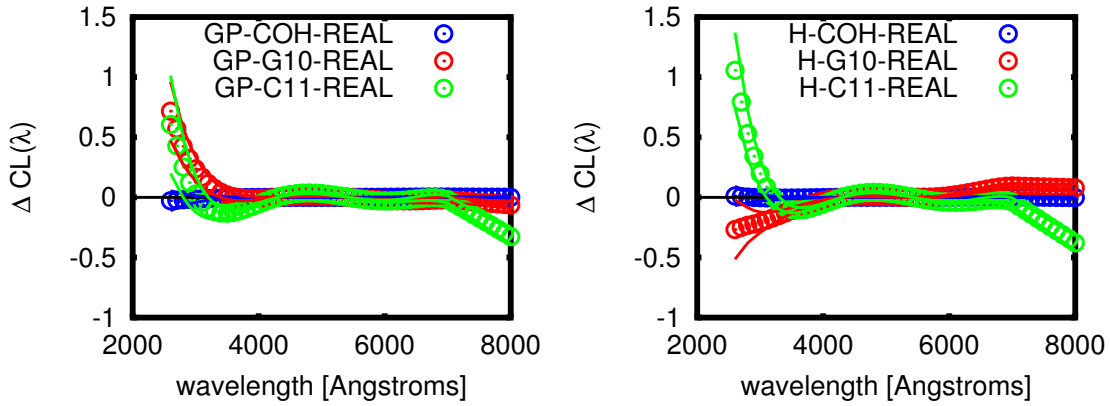

Figure 3.15 Mean color law residuals from the GP(left) and H(right) realistic training tests, for C=1.0. (Notice that this is 10 times the C used in G10 Figure 6). Solid lines show the 1-σ scatter about the mean residuals. Model naming conventions are described in Table 3.2.

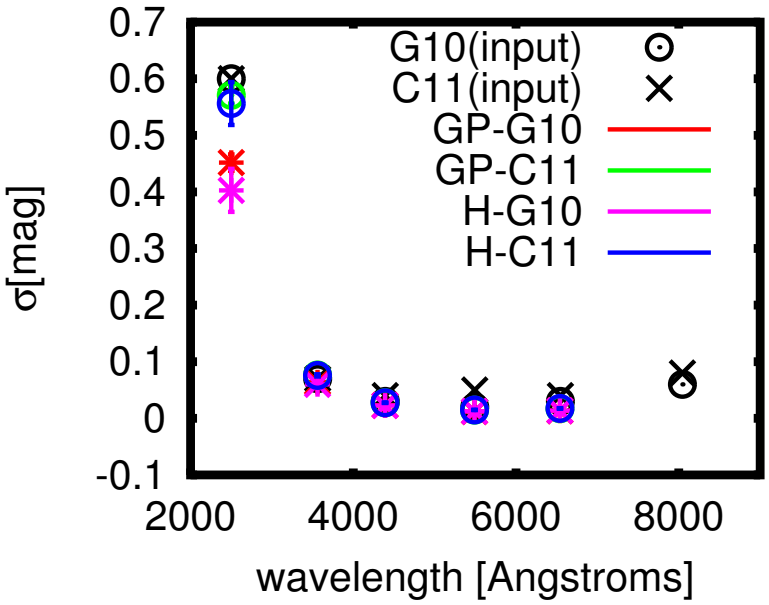

Figure 3.16 Input (black) and mean recovered broadband dispersions from the GP-G10(red), GP-C11(green), H-G10(pink), and H-C11(blue) realistic training tests. Only the diagonal term of the input C11 dispersion is shown. Model naming conventions are described in Table 3.2.

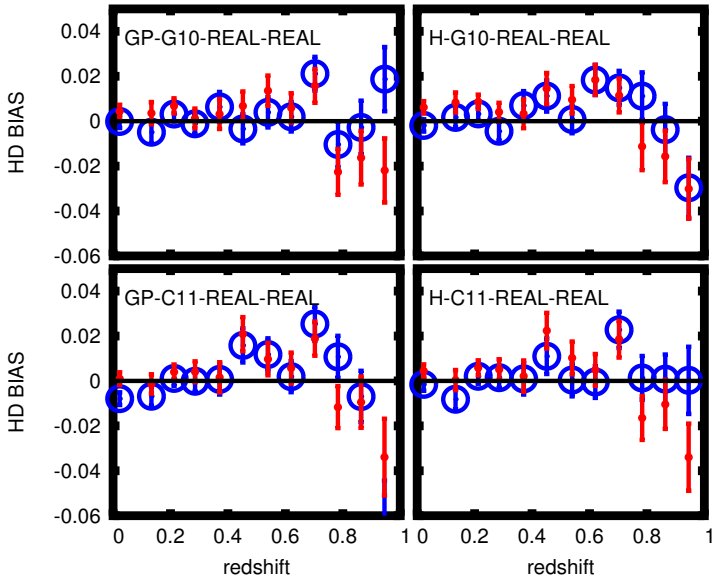

Figure 3.17 Hubble bias is shown for realistically trained models applied to realistic test data. The blue circles show the *TOTAL* (R13) bias-corrected values; small red dots indicate the raw (uncorrected) values. Plot labels indicate the input model and training type. Model naming conventions are described in Table 3.2.

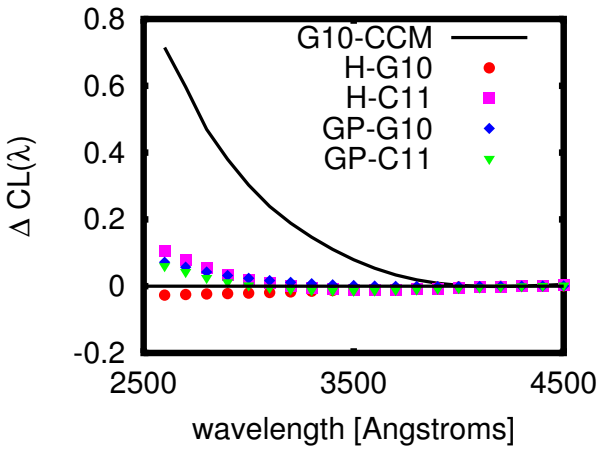

Figure 3.18 Mean color law differences for the four realistic-scatter trainings. Each set of data points shows output $-$ input CL as a function of wavelength for a SN with $c = 0.1$. The solid black line shows the difference between the G10 color law and the CCM ($R_v = 3.1$) color law for comparison. Model naming conventions are described in Table 3.2.

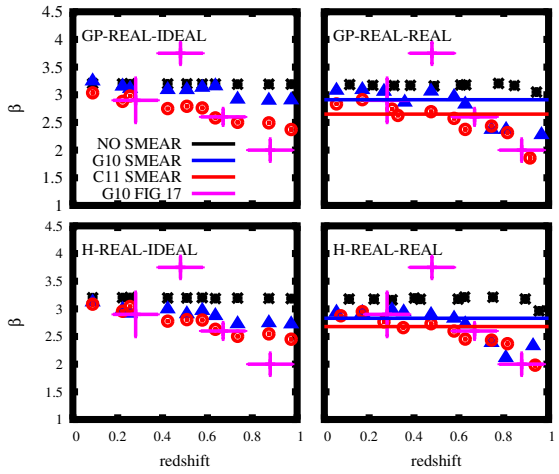

Figure 3.19 Mean β values evaluated independently in redshift bins for the intrinsic scatter models "NONE" (black stars), "G10" (blue triangles), and "C11" (red circles). β values for ideal test sets are shown on the left, β values for realistic test sets are shown on the right. Analogous β values obtained from SNLS3 data (G10 Figure 17) are shown in pink crosses. Solid lines on the right panels show the β values recovered if one assumes β is constant with redshift. Model naming conventions are described in Table 3.2.

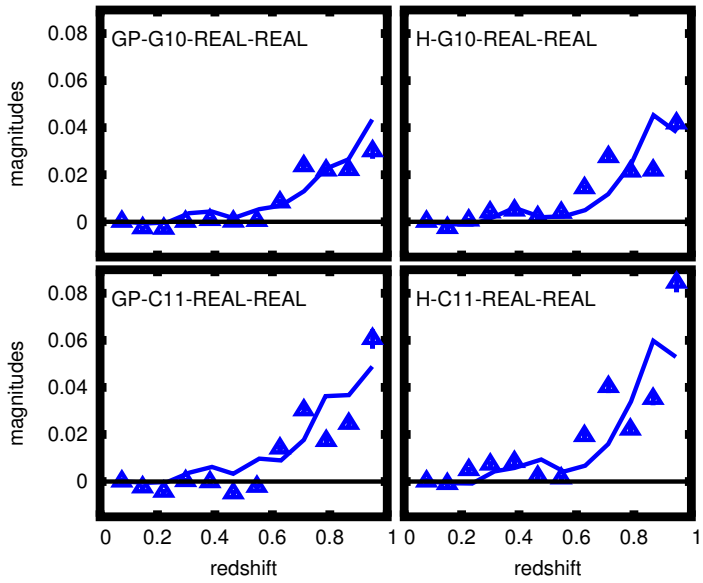

Figure 3.20 Training model scatter as a function of redshift. Solid lines show the mean SALT-II scatter estimates produced during the model training process; triangular points show scatter recovered from our training tests. Both quantities have been normalized by subtracting off their value at $z = 0$. Plot labels indicate the input model and training type. Model naming conventions are described in Table 3.2.

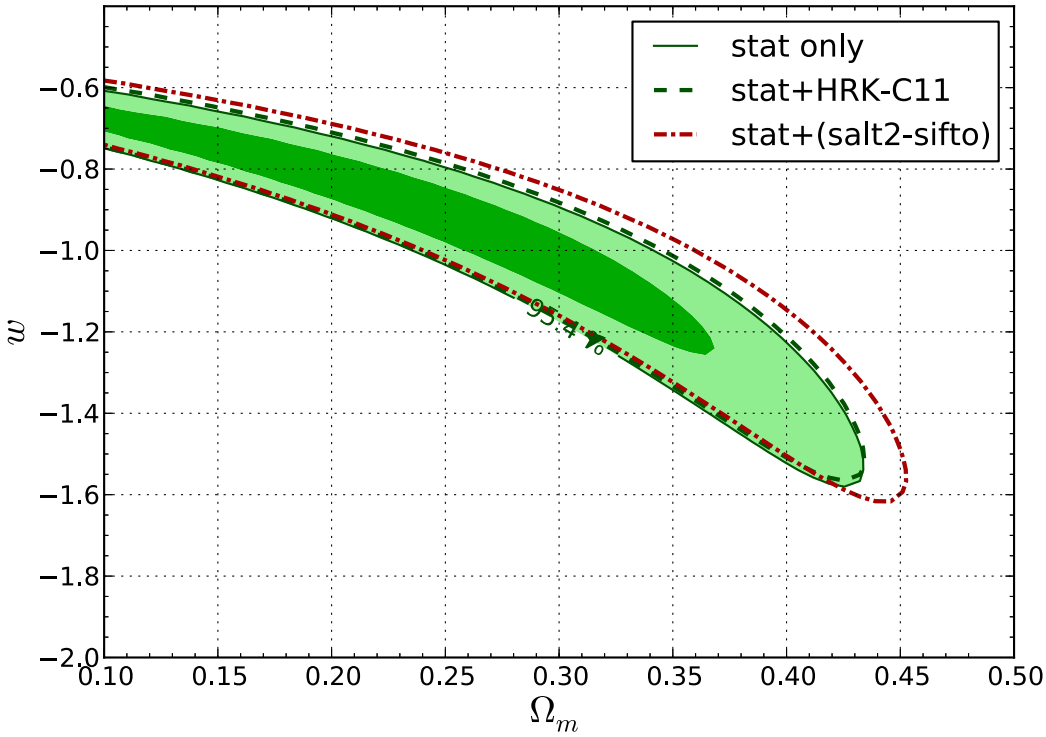

Figure 3.21 Influence of model systematic uncertainties on SN Ia cosmology constraints. The shaded green contours show the SN Ia cosmology constraints on the values of w and Ω_M if only statistical distance uncertainties are included. The dotted lines show the constraints when the model systematics from Conley et al. (2011)(red) or the H-C11 model systematics from this work(green) are taken into account. Model naming conventions are described in Table 3.2.

Chapter 4

Conclusions

4.1 Implications of Current Work

Currently, optical SN Ia cosmology is hampered by a lack of information about SN Ia UV and the systematic uncertainties associated with this wavelength region. Both SN Ia broad-band photometry and spectra show increased dispersion in the UV. Circumstantial evidence suggests that the observed dispersion in the UV region is related to progenitor metallicity. Theoretical studies of the relationship between progenitor metallicity and SN Ia luminosities indicate that metallicity evolution of progenitors could lead to redshift-dependent shifts in average absolute magnitude and width-luminosity relations which potentially bias optical SN Ia-derived cosmological parameters. A relationship between SN Ia UV colors and metallicity is less well studied, in large part because the observational data hasn't been available, but is likely to exist (Walker et al. 2012; Foley & Kirshner 2013). Because the SN Ia color correction parameter is large (~ 3), biases in measured SN Ia color are likely to lead to biases in measured distance.

Using simulated SN Ia training and test samples, we have shown that current training sets and model configurations lead to biases in the SALT-II SN Ia model UV color law and wavelength-dependent dispersion. Our inability to correctly estimate UV color laws and

dispersion leads to confusion about the nature of host galaxy dust and large uncertainties in high-z SN Ia cosmology.

To immediately reduce statistical uncertainties in high-z optical SN Ia cosmology, combining existing optical light curves with one or more space-based NIR observations is very helpful. Thanks to improved CCD efficiencies in the NIR ($\lambda \in [8000, 10000]$ Å) the Dark Energy SN Survey will have the best z photometry of any SN Survey to date. Even so, at redshifts near 1.0, DES optical photometry is only sampling rest frame SN photometry through *lambda* $\sim$ 4000 Å. As shown in Figure 4.2, the addition of *HST* WFC3/IR F105W and F125W photometry adds SN Ia rest frame coverage through $\lambda \sim 6000$ Å. This range of the SN Ia SED has been intensively studied and has much lower dispersion compared to the UV (e.g. Figure 1.5).

Figure 4.3 shows simulation-based estimates of DES distance constraints for SN Ia at redshifts between $z \sim 0.8$ and $z \sim 1.3$ for two situations: DES photometry alone, and DES photometry combined with a single epoch of HST WFC3/IR F105W and F125W photometry 21 days past SN discovery (roughly corresponding to 10 days after rest frame peak *B* magnitude). According to simulations, the addition of that single epoch decreases the distance measurement uncertainty by 0.07, entirely due to a reduction in the model uncertainty on the measured color parameter.

Measurements of the difference in distance bias as a function of redshift for DES alone vs DES + *HST* may also be carried out as an extension of my SALT-II training work.

In order to use optical SN Ia cosmology to learn more about the time evolution of w, understanding the SN Ia UV region is increasingly important. The correlation between host galaxy masses and Hubble residuals indicates that the existing observational parameters – light curve shape and color – are insufficient to standardize the brightnesses of SNe Ia. However, host galaxy mass is only a proxy for the actual SN Ia variable. Circumstantial evidence points to SN Ia progenitor metallicity as a good candidate for a third standardization parameter. Theoretical studies suggest that SN Ia luminosity varies as a function of progenitor metallicity. However, these same studies indicate that the

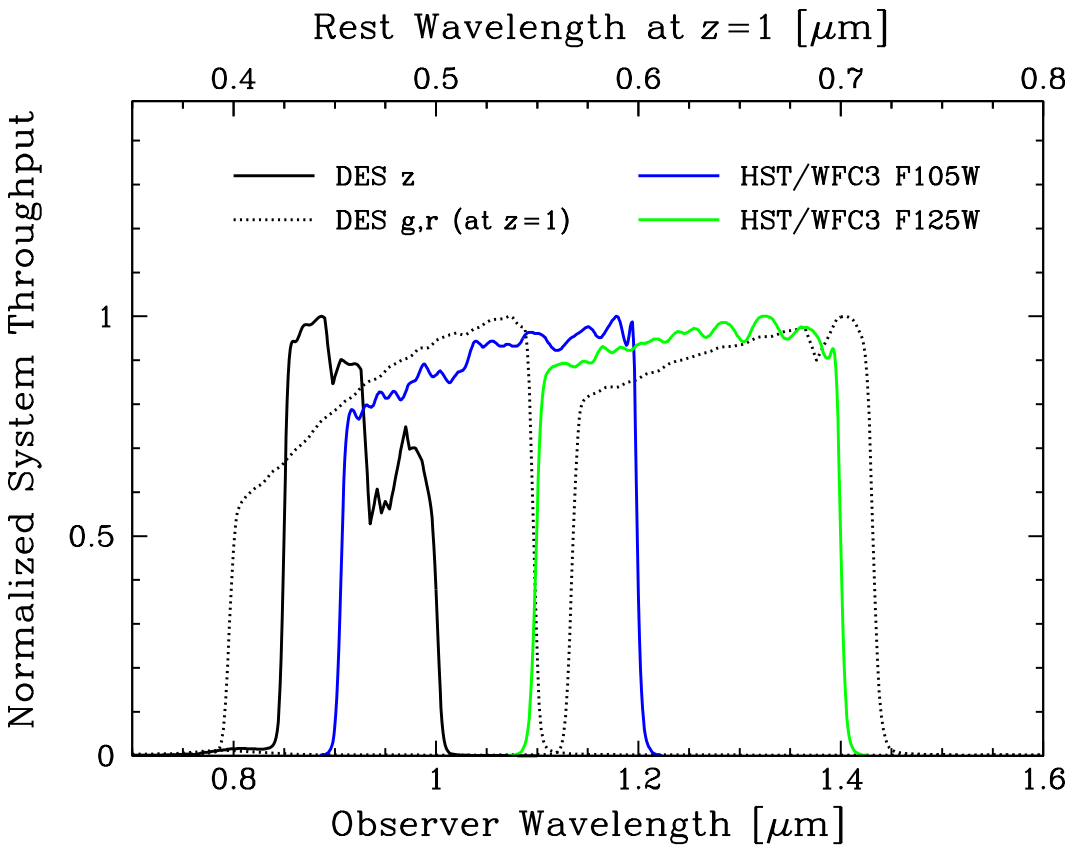

Figure 4.1

Figure 4.2 Without adding HST IR imaging, DES high-redshift SNe use observer frame *iz*, corresponding roughly to rest-frame *ug*, to constrain color. The addition of WFC3/IR F105W and F125W photometry adds rest-frame $g-r$ information, enabling a much better-determined color (and hence distance) measurement.

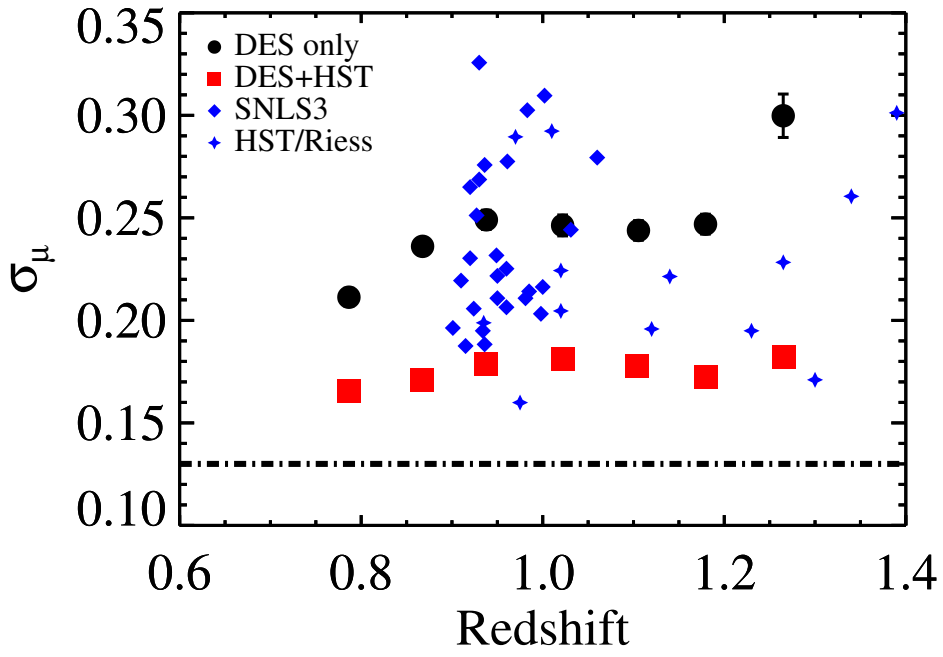

Figure 4.3 Distance modulus error as a function of redshift. The black points show constraints from DES only; the red points include NIR photometry with *HST*. Both sets of data have been averaged in redshift bins of $\Delta z = 0.1$. Here we assume a single orbit of *HST* observations taking place 3 weeks after trigger. Note the dramatic improvement from $\langle \sigma_\mu \rangle \sim 0.25$ to 0.17 with only a single *HST* visit. For comparison, distance measurement uncertainties from 39 $z > 0.9$ SN Ia from SNLS3 and *HST* (Riess et al. 2004, 2007) are overlaid in blue. These values are adopted from Sullivan et al. (2011). The black dashed line shows the intrinsic scatter associated with optical SN Ia distance measurements.

wavelength regime typically observed for optical distance measurements (4000 – 8000 Å) does not provide sufficient constraints on color or light-curve shape to distinguish between metallicities. While metallicity does impact the UV region of SN Ia SED's, observations of this area are challenging to obtain at low redshifts. On the other hand, at low redshifts distances – and therefore absolute luminosities – are known. More information is available to constrain host properties, and additional host galaxy observations are more easily obtainable at a wider range of wavelengths. If rest-frame UV observations of SNe Ia can be shown to be reliable, the investment of scarce scientific resources needed to get this information will be more palatable.

Our comparison of CSP and SDSS SN Ia broad-band *u* photometry (§2) showed that modern photometry techniques can achieve good average agreement in UV flux measurements. However, we found the dispersion in our UV photometry to be large. Our work suggested that much of this scatter was due to *S*-correction uncertainties, but the paucity of spectra with adequate wavelength coverage made these uncertainties difficult to quantify. More recently Betoule et al. (2012b) have used comparisons of calibration star catalogs to perform a more traditional cross-calibration check of SDSS and SNLS UV photometry. They found SDSS *u* calibration uncertainties to be on the order of 1% in flux, and 2% for the SNLS *u*[1]. Taken together, these two papers have provided evidence supporting the reliability of SDSS *u* photometry. Additional evidence buttressing these conclusions has come from a new sample of HST low-z SN Ia spectra described by Maguire et al. (2012). Synthetic photometry of these spectra indicate that natural variability in the UV combined with the relatively narrow width of the observer frame SDSS *u* filter explain the observed dispersion in SDSS UV observations (J Guy 2013, pers. comm., April 14, 2013). Based on these results, the SDSS observer frame *u* data will be included in the upcoming retraining of the SALT-II light curve fitter.

[1]The SNLS SN survey was aimed at higher redshifts and did not observe SNe Ia in *u*

4.2 Outlook for the future

Next season, the Dark Energy Survey will detect ~ 200 SNe Ia with redshifts < 0.4. These SNe Ia will have four bands of photometry, including high quality NIR (i and z) imaging. Using the SALT-II model to fit the three redder bands, corresponding to rest-frame *gri*, it will be possible to examine UV photometry residuals[2] as a function of SN Ia phase and rest-frame wavelength. If we assume a cosmology, we can also look at Hubble residuals as a function of UV photometry residuals. A correlation betwen specific UV photometry residuals and Hubble residuals would point the way to a light curve observable we could use as a third standardization parameter, and provide guidance in designing low-redshift SN surveys and low-z SN host galaxy follow-up to best explore this valuable wavelength region.

4.3 Scientific Acknowledgements

Funding for the SDSS and SDSS-II has been provided by the Alfred P. Sloan Foundation, the Participating Institutions, the National Science Foundation, the U.S. Department of Energy, the National Aeronautics and Space Administration, the Japanese Monbukagakusho, the Max Planck Society, and the Higher Education Funding Council for England. The SDSS Web Site is http://www.sdss.org/. The SDSS is managed by the Astrophysical Research Consortium for the Participating Institutions. The Participating Institutions are the American Museum of Natural History, Astrophysical Institute Potsdam, University of Basel, University of Cambridge, Case Western Reserve University, University of Chicago, Drexel University, Fermilab, the Institute for Advanced Study, the Japan Participation Group, Johns Hopkins University, the Joint Institute for Nuclear Astrophysics, the Kavli Institute for Particle Astrophysics and Cosmology, the Korean Scientist Group, the Chinese Academy of Sciences (LAMOST), Los Alamos National Laboratory, the Max-Planck-Institute for Astronomy (MPIA), the Max-Planck-Institute

[2] with respect to the best-fitting SALT-II model

for Astrophysics (MPA), New Mexico State University, Ohio State University, University of Pittsburgh, University of Portsmouth, Princeton University, the United States Naval Observatory, and the University of Washington. Support for this research at Rutgers University was provided in part by NSF CAREER award AST-0847157 to SWJ.

This work is based in part on observations made at the following telescopes. The APO 3.5 m telescope is owned and operated by the ARC. We thank the observatory director, Suzanne Hawley, and site manager, Bruce Gillespie, for their support of this project. The Subaru Telescope is operated by the National Astronomical Observatory of Japan. The William Herschel Telescope is operated by the Isaac Newton Group on the island of La Palma in the Spanish Observatorio del Roque de los Muchachos of the Instituto de Astrofisica de Canarias. Observations at the ESO New Technology Telescope at La Silla Observatory were made under programme IDs 77.A-0437, 78.A-0325, and 79.A-0715 . Kitt Peak National Observatory, National Optical Astronomy Observatories (NOAO), is operated by the Association of Universities for Research in Astronomy, Inc. (AURA) under cooperative agreement with the NSF. The WIYN Observatory is a joint facility of the University of Wisconsin-Madison, Indiana University, Yale University, and NOAO. The W. M. Keck Observatory is operated as a scientific partnership among the California Institute of Technology, the University of California, and NASA. The Observatory was made possible by the generous financial support of the W. M. Keck Foundation. The South African Large Telescope of the South African Astronomical Observatory is operated by a partnership between the National Research Foundation of South Africa, Nicolaus Copernicus Astronomical Center of the Polish Academy of Sciences, the Hobby-Eberly Telescope Board, Rutgers University, Georg-August-UniversitÂŁt GÂŽttingen, University of Wisconsin-Madison, University of Canterbury, University of North Carolina-Chapel Hill, Dartmouth College, Carnegie Mellon University, and the United Kingdom SALT consortium. A.V.F.'s supernova group at U.C. Berkeley is supported by NSF grant AST-0607485.

Thanks also to the SUSPECT Online Supernova Spectrum Archive.

Appendix A

Expected alpha determination

Mixing between the input x_1 and c parameters during the training process is not unexpected, and will lead to predictable changes in the recovered α model parameter.

The training process separates color from width by assuming that peak $B-V$ color will be zero for all SNe with c=0, regardless of x_1 value. If the input training set shows some variation in color with x_1, such that the observed color follows the form $c_{obs} = c_0 + bx_1$, the width-varying part of the color will be incorporated into the SALT-II model α term as follows:

$$m_B = M_B + K + \mu(z) - (\alpha - \beta b)x_1 + \beta c_0, \tag{A.1}$$

where K, $\mu(z)$, x_1, and c are the k-correction, distance modulus, width, and color of a specific SNIa, and M_B, α, and β are global SN Ia parameters.

By linearly fitting peak $B-V$ color as a function of $x1$ for each of our input models, and normalizing this slope with respect to the base G10 model such that $b \equiv b - b_{G10}$, we can measure the slope and predict the expected alpha value α_{exp}:

$$\alpha_{exp} = \alpha - \beta b. \tag{A.2}$$

We have used this technique to calculate expected values for α as a function of input model:

Table A.1. Expected α values

model	α_{exp}
GP-NONE	0.100
H-NONE	0.102
GP-G10	0.079
H-G10	0.106
GP-C11	0.099
H-C11	0.100

[h!]

Bibliography

Abazajian, K. N., et al. 2009, ApJS, 182, 543

Aihara, H., et al. 2011, ApJS, 193, 29

Aldering, G., et al. 2006, ApJ, 650, 510

Allen, S. W., Rapetti, D. A., Schmidt, R. W., Ebeling, H., Morris, R. G., & Fabian, A. C. 2008, MNRAS, 383, 879

Altavilla, G., et al. 2007, A&A, 475, 585

Amanullah, R., et al. 2010, ApJ, 716, 712

Astier, P. 2012, ArXiv e-prints

Astier, P., et al. 2006, A&A, 447, 31

Axelrod, T. S. 1980a, PhD thesis, California Univ., Santa Cruz.

Axelrod, T. S. 1980b, in Texas Workshop on Type I Supernovae, ed. J. C. Wheeler, 80–95

Bailey, S., et al. 2009, A&A, 500, L17

Balland, C., et al. 2009, A&A, 507, 85

Barone-Nugent, R. L., et al. 2012, MNRAS, 425, 1007

Benetti, S., et al. 2004, MNRAS, 348, 261

Bernstein, J. P., et al. 2012, ApJ, 753, 152

Betoule, M., Astier, P., Guy, J., Regnault, N., & El Hage, P. in preparation

Betoule, M., Marriner, J., & Reynauld, N. 2012a, in prep

Betoule, M., et al. 2012b, ArXiv e-prints

Blaylock, M., Branch, D., Casebeer, D., Millard, J., Baron, E., Richardson, D., & Ancheta, C. 2000, PASP, 112, 1439

Blondin, S., & Tonry, J. L. 2007, ApJ, 666, 1024

Branch, D., Lacy, C. H., McCall, M. L., Sutherland, P. G., Uomoto, A., Wheeler, J. C., & Wills, B. J. 1983, ApJ, 270, 123

Brown, P. J., et al. 2010, ApJ, 721, 1608

Calzetti, D., Kinney, A. L., & Storchi-Bergmann, T. 1994, ApJ, 429, 582

Cappellaro, E., et al. 2001, ApJ, 549, L215

Cardelli, J. A., Clayton, G. C., & Mathis, J. S. 1989, ApJ, 345, 245

Chotard, N., et al. 2011, A&A, 529, L4

Conley, A., Carlberg, R. G., Guy, J., Howell, D. A., Jha, S., Riess, A. G., & Sullivan, M. 2007, ApJ, 664, L13

Conley, A., et al. 2008, ApJ, 681, 482

—. 2011, ApJS, 192, 1

Contreras, C., et al. 2010, AJ, 139, 519

Cooke, J., et al. 2011, ApJ, 727, L35

D'Agostini, G. 1995, Nuclear Instruments and Methods in Physics Research A, 362, 487

D'Andrea, C. B., et al. 2011, ApJ, 743, 172

Doi, M., et al. 2010, AJ, 139, 1628

Einstein, A. 1915, Sitzungsberichte der Königlich Preußischen Akademie der Wissenschaften (Berlin), Seite 844-847., 844

Eisenstein, D. J., et al. 2005, ApJ, 633, 560

Elias-Rosa, N., et al. 2006, MNRAS, 369, 1880

Ellis, R. S., et al. 2008, ApJ, 674, 51

Filippenko, A. V., et al. 1992, AJ, 104, 1543

Folatelli, G., et al. 2010, AJ, 139, 120

Foley, R. J., & Kasen, D. 2011, ApJ, 729, 55

Foley, R. J., & Kirshner, R. P. 2013, ArXiv e-prints

Foley, R. J., Sanders, N. E., & Kirshner, R. P. 2011, ApJ, 742, 89

Foley, R. J., et al. 2008, ApJ, 684, 68

—. 2012a, AJ, 143, 113

—. 2012b, ApJ, 744, 38

Freedman, W. L., et al. 2009, ApJ, 704, 1036

Friedmann, A. 1922, Zeitschrift fÃ?r Physik, 10, 377

—. 1924, Zeitschrift für Physik, 21, 326

Frieman, J. A., et al. 2008a, AJ, 135, 338

—. 2008b, AJ, 135, 338

Fukugita, M., Ichikawa, T., Gunn, J. E., Doi, M., Shimasaku, K., & Schneider, D. P. 1996, AJ, 111, 1748

Ganeshalingam, M., et al. 2010, ApJS, 190, 418

Giannantonio, T., Scranton, R., Crittenden, R. G., Nichol, R. C., Boughn, S. P., Myers, A. D., & Richards, G. T. 2008, Phys. Rev. D, 77, 123520

Gunn, J. E., et al. 1998, AJ, 116, 3040

—. 2006, AJ, 131, 2332

Gupta, R. R., et al. 2011, ApJ, 741, 127

Guy, J., Astier, P., Nobili, S., Regnault, N., & Pain, R. 2005, A&A, 443, 781

Guy, J., et al. 2007, A&A, 466, 11

—. 2010, A&A, 523, A7+

Hamuy, M., et al. 1996, AJ, 112, 2408

—. 2002, AJ, 124, 417

—. 2006, PASP, 118, 2

Hicken, M., Wood-Vasey, W. M., Blondin, S., Challis, P., Jha, S., Kelly, P. L., Rest, A., & Kirshner, R. P. 2009a, ApJ, 700, 1097

Hicken, M., et al. 2009b, ApJ, 700, 331

Hoeflich, P., Wheeler, J. C., & Thielemann, F. K. 1998, ApJ, 495, 617

Hogg, D. W., Baldry, I. K., Blanton, M. R., & Eisenstein, D. J. 2002, ArXiv Astrophysics e-prints

Hogg, D. W., Finkbeiner, D. P., Schlegel, D. J., & Gunn, J. E. 2001, AJ, 122, 2129

Holtzman, J. A., et al. 2008, AJ, 136, 2306

Hoyle, F., & Fowler, W. A. 1960, ApJ, 132, 565

Hsiao, E. Y., Conley, A., Howell, D. A., Sullivan, M., Pritchet, C. J., Carlberg, R. G., Nugent, P. E., & Phillips, M. M. 2007, ApJ, 663, 1187

Ivezić, Ž., et al. 2007, AJ, 134, 973

Jha, S., Riess, A. G., & Kirshner, R. P. 2007, ApJ, 659, 122

Jha, S., et al. 2006, AJ, 131, 527

Kaiser, N., & Pan-STARRS Team. 2005, in Bulletin of the American Astronomical Society, Vol. 37, American Astronomical Society Meeting Abstracts, 150.04

Kasen, D. 2010, ApJ, 708, 1025

Kasen, D., & Plewa, T. 2007, ApJ, 662, 459

Kasen, D., Röpke, F. K., & Woosley, S. E. 2009, Nature, 460, 869

Kattner, S., et al. 2012, PASP, 124, 114

Kelly, P. L., Hicken, M., Burke, D. L., Mandel, K. S., & Kirshner, R. P. 2010, ApJ, 715, 743

Kessler, R., et al. 2009a, ApJS, 185, 32

—. 2009b, PASP, 121, 1028

—. 2009c, PASP, 121, 1028

—. 2012, submitted

Kim, A., Goobar, A., & Perlmutter, S. 1996, Publications of the Astronomical Society of the Pacific, 108, 190

Kinney, A. L., Calzetti, D., Bohlin, R. C., McQuade, K., Storchi-Bergmann, T., & Schmitt, H. R. 1996, ApJ, 467, 38

Komatsu, E., et al. 2009, ApJS, 180, 330

Kotak, R., et al. 2005, A&A, 436, 1021

Kowal, C. T. 1968, AJ, 73, 1021

Kowalski, M., et al. 2008, ApJ, 686, 749

Krisciunas, K., et al. 2009, AJ, 138, 1584

Lampeitl, H., et al. 2010, ApJ, 722, 566

Landolt, A. U. 1992, AJ, 104, 340

Leavitt, H. S. 1908, Annals of Harvard College Observatory, 60, 87

Leibundgut, B., et al. 1993, AJ, 105, 301

Lemaître, G. 1927, Annales de la Societe Scietifique de Bruxelles, 47, 49

Lentz, E. J., Baron, E., Branch, D., Hauschildt, P. H., & Nugent, P. E. 2000, ApJ, 530, 966

Leonard, D. C., Li, W., Filippenko, A. V., Foley, R. J., & Chornock, R. 2005, ApJ, 632, 450

Lira, P. 1995, Master's thesis, Univ. Chile

LSST Science Collaboration et al. 2009, ArXiv e-prints

Lupton, R. H., Gunn, J. E., & Szalay, A. S. 1999, AJ, 118, 1406

Maeda, K., et al. 2011, MNRAS, 413, 3075

Maguire, K., et al. 2012, MNRAS, 426, 2359

Maoz, D., & Mannucci, F. 2012, **??**jnlPASA, 29, 447

Marriner, J., et al. 2011, ApJ, 740, 72

Mazzali, P. A. 2000, A&A, 363, 705

Mazzali, P. A., & Podsiadlowski, P. 2006, MNRAS, 369, L19

Milne, P. A., et al. 2010, ApJ, 721, 1627

Mosher, J., et al. 2012, AJ, 144, 17

Nobili, S., & Goobar, A. 2008, A&A, 487, 19

Nugent, P., Kim, A., & Perlmutter, S. 2002, PASP, 114, 803

Parkinson, D., et al. 2012, Phys. Rev. D, 86, 103518

Pastorello, A., et al. 2007a, MNRAS, 377, 1531

—. 2007b, MNRAS, 376, 1301

Patat, F., Benetti, S., Cappellaro, E., Danziger, I. J., della Valle, M., Mazzali, P. A., & Turatto, M. 1996, MNRAS, 278, 111

Perlmutter, S., et al. 1999, ApJ, 517, 565

Perrett, K., et al. 2010, AJ, 140, 518

Phillips, M. M. 1993, ApJ, 413, L105

Phillips, M. M., Lira, P., Suntzeff, N. B., Schommer, R. A., Hamuy, M., & Maza, J. 1999, AJ, 118, 1766

Phillips, M. M., et al. 2007, PASP, 119, 360

Pickering, E. C. 1890, Annals of Harvard College Observatory, 27, 1

Pier, J. R., Munn, J. A., Hindsley, R. B., Hennessy, G. S., Kent, S. M., Lupton, R. H., & Ivezić, Ž. 2003, AJ, 125, 1559

Planck Collaboration et al. 2013, ArXiv e-prints

Prieto, J. L., et al. 2007, ArXiv e-prints

Pskovskii, I. P. 1977, Soviet Ast., 21, 675

Quimby, R., Höflich, P., & Wheeler, J. C. 2007, ApJ, 666, 1083

Regnault, N., et al. 2009, A&A, 506, 999

Rheault, J.-P., Depoy, D. L., Behm, T. W., Kylberg, E. W., Cabral, K., Allen, R., & Marshall, J. L. 2010, in Society of Photo-Optical Instrumentation Engineers (SPIE) Conference Series, Vol. 7735, Society of Photo-Optical Instrumentation Engineers (SPIE) Conference Series

Riess, A. G., Press, W. H., & Kirshner, R. P. 1996, ApJ, 473, 588

Riess, A. G., et al. 1998, AJ, 116, 1009

—. 1999, AJ, 117, 707

—. 2004, ApJ, 607, 665

—. 2007, ApJ, 659, 98

Sako, M., et al. 2008, AJ, 135, 348

—. 2012, in prep

Salvo, M. E., Cappellaro, E., Mazzali, P. A., Benetti, S., Danziger, I. J., Patat, F., & Turatto, M. 2001, MNRAS, 321, 254

Sauer, D. N., et al. 2008, MNRAS, 391, 1605

Schlegel, D. J., Finkbeiner, D. P., & Davis, M. 1998, ApJ, 500, 525

Smith, J. A., et al. 2002, AJ, 123, 2121

Spergel, D. N., et al. 2003, ApJS, 148, 175

Stanishev, V., et al. 2007, A&A, 469, 645

Stoughton, C., et al. 2002, AJ, 123, 485

Stritzinger, M., et al. 2002, AJ, 124, 2100

Stritzinger, M. D., et al. 2011, AJ, 142, 156

Sullivan, M., Ellis, R. S., Howell, D. A., Riess, A., Nugent, P. E., & Gal-Yam, A. 2009, ApJ, 693, L76

Sullivan, M., et al. 2010, MNRAS, 406, 782

—. 2011, ApJ, 737, 102

Suntzeff, N. B. 2000, in American Institute of Physics Conference Series, Vol. 522, American Institute of Physics Conference Series, ed. S. S. Holt & W. W. Zhang, 65–74

Timmes, F. X., Brown, E. F., & Truran, J. W. 2003, ApJ, 590, L83

Tonry, J. L., et al. 2003, ApJ, 594, 1

—. 2012, ApJ, 750, 99

Tripp, R. 1998, A&A, 331, 815

Tucker, D. L., et al. 2006, Astronomische Nachrichten, 327, 821

Turon, C., Luri, X., & Masana, E. 2012, Ap&SS, 341, 15

Van Helden, A. 2010, Measuring the Universe: Cosmic Dimensions from Aristarchus to Halley (University of Chicago Press)

Walker, E. S., Hachinger, S., Mazzali, P. A., Ellis, R. S., Sullivan, M., Gal Yam, A., & Howell, D. A. 2012, MNRAS, 427, 103

Wang, X., et al. 2012, ApJ, 749, 126

Webb, S. 1999, Measuring the Universe: The Cosmological Distance Ladder, Springer-Praxis Series in Astronomy and Astrophysics (Springer)

Wheeler, J. C., & Harkness, R. P. 1990, Reports on Progress in Physics, 53, 1467

Wood-Vasey, W. M., et al. 2007, ApJ, 666, 694

York, D. G., et al. 2000, AJ, 120, 1579